

สมบัติทางไฟฟ้า สมบัติทางแสงและสมบัติการรับรู้แก๊สของฟิล์มบางแบบเรียบไททานेट/
สตรอนเทียมไททานेट



นางสาวธิดารัตน์ สุภาสัย

ศูนย์วิทยทรัพยากร
จุฬาลงกรณ์มหาวิทยาลัย

วิทยานิพนธ์นี้เป็นส่วนหนึ่งของการศึกษาตามหลักสูตรปริญญาวิทยาศาสตรดุษฎีบัณฑิต

สาขาวิชาฟิสิกส์ ภาควิชาฟิสิกส์

คณะวิทยาศาสตร์ จุฬาลงกรณ์มหาวิทยาลัย

ปีการศึกษา 2553

ลิขสิทธิ์ของจุฬาลงกรณ์มหาวิทยาลัย



5 0 7 3 8 2 7 1 2 3

ELECTRICAL, OPTICAL AND GAS SENSING PROPERTIES OF BARIUM
TITANATE/STRONTIUM TITANATE THIN FILMS



Miss Thidarat Supasai

ศูนย์วิทยทรัพยากร
จุฬาลงกรณ์มหาวิทยาลัย

A Dissertation Submitted in Partial Fulfillment of the Requirements

for the Degree of Doctor of Philosophy Program in Physics

Department of Physics

Faculty of Science

Chulalongkorn University

Academic Year 2010

Copyright of Chulalongkorn University

Thesis Title ELECTRICAL, OPTICAL AND GAS SENSING PROPERTIES OF BARIUM TITANATE/STRONTIUM TITANATE THIN FILMS


By Miss Thidarat Supasai

Field of Study Physics

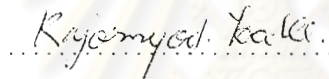
Thesis Advisor Assistant Professor Satreerat Hodak, Ph.D.

Thesis Co-advisor Anurat Wisitsoraat, Ph.D.

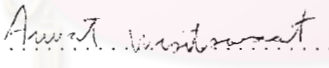
Accepted by the Faculty of Science, Chulalongkorn University in Partial Fulfillment of the Requirements for the Doctoral Degree


 Dean of the Faculty of Science
(Professor Supot Hannongbua, Dr.rer.nat.)


THESIS COMMITTEE


 Chairman
(Assistant Professor Kajornyod Yoodee, Ph.D.)

 Thesis advisor
(Assistant Professor Satreerat Hodak, Ph.D.)

 Thesis Co-Advisor
(Anurat Wisitsoraat, Ph.D.)

 Examiner
(Chatchai Srinitiwirawong, Ph.D.)

 Examiner
(Assistant Professor Nakorn Phaisangittisakul, Ph.D.)

 External Examiner
(Pongpan Chindaodom, Ph.D.)

ธิดารัตน์ สุภาลัย : สมบัติทางไฟฟ้า สมบัติทางแสง และสมบัติการรับรู้แก๊สของฟิล์มบางแบบเรียบไททาเนต/สตรอนเทียมไททาเนต. (ELECTRICAL, OPTICAL AND GAS SENSING PROPERTIES OF BARIUM TITANATE/STRONTIUM TITANATE THIN FILMS) อ. ที่ปรึกษาวิทยานิพนธ์หลัก : ผศ. ดร. สตรีรัตน์ ไสค์ด, อ. ที่ปรึกษาวิทยานิพนธ์ร่วม : ดร. อนุรัตน์ วิศิษฎ์สรอรรถ, 169 หน้า.

พหุผลึกฟิล์มแบบเรียบไททาเนต/สตรอนเทียมไททาเนตแบบสลับชั้นถูกเตรียมโดยวิธีโซล-เจลลงบนแผ่นรองรับต่างชนิดสอดคล้องตามสมบัติของฟิล์มที่จะถูกศึกษา อินเดียมทินออกไซด์ปลูกบนกระจกถูกใช้เป็นแผ่นรองรับเพื่อศึกษาสมบัติทางแสงของฟิล์ม พบว่า ค่าช่องว่างพลังงานของฟิล์มค่อย ๆ ลดลงจาก 4.19 เป็น 4.03 อิเล็กตรอนโวลต์เมื่อฟิล์มถูกอบที่อุณหภูมิต่ำ (300 - 550 องศาเซลเซียส) ในขณะที่ค่าช่องว่างพลังงานของฟิล์มอบที่อุณหภูมิสูง (600 - 650 องศาเซลเซียส) อยู่ในช่วง 3.64-3.74 อิเล็กตรอนโวลต์ ค่าดัชนีหักเหของฟิล์มอยู่ในช่วง 1.69-2.10 ขึ้นอยู่กับอุณหภูมิที่ใช้อบฟิล์ม ค่าสัมประสิทธิ์การดูดกลืนของฟิล์มอยู่ในอันดับ 10^2 แผ่นรองรับอะลูมินาถูกใช้เพื่อศึกษาการรับรู้แก๊สและวัดค่าคงที่ไดอิเล็กทริกของฟิล์ม ในงานวิจัยนี้ พบว่าความไวต่อแก๊สของฟิล์มบางสามารถปรับปรุงได้โดยการเพิ่มปริมาณของเหล็กที่เจือลงในฟิล์มบางและอุณหภูมิขณะทดลอง ค่าความไวของแก๊สเอทานอลในช่วงความเข้มข้น 100 - 1000 พีพีเอ็มของฟิล์มเจือเหล็กร้อยละ 8 โดยน้ำหนัก มีค่าอยู่ในช่วง 3-10 ซึ่งมีค่ามากกว่าประมาณสองเท่าของค่าความไวของแก๊สเอทานอลของฟิล์มเจือเหล็กที่ร้อยละ 2 โดยน้ำหนักเมื่ออุณหภูมิขณะทดลองเป็น 350 องศาเซลเซียส นอกจากนี้ พบว่า ค่าคงที่ไดอิเล็กทริกของฟิล์มสามารถปรับปรุงได้โดยการปลูกฟิล์มแบบสลับชั้นและโดยการนำฟิล์มไปฉายรังสีแกมมา ผู้วิจัยพบว่าค่าคงที่ไดอิเล็กทริกของฟิล์มแบบเรียบไททาเนต/สตรอนเทียมไททาเนตแบบสลับชั้น ฟิล์มแบบเรียบไททาเนต และฟิล์มสตรอนเทียมไททาเนต มีค่าประมาณ 522 280 และ 188 ตามลำดับ วัดที่อุณหภูมิห้อง ที่ความถี่ 100 กิโลเฮิร์ต และค่าคงที่ไดอิเล็กทริกของฟิล์มแบบเรียบไททาเนต/สตรอนเทียมไททาเนตแบบสลับชั้นหลังถูกฉายรังสีแกมมาที่ 30 กิโลเกรย์ มีค่าเพิ่มขึ้นเป็น 830 และค่าความสูญเสียไดอิเล็กทริกของฟิล์มทุกชนิดอยู่ในอันดับ 10^{-2} วัดที่ความถี่ 100 กิโลเฮิร์ต

ภาควิชา..... ฟิสิกส์..... ลายมือชื่อ..... Thidarat Supalai
 สาขาวิชา..... ฟิสิกส์..... ลายมือชื่อ อ.ที่ปรึกษาวิทยานิพนธ์หลัก..... Sittreeat Hadda
 ปีการศึกษา..... 2553..... ลายมือชื่อ อ.ที่ปรึกษาวิทยานิพนธ์ร่วม..... Sittreeat Hadda

5073827123 : MAJOR PHYSICS

KEYWORDS : SrTiO₃/BaTiO₃ / GAS SENSOR / DIELECTRIC

THIDARAT SUPASAI : ELECTRICAL, OPTICAL AND GAS SENSING PROPERTIES OF BARIUM TITANATE/STRONTIUM TITANATE THIN FILMS. ADVISOR : ASST. PROF. SATREERAT HODAK, Ph.D.. CO-ADVISOR : ANURAT WISITSORAAT, Ph.D., 169 pp.

Polycrystalline SrTiO₃/BaTiO₃ multilayer films (STO/BTO) were prepared by a sol-gel spin coating technique on different types of substrates suitable to the desired applications. ITO coated on glass was used as a substrate to investigate the optical properties of the films. The value of energy gap gradually decreased from 4.19 to 4.03 eV as the films were annealed at lower temperature (300-550 °C) while that of the films annealed at higher temperature of 600 and 650 °C was in the 3.64-3.74 eV range. The refractive index of the films was in the range of 1.69-2.10 depending on annealing temperature and the extinction coefficient of the films was in the order of 10⁻². Al₂O₃ was used as a substrate to characterize ethanol sensing and dielectric properties of the films. The sensitivity of the films can be improved with increasing Fe-doping concentration and operating temperature. The sensitivity obtained at 350 °C to ethanol vapor concentration in the 100-1000 ppm of the films doped with Fe 8 wt% was in the 3-10 range which was about two times higher than that of the Fe 2 wt% doped films. The dielectric constant of the films can be improved by constructing multilayer films and by irradiating gamma ray on the film devices. The room temperature dielectric constant of STO/BTO, uniform BTO and uniform STO films was approximately 522, 280 and 188, respectively measuring at 100 kHz whereas the dielectric constant of STO/BTO films increased up to 830 after irradiated to gamma ray at dose of 30 kGy. The loss tangent of all films was in the order of 10⁻² at 100 kHz.

Department : Physics Student's Signature *Thidarat Supasai*
 Field of Study : Physics Advisor's Signature *Satreerat Hodak*
 Academic Year : 2010 Co-advisor's Signature *Anurat Wisitsoraat*

Acknowledgements

I would like to express my gratitude to my thesis advisor, Assistant Professor Dr. Satreerat Hodak for giving me the opportunity to work on this interesting project and for her guidance, time throughout the course of thesis. I would especially like to thank Dr. Anurat Wisitsoraat, my thesis co-advisor, for his kind suggestions during this work. I am also grateful to Assistant Professor Dr. Kajornyod Yoodee, Dr. Chatchai Srinitiwara Wong, Assistant Professor Dr. Nakorn Phaisangittisakul and Dr. Pongpan Chindaudom for serving as a chairman and committee, respectively. All of whom have made valuable comments and have been helpful in the production of thesis.

I would like to thank the financial supports from Department of Physics, Faculty of Science, Chulalongkorn University and Graduate Thesis Grant for paying fund to attend conferences.

Especially, I would like to thank the Thailand Graduate Institute of Science and Technology (TGIST) for providing tuition fee and other expenses.

I would like to thank Synchrotron Light Research Institute (Public organization) for the help in XAS measurement at beamline 8, Siam Photon Laboratory, Nakhon Ratchasima province.

I also thank all of my colleagues (Ornicha Kongwut, Yumairoh Kasa, Pavarit Promsena) for their kind support, help, fun and suggestion during my study. Thanks to all my friends at the Department of Physics for a good relationships. Thanks to Mr. Disayut Phokharatkul for the help in sputtering electrode and dicing the samples and also thank to all my friends at the Nanoelectronics and MEMS Laboratory, National Electronics and Computer Technology Center (NECTEC) for their helping and suggestions.

Finally, my warm and deep affectionate appreciation are to my family; my father, my mother and my sisters for their love, encouragement, understanding and supporting throughout my Ph.D. study.

Contents

	Page
Abstract (Thai)	iv
Abstract (English).....	v
Acknowledgements	vi
Contents	vii
List of Tables.....	x
List of Figures.....	xi
 Chapter	
I INTRODUCTION.....	1
1.1 Thesis motivation	1
1.2 The aims of this thesis are:	12
1.3 Overview of this thesis	13
II THEORETICAL BACKGROUND.....	14
2.1 BaTiO ₃ material	14
2.2 SrTiO ₃ material	17
2.3 Sol-gel process	19
2.3.1 Spin coating	20
2.3.2 Drying	22

Chapter	Page
2.3.3 Sol-gel densification	22
2.4 Interference conditions in a thin film	23
2.5 Dielectric properties	26
2.5.1 Dielectric materials in electric field	26
2.5.2 Dielectric constant	27
2.5.3 Dielectric loss	32
2.6 Gas sensor	33
2.6.1 Mechanism of gas sensor	34
2.6.2 The influence of microstructure and grain size of film	39
III CHARACTERIZATION TECHNIQUES	43
3.1 X-ray diffraction	43
3.1.1 X-ray production	44
3.1.2 Bragg's Law	45
3.2 Field emission scanning electron microscopy	48
3.3 X-ray absorption spectroscopy	51
3.4 Ultraviolet-visible spectroscopy	56
3.4.1 Determination of refractive index and film thickness	59
3.4.2 Determination of energy gap and Urbach energy	61
3.5 Atomic force microscopy	62
IV EXPERIMENTAL DETAILS	65
4.1 Synthesis of BaTiO ₃ and SrTiO ₃ precursors	65
4.2 Substrate preparation and conditions for film deposition	66

Chapter	Page
4.3 Spin coating process	68
4.4 Fabrication of device	72
4.4.1 Mask fabrication	73
4.4.2 Electrode deposition	76
4.5 Gas sensing property measurement	78
4.6 Gamma ray irradiation	81
4.7 Dielectric property measurement	82
4.7.1 Dielectric constant determination of interdigitated capacitor	86
V RESULTS AND DISCUSSIONS	88
5.1 Effect of annealing temperature on structural properties and surface morphology of SrTiO ₃ /BaTiO ₃ films	88
5.2 Effect of annealing temperature on optical properties of SrTiO ₃ /BaTiO ₃ films	95
5.3 Oxidation state and weight percentage of Fe in SrTiO ₃ /BaTiO ₃ films	105
5.4 Effect of Fe doping on structural properties and surface morphology of SrTiO ₃ /BaTiO ₃ films	108
5.5 Effect of Fe doping on gas sensing properties of SrTiO ₃ /BaTiO ₃ films	112
5.6 Effect of multilayer structure film and Fe dopant on dielectric constant	119
5.7 Effect of gamma irradiation on dielectric constant	132
VI CONCLUSION	139
References	142
Appendices	160
Appendix A: XRD database	161

Chapter	Page
Appendix B: Weight percentage calculating of Fe doping	164
concentrations	164
Appendix C: Conference presentations	165
Appendix D: Publications	167
Appendix E: Research award	168
Vitae	169



ศูนย์วิทยทรัพยากร
จุฬาลงกรณ์มหาวิทยาลัย

List of Tables

Table	Page
2.1 The physical properties of bulk BaTiO ₃	17
2.2 The physical properties of bulk SrTiO ₃	17
2.3 The major steps in a sol-gel process.	23
4.1 The physical properties of alumina substrate.	67
4.2 Deposition conditions for film growth.	69
4.3 The current and time using in electroplating process.	74
4.4 The doses of gamma ray using for irradiation.	82
5.1 Weight and atomic percentage of Fe in BaTi _{1-x} Fe _x O ₃ films	105
5.2 Weight and atomic percentage of Fe in SrTi _{1-x} Fe _x O ₃ films	105
5.3 Response and recovery time of SrTiO ₃ /BaTiO ₃ films doped with Fe 2 wt% operating at 250 °C.	114
5.4 Response and recovery time of SrTiO ₃ /BaTiO ₃ films doped with Fe 8 wt% operating at 250 °C.	114
5.5 Response and recovery time of SrTiO ₃ /BaTiO ₃ films doped with Fe 8 wt% operating at 350 °C.	115
5.6 The value of dielectric constant and loss tangent of all films at 100 kHz with no bias voltage.	123

List of Figures

Figure	Page
2.1 The unit cell of perovskite cubic structure.	15
2.2 The crystal structure of BaTiO ₃ ; (a) below T _c , the structure is tetragonal and (b) above T _c , the structure is cubic.	15
2.3 Polarization behavior as a function of electric field in ferroelectric material (a) above T _c and (b) below T _c	16
2.4 Permittivity versus temperature of bulk SrTiO ₃ for at DC bias electric field of 0, 5 V/μm and 10 V/μm [90].	18
2.5 The four stages of spin coating process (a) deposition, (b) spin up, (c) spin off and (d) evaporation.	21
2.6 Schematic of optical model for air/thin film/substrate structure.	24
2.7 (a) Displacement of center of positive and negative charge due to an applied external electric field. (b) Electric flux line of dipole (solid line) and applied external electric flux line (dash line).	27
2.8 A parallel-plate capacitor inserting with dielectric material.	28
2.9 Schematic of various polarization mechanisms.	30
2.10 Frequency dependence of polarizability.	31
2.11 Phasor diagram of (a) an air capacitor and (b) capacitor filled with dielectric.	32
2.12 Schematic of basic structure of gas sensor having reactor and transducer.	34
2.13 Typical transient signal of a sensor as a function of time.	35

Figure	Page
2.14 Energy band diagram of a metal-p-type semiconductor junction for $\phi_s > \phi_m$ (a) before and (b) after contact.	36
2.15 Schematic of potential barrier of gas sensor at a grain boundary.	38
2.16 Schematic of agglomerated polycrystalline films showing contribution of different components of resistances.	40
2.17 Schematic model for grain size effect. Shaded area represents to depletion region (high resistance) whereas unshaded area refers to core region (low resistance).	42
3.1 Schematic showing probability of X-ray production.	44
3.2 Schematic of X-ray spectra includes brehmsstrahlung and K_α and K_β characteristic radiation.	46
3.3 Schematic representation of X-ray diffraction from crystal structure according to Bragg's law.	47
3.4 Schematic of basic fundamental element of FESEM.	49
3.5 The interaction between primary electron beam on sample surface showing the excitation volume produced auger electrons, secondary electrons, backscattered electrons, characteristic X-rays and continuous X-rays with their depths within the sample.	50
3.6 Schematic of (a) X-ray absorption, (b) relaxation of electron in excited state emitting fluorescent X-ray and (c) auger electron emission.	52
3.7 Schematic of (a) Transmission mode (b) Fluorescent mode often using in XAS measurement.	54
3.8 XAS spectrum including pre-edge, XANES, EXAFS regions and absorption edge.	55

Figure	Page
3.9 Schematics of photoelectron wave outgoing (solid circles) from an absorber atom and backscattering (dashed circles) form neighbor atom (a) constructive interference and (b) destructive interference.	56
3.10 Schematic representation of molecule energy showing electronic, vibrational and rotational energy states and electronic transitions.	57
3.11 Schematic of a double beam UV-Vis spectrophotometer.	58
3.12 A sketch of enveloped of the optical transmittance.	60
3.13 Schematic of atomic force microscope.	63
3.14 interaction force between an atom at the apex of the tip and an atom in the sample surface as a function of distance between the tip and the surface following Lennard-Jones potential.	64
4.1 The layout of synthesis of barium titanate or strontium titanate by sol gel method.	66
4.2 Schematic representation of (a) SrTiO ₃ /BaTiO ₃ film on ITO coated on glass substrate, (b) BaTiO ₃ /BaTiO ₃ /BaTiO ₃ /BaTiO ₃ /BaTiO ₃ film on alumina substrate, (c) SrTiO ₃ /SrTiO ₃ /SrTiO ₃ /SrTiO ₃ /SrTiO ₃ film on alumina substrate and (d) SrTiO ₃ /BaTiO ₃ /SrTiO ₃ /BaTiO ₃ /SrTiO ₃ film on alumina substrate.	70
4.3 The photograph of spin coater machine model P6700 series.	70
4.4 The flow chart for multilayer film deposition with different growth conditions by spin coating process.	71
4.5 The schematic of annealing process.	72
4.6 The schematic of configuration of interdigitated electrode.	73
4.7 The schematic of photolithography process steps.	75

Figure	Page
4.8 A photograph showing a set of Ni interdigitated mask containing 90 pieces of configuration.	76
4.9 The photograph showing the interdigitated mask mounted the films closely by using array of magnets.	77
4.10 The photograph of a device.	77
4.11 Schematic set up for gas sensing measurement.	79
4.12 A gas testing chamber.	80
4.13 The photograph presenting the stage and probes used for measuring the resistance of the films	80
4.14 The photograph showing the capacitors mounted on foam sent them to gamma source.	81
4.15 The photograph showing the Red Perspex used for calibrating the gamma ray doses.	82
4.16 The schematic diagram of a ring resonator used in capacitance measurement. Flip chip presented as variable capacitors.	84
4.17 The image of interdigitated capacitor connected to a ring resonator.	84
4.18 The photograph of LF impedance analyzer model HP 4192A connected to a ring resonator box.	85
4.19 Schematic representation of (a) top view and (b) cross section of capacitor with interdigitated electrode structure showing all parameters for calculating dielectric constant of films.	87
5.1 X-ray diffraction pattern of SrTiO ₃ /BaTiO ₃ films annealed at different temperatures on ITO/glass.	89

Figure	Page
5.2 X-ray diffraction pattern of SrTiO ₃ /BaTiO ₃ films on Si substrate annealed at temperatures of 800 °C.	91
5.3 X-ray diffraction pattern of uniform BaTiO ₃ and SrTiO ₃ films on Si substrate annealed at temperatures of 1000 °C.	92
5.4 X-ray diffraction pattern of SrTiO ₃ /BaTiO ₃ films on Al ₂ O ₃ substrate annealed at temperatures of 100 °C.	93
5.5 AFM images (0.3 μm x 0.3 μm) of SrTiO ₃ /BaTiO ₃ films deposited on ITO coated glass annealed at different temperatures (a) 300 °C, (b) 500 °C, (c) 550 °C, (d) 600 °C and (e) 650 °C.	94
5.6 Transmittance spectra of SrTiO ₃ /BaTiO ₃ films annealed at different temperatures (a) 300 °C, (b) 500 °C, (c) 550 °C, (d) 600 °C and (e) 650 °C.	95
5.7 Transmittance spectra of SrTiO ₃ /BaTiO ₃ /SrTiO ₃ /BaTiO ₃ films annealed at 600 °C.	96
5.8 Transmittance spectra of BaTiO ₃ and Ba _{0.8} Fe _{0.2} TiO ₃ films before and after gamma irradiation at a dose of 15 kGy reported by Kongwut et al.	97
5.9 Determination of Urbach energy for SrTiO ₃ /BaTiO ₃ films annealed at 500, 550 and 600 °C from the absorption coefficient.	98
5.10 Plot of (αhν) ² versus hν for SrTiO ₃ /BaTiO ₃ films annealed at various temperatures.	99
5.11 Temperature dependence of the optical band gap energy for SrTiO ₃ /BaTiO ₃ films.	100
5.12 Direct and indirect band gap energies versus the average particle size. The solid line is prediction by quantum size effect. The dashed lines are the prediction of the quantum size effect with adjustable effective mass.	101

Figure	Page
5.13 The variation of (a) refractive index, n and (b) extinction coefficient, k of the films as a function of wavelength.	104
5.14 (a) Fe K-edge XANES spectra of Fe-doped SrTiO ₃ /BaTiO ₃ multilayer films with various Fe concentrations (b) pre-edge and absorption regions.	107
5.15 (a) X-ray diffraction patterns of Fe-doped SrTiO ₃ / BaTiO ₃ multilayer films with different Fe concentrations deposited on alumina substrate, (b) the zoom of (200) planes.	109
5.16 FESEM images with magnification of 50,000 of SrTiO ₃ /BaTiO ₃ multilayer films deposited on alumina substrate (a) undoped, (b) 2 wt%, (c) 4 wt% and (d) 8wt% Fe doping concentrations.	110
5.17 Cross-section FESEM images of a device made from 2 wt% Fe-doped SrTiO ₃ /BaTiO ₃ multilayer films deposited on alumina substrate.	111
5.18 The dynamic response to ethanol with concentration ranging 100 to 1000 ppm of SrTiO ₃ /BaTiO ₃ multilayer films doped with (a) Fe 2 wt% operating at 250 °C, (b) Fe 2 wt% operating at 350 °C, (c) Fe 8 wt% operating at 250 °C, and (d) and Fe 8 wt% operating at 350 °C with increasing ethanol concentration in the range of 100-1000 ppm.	113
5.19 Sensitivity of the films doped with (a) Fe 2 wt% operating at 250 °C, (b) Fe 2 wt% operating at 350 °C, (c) Fe 8 wt% operating at 250 °C and (d) Fe 8 wt% operating at 350 °C.	116
5.20 Comparison of ethanol sensitivity of the films doped with Fe 2 wt% and 8 wt% with different concentrations at operating temperature of 350 °C.	118

Figure	Page
5.21 The frequency dependence of dielectric constant of BaTiO ₃ with applied voltage at (a) 0 to 25 volt and (b) 0 to -25 volt at room temperature.	120
5.22 The frequency dependence of dielectric constant of SrTiO ₃ with applied voltage from 0 to 25 volt at room temperature.	122
5.23 The frequency dependence of dielectric constant of SrTiO ₃ /BaTiO ₃ films with applied voltage at (a) 0 to 25 volt and (b) 0 to -25 volt at room temperature.	124
5.24 The room temperature dielectric constant as a function of (a) applied electric field and (b) volt of BaTiO ₃ /SrTiO ₃ multilayer films. .	125
5.25 The value of dielectric constant of all the films without applied voltage measured at room temperature.	126
5.26 Schematic presentation of (a) perovskite unit cell of SrTiO ₃ and BaTiO ₃ (b) formation of SrTiO ₃ /BaTiO ₃ superlattices. The arrows denote the induced compressive stress in BaTiO ₃ and the tensile stress in SrTiO ₃	127
5.27 Dielectric constant of BaTiO ₃ plotted as a function of average grain diameter reported by Arlt et al.	129
5.28 Grain size dependence of permittivity of BaTiO ₃ ceramics	130
5.29 The frequency dependence of capacitance and loss tangent of all the films without applied voltage measured at room temperature. .	131

Figure	Page
5.30 The frequency dependence of capacitance and loss tangent of SrTiO ₃ /BaTiO ₃ films after exposure to gamma at dose of 5, 10 and 30 kGy.	135
5.31 The dielectric constant of SrTiO ₃ /BaTiO ₃ films as a function of frequency with various gamma irradiations.	136
5.32 The (a) capacitance (b) dielectric constant and (c) loss tangent of SrTiO ₃ /BaTiO ₃ films exposed to gamma ray at dose of 10 kGy and heating at 100 °C for 30 min.	137
5.33 The (a) capacitance (b) dielectric constant and (c) loss tangent of SrTiO ₃ /BaTiO ₃ films exposed to gamma ray at dose of 10 kGy and heating at 100 °C for 30 min.	138

CHAPTER I

INTRODUCTION

1.1 Thesis motivation

At present, there is an ongoing demand for developing the technique to measure the gas concentration for a wide range of applications such as agricultural industries, biotechnological process and monitoring in domestic and industrial environmental pollutant as well as automotive exhausting. For example, in agricultural field carbon dioxide (CO_2) is one factor for plant growth. Namely, the improvement in growth rate of plants can be achieved by controlling CO_2 concentration. Moreover, CO_2 is utilized for food packaging in biotechnological process to extend storage life of food such as meat, vegetable and fruits. Contrastively, high CO_2 concentration can damage human organ involving respiration system. The increasing CO_2 can cause green house effect and ozone depletion resulting in global warming. Most commercial CO_2 gas sensors are based on optical measurement. It has been known that CO_2 molecules absorb spectra in range of infrared at wavelengths of $4.3 \mu\text{m}$ [1]. Moreover, optical gas sensors can operate by detecting the refractive index that obtains via various methods including interference spectra, reflected or transmitted light intensity and surface plasmon resonance [2, 3, 4]. Nevertheless, optical gas sensor is too expensive for some applications at which low cost sensor is needed. From these reasons, solid state gas sensors based on semiconducting metal oxide could be a good candidate due to their low cost, small size, the ease to integrate in electronic device, simplicity for fabrication and measurement as well as durability. The working principle of semiconducting

gas sensor device is simple. It functions by measuring the change in electrical resistance of sensor as it exposes to target gas concentration. Metal oxides such as SnO_2 , TiO_2 , ZnO and WO_3 are conventional gas sensor which have been widely used for detecting NO_2 , H_2S , NH_3 and ethanol vapor [5, 6, 7]. However, utilization of these materials for monitoring CO_2 and CO is not widespread due to their poor sensitivity. Many researchers have made an effort to improve their sensitivity and selectivity. Stankova et al. modified WO_3 with seven different materials (Pt, Au, Ag, Ti, SnO_2 , ZnO and ITO (indium tin oxide)) by sputtering technique to study the gas sensing properties in various gases at low operating temperature in the range of 110-260 °C [5]. They observed that pure WO_3 can not respond to CO in the range of 1000-3500 ppm while with other gases such as H_2S , NO_2 , CH_4 and NH_3 it can monitor in spite of low concentration in the range of 1-3.5 ppm for H_2S , 1-10 ppm for NO_2 , 100-350 ppm for CH_4 and 100-1000 ppm for NH_3 . They further indicated that CO sensing property of WO_3 can be improved by doping with only two materials which are Au and SnO_2 .

Among such metal oxide materials, semiconducting perovskite such as barium titanate (BaTiO_3 or BTO) and strontium titanate (SrTiO_3 or STO) have received attention for fabricating as gas sensor to detect toxic and combustible gases such as CO_2 , CO as well as O_2 due to having high melting temperature and stability in microstructural morphology under high temperature and chemical atmosphere [8, 9, 10]. Work by Ishihara et al. studied on gas sensing properties of CuO-BaTiO_3 in various gases including H_2 , CH_4 , CO , CO_2 as well as H_2O (humidity) [11]. They observed that CuO-BaTiO_3 added with Ag showed sensing response to CO_2 much better than other gases for which the sensitivity to CO_2 was approximately 40 at the operating temperature of 425 °C, whereas the sensitivity of that to CO , H_2 , H_2O and CH_4 was found to be round 10, 3, 2 and 1, respectively. The CO_2 sensitivity is 4-40 times higher than that of the sensor under the other four types of gases at same operating conditions. Their work pointed out that the sensor made from Ag added CuO-BaTiO_3 has selectivity to CO_2 detection. However, the mechanisms for CO_2 selectivity obtained by

adding Ag into CuO-BaTiO₃ are not clear. Herran et al. used sputtering technique to prepare CuO-BaTiO₃ films and studied the sensing characteristic under CO₂ atmosphere [12]. They observed that the sensor quickly responded to CO₂ of which the response and recovery times are around 2 and 3 min, respectively and the sensitivity is approximately 15 operating at 300 °C. For SrTiO₃, most researchers have taken an interest in its O₂ sensing property. Hu et al. investigated O₂ sensing characteristic at low temperature of SrTiO₃ fabricated by high energy ball milling and conventional screen-printing techniques [13]. They found that the highest sensitivity was around 6 at operating temperature of 40 °C which is near the human body temperature. Work by Hara et al. reported the oxygen sensing performance of SrTiO₃ thin film prepared using atomic layer deposition [14]. Their results presented the sensor based on SrTiO₃ thin film exhibited high oxygen sensitivity under low O₂ concentration in order of ppb (parts per billion) at room temperature. They mentioned that this sensitivity is sufficient to detect oxygen contamination in semiconductor manufacturing processes. Work done by Gerblinger et al. have been studied the O₂ sensing performance of SrTiO₃ at high operating temperature in the range of 650-1100 °C [15]. They found that the sensitivity was in the 1-1.6 depending on operating temperature and the maximum sensitivity can be obtained at the operating temperature of 1000 °C. The good point of SrTiO₃ is that it can respond to O₂ in wide range of temperature from room temperature to high temperature. In addition, the sensing characteristics of BaTiO₃ and SrTiO₃ in a variety of gases atmosphere such as H₂S [10, 16], H₂ [17], NH₃ [18], liquid petroleum gas (LPG) [19], hydrocarbon [20] and acetone [21] have also been examined. Nevertheless, there was not many research groups investigated on ethanal sensing performance for BaTiO₃ and SrTiO₃ materials. From literature review, materials mostly used for detecting ethanol vapor are WO₃, SnO₂, ZnO, TiO₂ [22, 23, 24]. Wisitsoraat et al. studied gas sensing properties of WO₃ and SnO₂ grown by ion-assisted electron beam evaporation [22]. The sensors were tested with CO at concentration of 1000 ppm and ethanol vapor at concentration of 1% in the temperature range between 200 and 350 °C.

Their results showed that the SnO₂ thin film has higher sensitivity to both CO and ethanol vapor than the WO₃ thin film. In comparison between two types of testing gases, both sensors showed the best gas sensing performance to ethanol vapor. The sensitivity of SnO₂ exposed to CO and ethanol vapor was about 5 and 7 operating at 300 °C, respectively whereas that of WO₃ presented in CO and ethanol vapor was around 1.5 and 2, respectively.

In addition, they found that CO and ethanol sensitivity can be improved by increasing oxygen-ion addition during e-beam evaporation. The enhancement in gas sensitivity may be due to the fact that the addition of oxygen-ions reoxidizes the film generating the reduction in the number of oxygen vacancies. Chen et al. reported a new alcohol sensor using ultrathin single crystalline WO₃ nanoplate prepared by a topochemical transformation process on the basis of intercalation chemistry [25]. The WO₃ nanoplate sensor exhibited extremely sensitivity to alcohols e.g. methanol, ethanol, isopropanol and butanol. They found that the sensitivity of WO₃ nanoplate sensor operating at 300 °C was approximately 161 for butanol at 100 ppm, 33 for methanol at 300 ppm, 70 for ethanol at 200 ppm and 75 for isopropanol at 200 ppm. They also found that the response and recovery times of the sensor were shorter than 15 second for all the test alcohols. Moreover, they compared the gas sensing performance of WO₃ nanoparticle sensor to alcohol. Their results exhibited that the sensitivity of WO₃ nanoparticle sensors was smaller than those of the sensor made of WO₃ nanoplate. The obtained sensitivities of WO₃ nanoparticle sensors operating at 300 °C were about 13 for butanol at 100 ppm, 9 for methanol at 300 ppm, 7 for ethanol at 200 ppm and 5 for isopropanol at 200 ppm. Chen et al. noticed that the enhancement in alcohol sensing properties of WO₃ nanoplate can be attributed to ultrathin platelike morphology and loosely assembled structure observed in WO₃ nanoplate yielding increase in absorption and fast diffusion of alcohol molecules. Another investigation to alcohol sensing was done by Wang et al. [26]. The sensors were fabricated from Fe-doped SnO₂ nanofibers synthesized by an electrospinning method. They observed that the Fe-doped SnO₂ nanofiber sensors had a high sensitivity to al-

cohol of which the sensitivity was found to be about 7, 15, 30 and 125 as the sensors exposed to alcohol concentrations of 50, 100, 200 and 1000 ppm, respectively which measured at the temperature of 300 °C. On comparing to sensitivity of the sensor with and without nanostructure at same operating conditions, for example SnO₂, it has been seen that the sensors with nanostructure had outstanding sensitivity compared with the sensors without nanostructure. The improvement in gas sensitivity observed for nanostructure sensors is due to the increase in surface interaction of the sensor. However, limitation of nanostructure gas sensor is that its morphological feature is easier to be deformed at high temperature leading to difficulty for determining gas sensitivity.

There are many parameters for gas sensing characterization indicating that the materials have high sensing performance including sensitivity, response time (the time taken sensor signal to reach 90% of its steady state), recovery time (the time taken the sensor to be within 10% of the initial value), selectivity and long term stability [27]. Among of these parameters, sensitivity is one of the most important parameter. If the value of sensitivity for a particular gas is high pointing that the material is a very good sensor. It was proposed that the gas sensitivity can be promoted by reducing the grain size which induces a large surface to volume ratio [28, 24, 29]. Generally, the gas sensing properties are based on reaction between adsorbed oxygen molecules and gases which could be took place on the film surface [30, 31]. Certainly, the reduction in grain size or the presence of porosity in the materials is one of the essential factors to improve the sensitivity of gas sensors. Kuwabara and Kim et al. reported that pores in the Ba_xSr_{1-x}TiO₃ materials can support oxygen adsorbed at the grain boundary [32, 33, 34]. Several approaches have been employed to enhance the surface to volume ratio through variety of methods such as modifying materials with additive as well as using spacial technique to prepare materials [35, 36]. However, doping is simple way which can apply to any film preparation, especially with a sol-gel technique which was used to prepare BaTiO₃ and SrTiO₃ films in this thesis work. It has been suggested that not only with metal such as Fe, Au, W and Al [28, 24, 29, 37] but also metal

oxide like CuO, CeO₂ [38, 39] can decrease that ratio. Chaudhari et al. studied the effect of three dopants including CuO, CdO and Pd on liquid petroleum (LPG) sensitivity for BaTiO₃ films as well as optimal operating temperature [19]. They compared the sensitivity for four types of films (pure BaTiO₃, CdO-doped BaTiO₃, CuO/CdO-doped BaTiO₃ and Pd/CdO/CuO-doped BaTiO₃). Their work presented that sensitivity of the films to LPG concentration of 1000 ppm increased from 0.45 for pure BaTiO₃ to 0.95 for Pd/CuO/CdO-doped BaTiO₃ whereas the optimal operating temperature of the films also decreased from 300 °C for pure BaTiO₃ to 225 °C for Pd/CdO/CuO-doped BaTiO₃. Work by Tianshu et al. reported Cd-doped SnO₂ has an extreme ethanol sensitivity of which the sensitivity value was approximately 200 at low concentration of 80 ppm operating at 225 °C [40]. In addition, they further pointed out that with Cd doping the response and recovery time could reduce. They noticed that the better sensing performance of SnO₂ achieved through doping Cd was due to reduction in crystalline size and existence of porosity in the materials [41]. Neri et al. fabricated resistive oxygen sensor for application in diesel engines car under real driving conditions. The sensors were made from SrTi_{0.4}Fe_{0.6}O_{2.8} powder prepared by self propagating high-temperature synthesis and subsequent ball-milling treatment. Oxygen sensing performance of SrTi_{0.4}Fe_{0.6}O_{2.8} sensor was also compared to that of Bosch commercial oxygen sensor. The signal output indicated that their sensor responded quickly to oxygen concentration variations as the Bosch probe. In addition, Fe-doped BaTiO₃ and Fe-doped SrTiO₃ are multiferroic materials that exhibit ferroelectricity and ferromagnetism under the same physical conditions. Recently, there are many reports on the effect of the Fe doping concentration in BaTiO₃ and SrTiO₃ on room temperature ferromagnetism [42, 43]. By modifying SrTiO₃ with Fe ions, the ferroelectric Curie temperature (T_c) could move to higher temperature as high as 200 °C, whereas an antiferromagnetic behavior existed in SrTiO₃ doped with low Fe concentration [43].

Ethanol or ethyl alcohol is one type of alcohol faced in our daily life. Ethanol sensor have been widely used in many applications such as alcohol gas checker in

breath of car driver, wide making process, food and chemical industries. Especially in the field of driver alcohol checking, alcohol detector is very necessary due to the fact that many occurred accidents at present are mostly caused by drivers consuming alcohol and driving. Thus, the way to fabricate alcohol detector having high efficiency and low cost has been required to reduce accidents. From the literature reviews we read including as for our knowledge, there was no report on ethanal sensor for BaTiO₃ and SrTiO₃ multilayer films. Moreover, based on assumption metal doping into the films can reduce grain size leading to enhancement in surface to volume ratio, thus in this thesis work, we studied the ethanol sensing characteristic for Fe-doped BaTiO₃ and Fe-doped SrTiO₃ multilayer films for different Fe concentrations.

Besides gas sensing properties, electrical properties of BaTiO₃ and SrTiO₃ have also been extensively investigated due to their high dielectric constant and electric field tunability, which usually occur near transition temperature or Curie temperature (T_c). The materials with high dielectric constant and tunability is widely utilized in many applications such as optoelectronic device, dynamic random access memories (DRAMs) and tunable microwave component. The dielectric constant of BaTiO₃ bulk is approximately 10000 at temperature 393 K while the dielectric constant of BaTiO₃ thin films is in the 1000-3000 range by varying temperature from 390 K to 430 K [44, 45]. The dielectric constant of SrTiO₃ readily responds to a small electric field at lower temperature than that of BaTiO₃. In other words, the dielectric constant of SrTiO₃ bulk is approximately 30000 at temperature 4 K while the dielectric constant of SrTiO₃ thin films is in the 2000-5000 range at temperature from 30 to 100 K [46, 47]. Because the dielectric constant of both types responds to an electric field in different temperature range, many attempts were made to enhance or tune dielectric constant near room temperature. It was reported that the common way to improve dielectric properties is to add stress and strain into the lattice through two ways of film preparation [48, 49, 50, 51]. First way is done by growing film in combined form of Ba_{1-x}Sr_xTiO₃ compound [48, 52]. Second way is to fabricate artificial film by

means of superlattice of BaTiO_3 and SrTiO_3 which have a good lattice matching [49, 50, 51]. The first $\text{BaTiO}_3/\text{SrTiO}_3$ artificial superlattice was successfully made in 1992 by Iijima et al. using reactive evaporation [53]. After that several techniques such as pulse laser deposition [54, 55], sputtering [50, 56], metal organic chemical vapor deposition [57], molecular beam laser [58], screen printing method [59] and sol-gel method [49, 60] has been employed to deposit $\text{BaTiO}_3/\text{SrTiO}_3$ multilayer films.

Wang et al. proved that the dielectric constant and tunability of $\text{Ba}_{1-x}\text{Sr}_x\text{TiO}_3$ can be tailored by adjusting the Ba/Sr ratio [52]. Gim et al. investigated dielectric properties of $\text{Ba}_{1-x}\text{Sr}_x\text{TiO}_3$ films grown by laser ablation on LaAlO_3 substrates, where the x values were varied in the 0.1-0.9 range [61]. Their experiment showed that the capacitance of the films changes by adjusting the values of x which the maximum value of measured capacitance of $\text{Ba}_{1-x}\text{Sr}_x\text{TiO}_3$ was obtained at $x=0.4$ of which the capacitance was approximately 1400 fF at room temperature without applied voltage. They also found that at $x=0.4$, the $\text{Ba}_{1-x}\text{Sr}_x\text{TiO}_3$ films exhibited the highest tunability of capacitance which was around 30% with dc applied voltage of 40 kV/cm measured at room temperature. However, some literatures compared the value of dielectric constant between $\text{Ba}_{1-x}\text{Sr}_x\text{TiO}_3$ and artificial $\text{SrTiO}_3/\text{BaTiO}_3$ superlattices. Kim et al. used pulsed laser deposition technique to study the dielectric properties of $\text{Ba}_{0.5}\text{Sr}_{0.5}\text{TiO}_3$ and $\text{SrTiO}_3/\text{BaTiO}_3$ multilayer film [54]. They observed that the dielectric constant value of multilayer films was higher than that of $\text{Ba}_{0.5}\text{Sr}_{0.5}\text{TiO}_3$ films of which the value was about 520 whereas the dielectric constant for multilayer films was found to be about 680 at 100 kHz measuring at room temperature. The improvement of dielectric properties observed in multilayer films was also confirmed in work by Hu et al. [55]. They prepared three types of films including $\text{Ba}_{0.5}\text{Sr}_{0.5}\text{TiO}_3$, $\text{Ba}_{0.5}\text{Sr}_{0.5}\text{TiO}_3/\text{Ba}_{0.5}\text{Sr}_{0.5}\text{TiO}_3$ and $\text{BaTiO}_3/\text{SrTiO}_3$ by using pulsed laser deposition technique. Their work presented that the films with homolayered structure ($\text{Ba}_{0.5}\text{Sr}_{0.5}\text{TiO}_3/\text{Ba}_{0.5}\text{Sr}_{0.5}\text{TiO}_3$) showed a tiny enhancement in dielectric constant compared with $\text{Ba}_{0.5}\text{Sr}_{0.5}\text{TiO}_3$ while that of heterolayered structure ($\text{BaTiO}_3/\text{SrTiO}_3$) could drastically increase.

They pointed out that the enhancement in dielectric constant of the films with heterolayered structure is due to the mechanical strain developed in the structure because of the lattice mismatch between the adjacent layer. The strain induced by lattice mismatch in this $\text{BaTiO}_3/\text{SrTiO}_3$ superlattice was also investigated by using the theoretical calculations [62, 63, 64]. It has been additionally proposed that with increasing the number of stacking layer, large strain distortion could be introduced in the in-plane direction as a consequence of improvement in the dielectric constant and tunability [65, 66]. Li et al. discussed the effect of layer number (n) of $(\text{SrTiO}_3/\text{BaTiO}_3)_n$ multilayer films on their dielectric properties which operated at room temperature without applied electric field [65]. The multilayer films were grown by a double target radio frequency (RF) magnetron sputtering technique with various layer numbers of 1, 2 and 4 as well as the thickness of all films was fixed at 450 nm. They observed that the dielectric constant of $(\text{SrTiO}_3/\text{BaTiO}_3)_n$ multilayer films increases from 270, 375 to 420 when the layer number of film growth increases from 1, 2 to 4, respectively. Moreover, they also noticed that the tunability of multilayer films can be increased with increasing the number of layers. The improvement of dielectric properties observed in $\text{SrTiO}_3/\text{BaTiO}_3$ multilayer films by increasing the stacking layer was also reported in work by Guigues et al [66]. Their results showed that the dielectric constant of multilayer films increases from 56 to 102 as the stacking period increases from 1 to 5 with the film thickness in the range of 65-85 nm. They also found that with increasing the layer of number, dielectric tunability enhances of which tunability was approximately 15% for 1 period and increases up to 37% for 5 periods. This increment of dielectric properties can be caused by internal strain which increases with the number of stacking period generating an improvement in dielectric constant of multilayer films. In this thesis work, four types of films including uniform BaTiO_3 , uniform SrTiO_3 , $\text{SrTiO}_3/\text{BaTiO}_3$ multilayer and Fe-doped $\text{SrTiO}_3/\text{BaTiO}_3$ multilayer were fabricated as a capacitor to compare their dielectric constant.

Furthermore, a number of authors reported the influence of high energy electromagnetic radiation such as gamma rays and X-rays on optical properties

of these materials. Kongwut et al. discussed the effect of gamma irradiation on optical properties of BaTiO₃ and Fe-doped BaTiO₃ thin films [67]. They observed the change in transmittance spectra of the films after exposure to gamma irradiation at 15 kGy of which the transmittance decreased by 4% for undoped films but by 11% for Fe-doped BaTiO₃ films. Since the Fe-doped films was more effective to gamma irradiation than undoped BaTiO₃ films, they further studied influence of gamma irradiation on the refractive index of Fe-doped BaTiO₃. Their work reported that the refractive index and extinction coefficient of the films also increased after irradiation to higher gamma doses. They did not report the change in electrical properties of such those films. In general, not only optical properties could be changed by gamma irradiation but the change in electrical properties of various materials were also published. Arshak et al. observed that the capacitance of manganese phthalocyanine (MnPc) thick film decreased from 50 pF to 30 pF as the films were irradiated to gamma ray with the doses up to 27 kGy [68]. However, they noticed that after exposure to gamma ray ranging within 7.2-25 kGy the films showed the increase in capacitance tunability. While another their work investigated electrical properties on bismuth germinate films, they found that capacitance values of films had gradually enhanced from 2.97 pF up to 7.09 pF as the films were exposed to gamma ray at dose of 2.44 mGy [69]. From work by Arshak et al., they indicated that each of materials dissimilar reacts with gamma ray at different doses. Work by Selcuk et al. have been discussed influence of gamma irradiation on dielectric characteristics of SnO₂ thin films [70]. They found that capacitance-voltage (C-V) curve moves towards the positive voltage with increasing the irradiation dose. In addition, they observed that the dielectric constant of the films gradually decreased from 6.94 to 5.97 as the gamma dose increased to 500 kGy. The variation of dielectric constant of TlSnO₂ single crystal effected by gamma irradiation was also noticed in work by Mustafaeva et al. [71]. Their results presented that the dielectric constant of TlSnO₂ sample rapidly increased from 12 to 32 when the gamma dose increased to 1×10^4 rad (1 rad = 0.01 Gy) and beyond the gamma dose of 1×10^4 rad the dielectric constant gradually de-

creased from 32 to 22 for the dose of 225×10^4 rad. Nevertheless, this reduced value of dielectric constant observed as the samples exposed to high gamma dose remained higher than that for unirradiation TlSnO_2 sample. Tugluoglu et al. also reported that the dielectric constant of $\text{Au/SnO}_2/\text{n-Si}$ (MOS) structures increased by gamma irradiation [72]. Their dielectric constant increased from 1.06 to 1.18 as the gamma dose increased up to 500 kGy. The increment of dielectric constant with increasing gamma dose also observed in work by Tataroglu et al. of which the dielectric constant of $\text{Al/SiO}_2/\text{pSi}$ (MIS) Schottky diodes rose from 0.015 to 0.019 with increasing gamma dose up to 500 kGy [73]. As mentioned earlier, gamma irradiation has strongly affected the electrical properties of the materials. However, based on the lack of existing data for electrical properties of BaTiO_3 and SrTiO_3 before and after gamma irradiation, it is interesting to study further beyond Kongwut et al.'s work.

In addition, since BaTiO_3 and SrTiO_3 present excellent optical properties such as large electro-optical coefficient, low optical loss and high optical transparency in visible region, these materials could be used in optoelectronic devices [74, 75]. An application of these types of films as insulating layer in flat panel displays (FPD) comprising of the layer of metal-electrode/phosphor/insulator/transparent electrode/glass has recently been reported [76, 77]. It has been reported that the optical properties such as optical transmittance were influenced by defects, impurity and grain boundary. A large number of works reported on optical, electrical (dielectric or ferroelectric) properties of these types of films, which are affected by many factors such as growth condition, the annealing temperature [78], the type of substrate or buffer layer used [79, 80], thickness [81], the doping [82] as well as microstructure [83]. Also, relatively few works dealt with the optical properties of $\text{SrTiO}_3/\text{BaTiO}_3$ multilayered films despite of much growing interest in these films for device applications [84, 85].

In the first stage of this thesis work due to the ease of experimental set up, we focused on optical properties of $\text{SrTiO}_3/\text{BaTiO}_3$ multilayered thin films deposited on a substrate made of optical transparent conducting indium tin oxide

(ITO) on glass. The annealing temperature was varied to achieve the optimal temperature for crystallinity. The temperature was changed from 300 °C and limited to 650 °C to avoid softening and deformation of the glass substrate. The effect of the annealing temperature SrTiO₃/BaTiO₃ multilayered thin films with different thickness on optical band gap and complex refractive index of the films was also investigated. After that, we move on to characterize the ethanol sensing properties of Fe-doped SrTiO₃/BaTiO₃ multilayered thin films deposited on insulating alumina substrate. In this stage, we also investigated the influence of Fe doping concentrations on the crystal structure and surface morphology of the films. The last stage, the dielectric properties of the films including uniform BaTiO₃, SrTiO₃, SrTiO₃/BaTiO₃ and Fe-doped SrTiO₃/BaTiO₃ multilayered films were investigated. In addition, the effect of gamma irradiation on dielectric properties of SrTiO₃/BaTiO₃ multilayered films was examined.

In this thesis, we study variety of applications in the same material by adjusting the parameter for film growth so that this work is no resemblance with most research in recent day. For instance, in case of dielectric measurement, which mostly carried out in the high frequency range of GHz and wide temperature range. Nevertheless, due to technical difficulty of carrying out measurements in the high frequency range and low temperature, this is why we are also interested in other their applications such as optical and gas sensing properties.

1.2 The aims of this thesis are:

1. To prepare barium titanate and strontium titanate thin films using a sol-gel spin coating technique.
2. To investigate the effects of film growing parameters such as annealing temperature and metal doping on crystal structure, surface morphology and optical properties of the films.
3. To fabricate capacitors and gas-sensing devices.

4. To analyze gas sensing properties of barium titanate and strontium titanate gas sensors.
5. To study the dielectric properties of barium titanate and strontium titanate capacitors.

1.3 Overview of this thesis

This thesis is divided into 7 chapters. Chapter I includes introduction, motivation and objective of this thesis work. Chapter II describes the necessary background for example crystal structure and some general properties of BaTiO_3 and SrTiO_3 materials, concept of sol gel process, interference conditions in a thin film, dielectric and gas sensor. The details of techniques used for characterizations which include X-ray diffraction, X-ray absorption spectroscopy, field emission scanning electron microscopy, atomic force microscopy, ultraviolet-visible spectroscopy as well as determination of refractive index, film thickness, energy gap and Urbach energy from transmission data are covered in chapter III. In chapter IV, film preparation including the condition for film deposition is presented. In addition, fabrication of device as well as the measurement for gas sensing and electrical properties are explained. Chapter V describes results and discussion which dedicate to three main properties (optical, electrical and gas sensing properties). Finally, in chapter VI, the conclusions of the thesis will be presented.

CHAPTER II

THEORETICAL BACKGROUND

In this chapter, essential background in this thesis work will be presented beginning with the details of the crystal structure of barium titanate and strontium titanate materials as well as their interesting properties. Next, sol-gel spin coating process used to form thin films will be described. In the last section of this chapter, the background about interference condition in the thin films, dielectric properties and gas sensor mechanism will be also be presented.

2.1 BaTiO₃ material

Barium titanate (BaTiO₃, BTO) belongs to the family of perovskite oxides structure with the formula ABO₃ at which A and B are cations with different sizes. The larger divalent ions (Ba²⁺) occupy the A site which is located at four corners of the cube. The B cation represented tetravalent ions (Ti⁴⁺) is coordinated at center position surrounded with 6 oxygen ions. The Ti⁴⁺ ion is fit into octahedral cage forming by oxygen ions. The unit cell of perovskite cubic structure is shown in Fig. 2.1.

BaTiO₃ has ferroelectric behavior. At temperature below a transition temperature, so called, Curie temperature (T_c) of 120 °C [86], the Ba²⁺ and Ti⁴⁺ ions are displaced with O²⁻ ions resulting in distortion of octahedral which generates a tetragonal structure with the lattice constants a and c as presented in Fig. 2.2(a). Because of asymmetry in the unit cell, a hugely spontaneous polarization is took place which gives a net dipole moment along to c -axis ([001] direction). The ma-

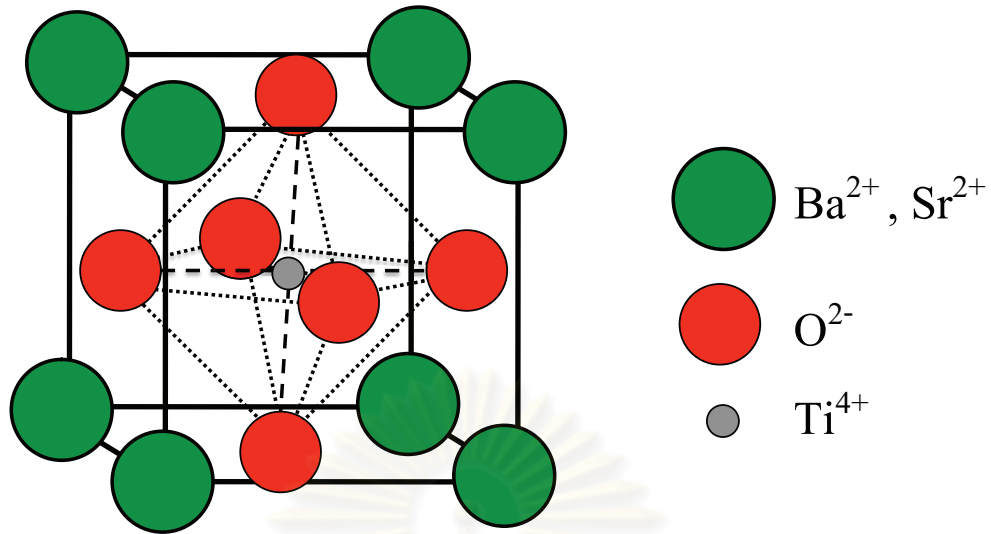


Figure 2.1: The unit cell of perovskite cubic structure.

material in this configuration is a ferroelectric. At above Curie temperature ($T > T_c$), there is enough thermal energy (kT) for making the Ti^{4+} ions to move randomly leading to have no fixed asymmetry. The cell is formed perfectly cubic structure with the lattice parameter as illustrated in Fig. 2.2(b). The material does not exhibit spontaneous polarization but generating a paraelectric phase.

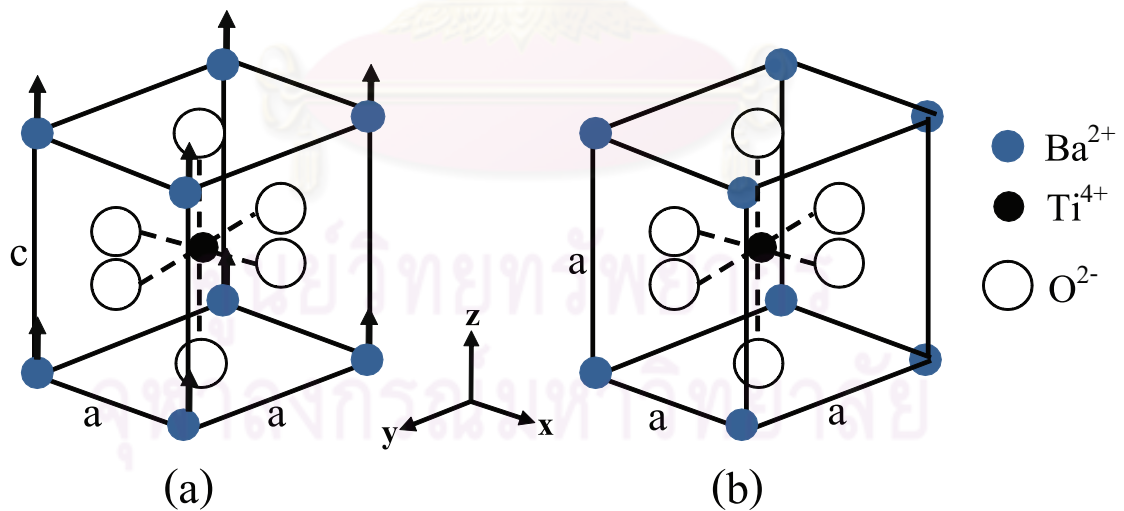


Figure 2.2: The crystal structure of BaTiO_3 ; (a) below T_c , the structure is tetragonal and (b) above T_c , the structure is cubic.

The polarization behavior as a function of electric field in paraelectric and

ferroelectric material is demonstrated in Fig. 2.3(a) and (b), respectively. For paraelectric material, there is no net dipole moment when an electric field equal to zero whereas in the case of ferroelectric material, the hysteresis loop of polarization can be obtained. On the other hand, a net dipole moment is still remain when the applied electric field is removed. In addition, BaTiO_3 has more another two phase transitions. Orthorhombic deformation of BaTiO_3 could be occurred at temperature of 5°C . At below the temperature of -70°C , BaTiO_3 undergoes to a rhombohedral phase [86]. The transformation in crystallographic structure is caused by changing the direction of dipole moments. In other words, the direction of dipole moments changes to $[011]$ and $[111]$ direction for orthorhombic and rhombohedral structure, respectively. The crystallographic changes and physical properties of BaTiO_3 bulk are given in Table 2.1.

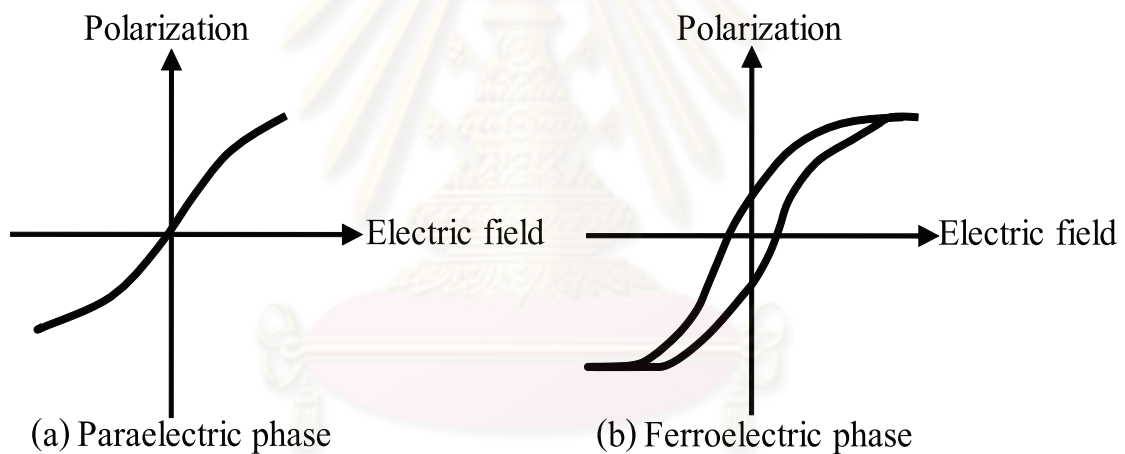


Figure 2.3: Polarization behavior as a function of electric field in ferroelectric material (a) above T_c and (b) below T_c .

Because of its ferroelectric property, BaTiO_3 has been used in wide range of applications such as dynamic random access memories (DRAMs), non-volatile ferroelectric random access memories, thermistor as well as optoelectronic device such as insulating layer in flat panel screen due to its excellent optical properties.

Table 2.1: The physical properties of bulk BaTiO₃.

Physical properties	
Crystal structure	Cubic ($T \geq 120$ °C), Tetragonal (5 °C $< T < 120$ °C), Orthorhombic (-70 °C $< T \leq 5$ °C) and Rhombohedral ($T \leq -70$ °C)
Lattice parameters	$a=3.992$ Å, $c=4.036$ Å (Tetragonal structure)
Density	6.02 g/cm ³
Melting point	1650 °C

2.2 SrTiO₃ material

Strontium titanate (SrTiO₃, STO) is an incipient ferroelectric with a very huge dielectric constant or relative permittivity (ϵ_r). A ferroelectric phase can be induced at a low temperature by impurities, external stress and external strain. SrTiO₃ has pseudo-cubic structure with lattice constant of 3.905 Å at room temperature [87]. At the temperature less than -168 °C, it undergoes a tetragonal structure [88, 89]. Some physical properties of bulk SrTiO₃ are presented in Table 2.2.

Table 2.2: The physical properties of bulk SrTiO₃.

Physical properties	
Crystal structure	Cubic ($T > -168$ °C) and Tetragonal ($T \leq -168$ °C)
Lattice parameters	$a=3.905$ Å (Cubic structure)
Density	5.17 g/cm ³
Melting point	2080 °C

Fig. 2.4 illustrates temperature dependence of dielectric permittivity of bulk SrTiO₃ for at an applied DC electric field of 0 , 5 V/ μ m and 10 V/ μ m [90]. At near phase transition temperature (Curie temperature of 105 K), the value of ϵ_r is very

large which is in the order of 10^3 with no DC bias field and decreases to around 900 and 600 at DC bias field of $5 \text{ V}/\mu\text{m}$ and $10 \text{ V}/\mu\text{m}$, respectively. Above this phase transition temperature, dielectric permittivity abruptly decreases as temperature increases which obeys Curie-Weiss law [91]:

$$\varepsilon_r = \frac{C}{T - T_c}, T > T_c \quad (2.1)$$

where C is a constant called the Curie constant and T_c is the Curie temperature. The change in dielectric permittivity opposed to a DC bias electric field is more sensitive at a low temperature. At Curie temperature, however, the permittivity of SrTiO_3 film material is smaller than that of bulk SrTiO_3 single crystal ($\varepsilon_r \sim 900$ for films and ~ 1200 for bulk single crystal). Contrastively, the permittivity of both materials has rather same value around 300 at near room temperature [92, 93].

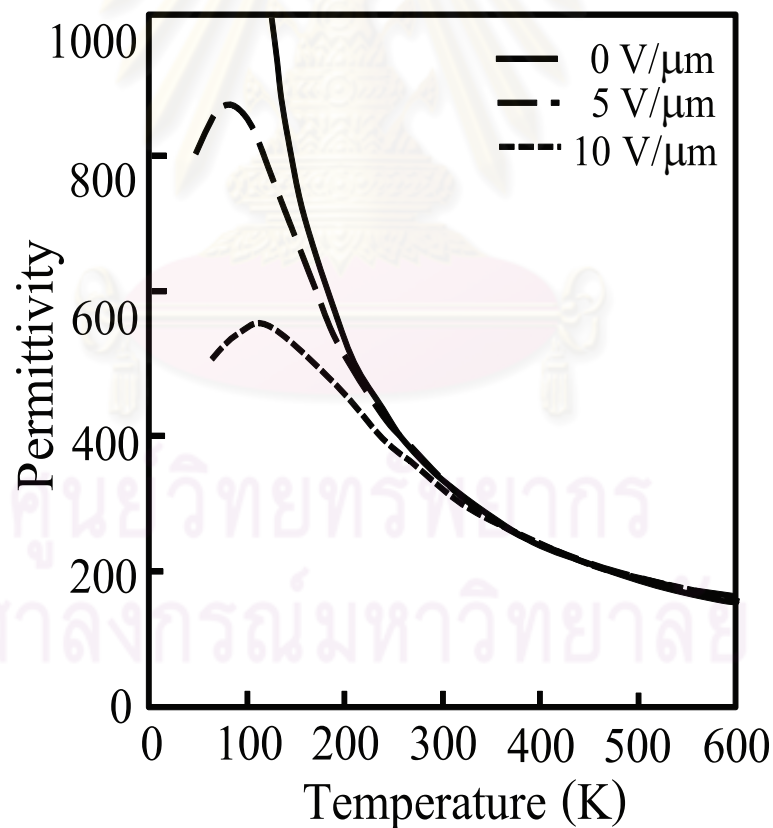


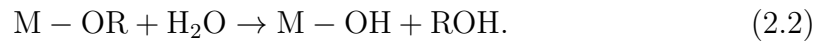
Figure 2.4: Permittivity versus temperature of bulk SrTiO_3 for at DC bias electric field of 0, $5 \text{ V}/\mu\text{m}$ and $10 \text{ V}/\mu\text{m}$ [90].

Since SrTiO_3 has not only prominently dielectric constant but also low dielectric loss tangent even at high frequency (> 1 GHz), it has been widely used for RF and microwave tuning applications such as harmonic generators, tuneable resonators, high density capacitors and microelectromechanical (MEM) switches [94, 95, 96, 97]. In addition, SrTiO_3 is used as buffer layer or substrate for epitaxial growth [98, 99, 100] as well as gas sensor detecting at high temperature, e.g. automotive exhaust gas because of its high melting point, stability in surface morphology in high temperature thermal and chemical atmosphere [13, 101, 102].

2.3 Sol-gel process

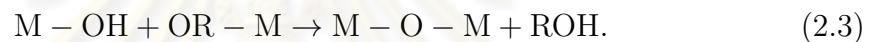
The sol-gel process is a versatile chemical solution method for preparing ceramic, metal oxide based thin films at low temperature. This sol-gel technique is widely used during the several decades because it can be alternative to conventional technique such as sputtering, evaporation, chemical vapor deposition, inductively couple plasma and plasma spray for depositing thin material coating. Particularly, for growing the ferroelectric materials which include large compound groups of metal oxide, the sol-gel process has a numerous utility for depositing such material. The advantage of sol-gel process is ease of doping metal and modifying the composition of the film. In this thesis, we used iron (Fe) for doping into the films. To describe the sol-gel process, the term sol-gel is essential to introduce. Sol-gel is derived from two components of the reaction that are sol and gel. The sol refers to discrete colloidal suspension that can be initially formed in a solution and the gel is the inertial network structure that forms after continual growth with in the solution. The starting materials used in the preparation of sol are usually metal alkoxides. Typically, there are two reactions that can occur during sol-gel process which can be broken down into two basic steps, hydrolysis and condensation as the following:

1) Hydrolysis of metal alkoxides



Hydrolysis reaction occurs when the metal alkoxides ($M - OR$) is mixed with H_2O . The reaction will be completed when OR (alkyl group) is replaced by OH (hydroxyl functional group). The byproduct, ROH , is alcohol which is removed by volatilization. As soon as reactive hydroxyl functional group is acquired, two partially hydrolyzed molecules link together through a condensation reaction that releases ROH through alcoholysis.

2) Condensation:



As the reaction continues, the amount of $M-O-M$ bounds multiply during such process called polymerization. After the precursor solution is prepared, various techniques can be used to produce the thin films e.g. spin, dip or spray coating. Among these techniques, spin coating has been widely used to deposit thin films onto the smooth substrate. There are many advantages including uniformity, ability to control the film thickness, ability to control the doping concentration, reproducibility, simplicity and low cost. The details as well as the theory behind such coating technique will be described in the next section.

2.3.1 Spin coating

Spin coating is a method for producing the film with thickness in the range of 10 nm - $5 \mu\text{m}$ on the flat substrate. Normally, the substrate that will be coated is held by vacuum chuck. The spin coating process can be broken down onto four stages which are deposition, spin up and spin off that occur sequentially and evaporation stage which takes place throughout the process. Figure 2.5 illustrates the four stages of spin coating process.

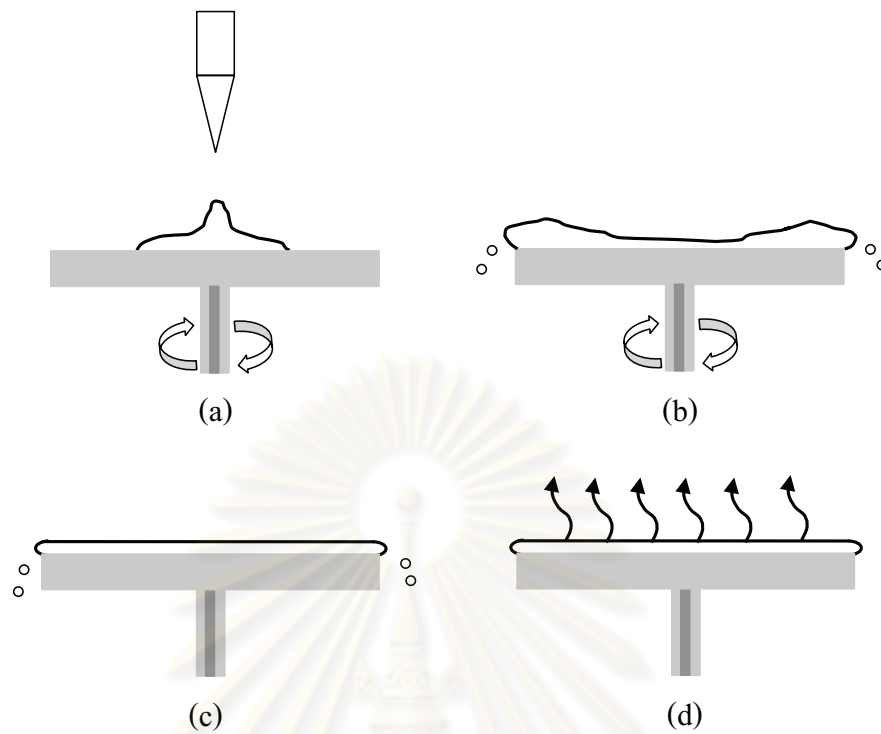


Figure 2.5: The four stages of spin coating process (a) deposition, (b) spin up, (c) spin off and (d) evaporation.

The deposition stage beginning with the excessive amount of liquid is deposited onto the center of a stationary substrate by using a nozzle. The excessive amount of liquid is utility for averting the coating discontinuities due to the fact that the front of liquid will dry before it reaching the wafer substrate edge.

In the spin up and spin off stages, the substrate is accelerated to very high angular velocities ($\sim 300-10000$ rpm). Centrifugal force causes the excess liquid spreading from the substrate leaving thin film. In this stage, the physics behind this coating method is related to equilibrium between the centrifugal force and viscous force which is defined by viscosity of the liquid [103]. In spin coating technique, the thickness of the films can be varied by controlling the spinning speed, time and viscosity of the precursor solution. It has been experimentally observed that the relationship between the film thickness (t) and the spinning speed or

angular velocity (ω) is given below:

$$t \propto \frac{1}{\sqrt{\omega}}. \quad (2.4)$$

The above equation indicates that the higher the spinning speed generates the thinner the film. Beside the spinning speed, the film thickness depends upon the concentration of the precursor solution.

The evaporation stage, in this stage a portion of the excess liquid is volatilized which can be occurred throughly the spin coating process. The defect can take place during spin coating process as the evaporation happens before time, which make a solid skin forming on the surface of solution. This solid skin obstructs the evaporation of solution trapped under this skin generating the coating defect.

2.3.2 Drying

After the gel film is deposited completely, it remains an excess amount of water and many porosities inside the structure. Prior to the pore closed throughout densification process, drying step is necessary to repel the solvent which is held in the pore. Moreover, the elimination of the solvent inside the pore can reduce the stress built up which causes films cracking during densification process.

2.3.3 Sol-gel densification

After drying, the films must be densified by heating to high temperature to form a tight films. When the gel film is heated, it undergoes three stages including heating up, isothermal heating or annealing and cooling down. In heating up and annealing stages, the structure of the films is changed to more denseness producing stresses and strains in gel films due to it constraint on the substrate. In addition, in such stages thermal stress could be generated because of the difference in thermal expansion coefficient between the film and substrate and fluctuation

in temperature. However, it has been observed that the stresses which occur due to the difference in thermal expansion coefficient much smaller than that due to densification [104]. Thus, densification is the main cause producing the stress in the stages of heating up and annealing. The overview of the steps in a sol-gel process including the aim in each of step is given in Table 2.3.

Table 2.3: The major steps in a sol-gel process.

Step	Aim
Preparation of solution	To form gel
Deposition of solution	To produce a wet-gel thin film
Drying	To repel solvent in the gel and prevent cracking
Annealing	To change physical and chemical properties (crystallization and densification)

2.4 Interference conditions in a thin film

Interference phenomena occurs when light waves originate at different positions overlap. If two waves with equal amplitudes and same wavelength are out of phase 180° , the amplitudes cancel and net result is zero. The interference is destructive. If two waves are perfectly in-phase, the amplitude is double. The interference is constructive. In the case of thin film the light wave can interfere with another wave that is reflected from the two different surfaces (air-film, film-substrate). This interference can also cause a decrease or increase in the reflectance or the transmittance of the incident light. Figure 2.6 shows optical model for air/thin film/substrate structure. In this study, the multilayer $\text{SrTiO}_3/\text{BaTiO}_3$ films used to characterize the optical properties were deposited on ITO coated on a glass substrate which is transparency. The thickness of ITO is about 80 nm which is smaller than that of glass substrate with thickness of 1.2 mm. The refractive

index of ITO and glass substrate (n_3) is approximately 2 and 1.47 at wavelength of 450 nm, respectively. The thickness (d) and refractive index (n_2) of the film are about 250 nm and 2.08 at 450 nm, respectively. There are two events occurring as light ray incidents at each interface, reflection and refraction. When incident ray of light SA hits on the film where it is partially reflected and partially refracted at interface between air and thin film (point A). The reflected ray AR_1 of light undergoes 180° phase change or $\lambda/2$ (λ is wavelength of incident ray) due to the higher the refractive index of film compared with the refractive index of air, whereas the part of refracted ray encounters the interface between film and substrate at point B where generates a partial ray transmitted along BT_1 , reflected along BC and then refracted along CR_2 (see Figure 2.6). The refracted ray CR_2 has no phase change since BC is reflected from low denser medium. Interferences can occur both refracted and transmitted ray due to the fact that they originate from same incident ray and acting as coherent ray.

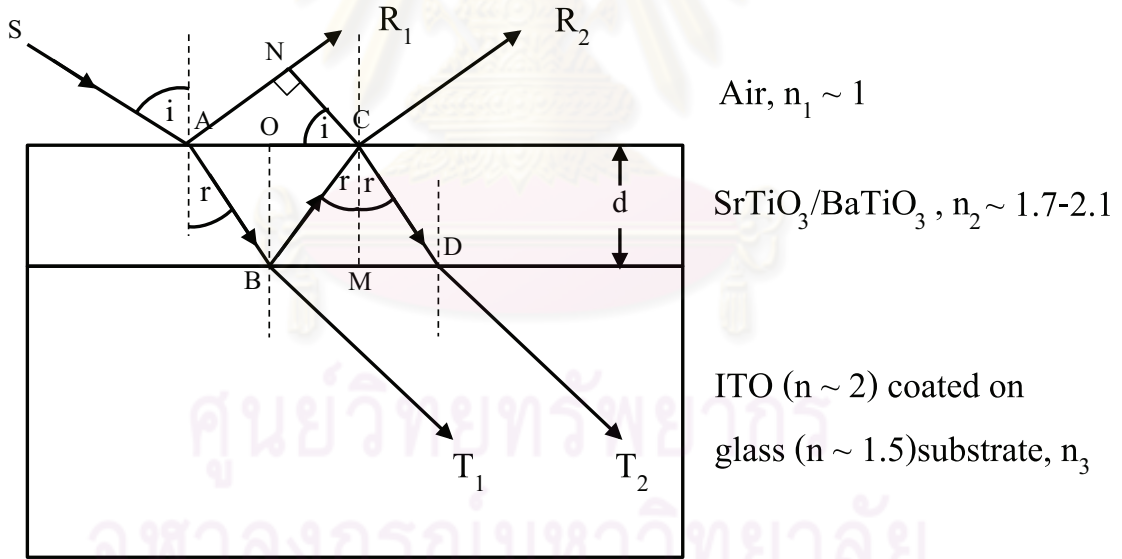


Figure 2.6: Schematic of optical model for air/thin film/substrate structure.

We have considered the case of reflected ray, path difference (Δ) between S-A-N and S-A-B-C- R_2 is given by:

$$\Delta = \text{path ABC in film} - \text{path AN in air}, \quad (2.5)$$

$$\Delta = n_2(AB + BC) - AN. \quad (2.6)$$

Using right angle triangles AOB, COB and ANC as well as Snell's law, the path difference can be expressed as:

$$\Delta = 2n_2d(\cos r). \quad (2.7)$$

Since AR_1 has phase change of 180° making further path difference $\lambda/2$, actually path difference becomes:

$$\Delta = 2n_2d(\cos r) - \frac{\lambda}{2}. \quad (2.8)$$

As the light ray incidents the film surface perpendicularly ($\cos r = 1$), the condition for constructive interference can be written as:

$$2d = \left(m + \frac{1}{2}\right) \frac{\lambda}{n_2}, \quad (2.9)$$

$$2n_2d = \left(m + \frac{1}{2}\right) \lambda, \quad (2.10)$$

and the condition for destructive interference is:

$$2d = (m) \frac{\lambda}{n_2}, \quad (2.11)$$

$$2n_2d = (m) \lambda, \quad (2.12)$$

where $m = 0, 1, 2, \dots$

The interference fringes obtaining from reflectance or transmittance give the information about film thickness as well as optical parameters such as refractive index, extinction coefficient and absorption coefficient. The detail for determination of such optical parameters is given in section 3.4.

2.5 Dielectric properties

2.5.1 Dielectric materials in electric field

Dielectric materials are an electrical insulating substance because of having low the number of free charge carriers. This is due to the fact that these electrons are defined in microscopic region (i.e. atoms or molecules) in the material. Nevertheless, when a direct voltage is applied, there is a very weak current (leakage current) and electrostatic field can be maintained for a long period inducing electrical energy storage in the material. This phenomena can be not found in electrical insulator. The material having dielectric properties is beneficial in capacitor and optoelectronic device. In order to clearly understand what occurs to dielectric material under electric field, an atom is served as an illustration. When an atom is placed in the electric field, positive charge (+q) and negative charge (-q) are separated on molecules making a shift in centers of them as exhibited in Fig. 2.7(a). The separation between centers of positive and negative charge due to an applied external electric field produces forces creating induced electric field (electric field generated by dipole). The electrical dipole moment (\vec{p}) is defined in the term of the product of the charge and the distance of separation between the charges:

$$\vec{p} = q \vec{d} \quad (2.13)$$

where q is total positive charge and \vec{d} is displacement between center of the charges. The density of this dipole build up per unit volume is called the polarization (\vec{P}). Figure 2.7(b) illustrates the electric flux line of dipole (solid line) in applied external electric field (dash line). The total electric field is the outcome of the induced electric field and the applied electric field, that is the electric field generated by dipole is very slight compared with external electric field.

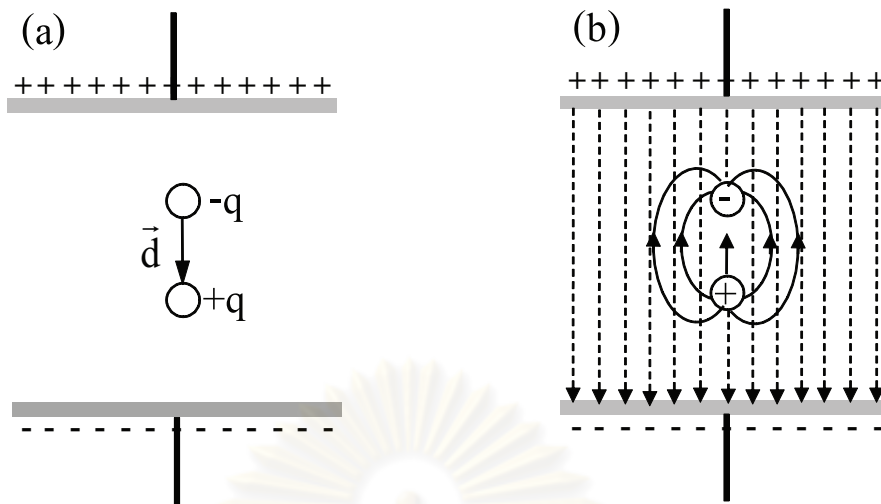


Figure 2.7: (a) Displacement of center of positive and negative charge due to an applied external electric field. (b) Electric flux line of dipole (solid line) and applied external electric flux line (dash line).

2.5.2 Dielectric constant

According to Gauss's law in matter, each free charge (ρ_{free}) produces dielectric displacement (\vec{D}):

$$\vec{\nabla} \cdot \vec{D} = \rho_{free} \quad (2.14)$$

where \vec{D} is defined as:

$$\vec{D} = \epsilon_0 \vec{E} + \vec{P}. \quad (2.15)$$

The constant ϵ_0 is called the permittivity of free space which has the value of $8.85 \times 10^{-12} \text{ C}^2/\text{N}\cdot\text{m}^2$. The dielectric displacement is described in two terms, $\epsilon_0 \vec{E}$ refers to the electric field related in free space and another one, \vec{P} represents the electric polarization in the matter.

As mention earlier, electric field induces polarization pointing in the same direction with the electric field. In isotropic medium, or homogeneous medium,

the polarization is directly relative to the electric field as follow:

$$\vec{P} = \epsilon_0 \chi_e \vec{E} \quad (2.16)$$

where χ_e is the electric susceptibility. This value refers to the ability of matter to polarize due to electric field depending on the structure of material and external factors such as temperature, frequency and pressure [105].

Thus, electric displacement becomes:

$$\vec{D} = \epsilon_0 \vec{E} + \epsilon_0 \chi_e \vec{E} = \epsilon_0 (1 + \chi_e) \vec{E} = \epsilon \vec{E} \quad (2.17)$$

here, the constant ϵ is the permittivity of the matter. The dielectric constant (ϵ_r) is defined in term of the relation of the permittivity of the matter to that of free space:

$$\epsilon_r = \frac{\epsilon}{\epsilon_0} = 1 + \chi_e. \quad (2.18)$$

The dielectric constant is also called relative permittivity. Because of having polarization, a dielectric material is used as capacitor, an electrical device be capable of storage charge from current by placing the dielectric between two conducting plates. A schematic of parallel-plate capacitor is illustrated in Fig. 2.8. When the

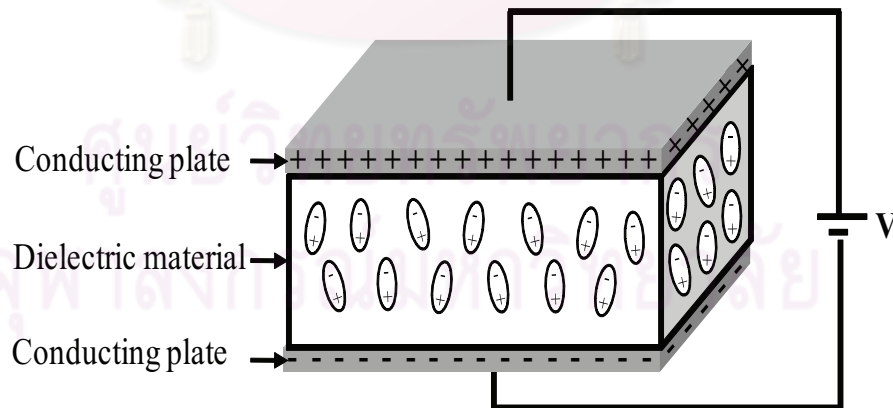


Figure 2.8: A parallel-plate capacitor inserting with dielectric material.

voltage (V) is applied across the conducting plates, the dielectric material polarizes yield the charge (Q) which can be stored in the capacitor. The capacitance

(C) of capacitor is given the meaning as the property that can allow the charge stored when the voltage is applied. The relationships between capacitance, charge and voltage are:

$$C = \frac{Q}{V}. \quad (2.19)$$

For parallel-plate capacitor, the capacitance is defined by

$$C = \epsilon \frac{A}{d} = \epsilon_r \epsilon_o \frac{A}{d} \quad (2.20)$$

here, A is the area of each conducting plate and d is distance between the insulated plates which is equal to the thickness of dielectric. From equation 2.20, the capacitance is directly proportional to the dielectric constant and depends upon the shape of the plates as well as the gap between them. In this thesis work, the films were fabricated as interdigitated capacitors. The configuration of interdigitated electrode is shown in section 4.7.1. In addition, dielectric constant which relates to polarization relies on frequency of external field. Generally, the total polarization of dielectric material is sum of four components as depicted in Fig. 2.9.

The four contributions of polarization compose of:

1. Electronic polarization: when the external electric field is applied to dielectric materials, the displacement of electron clouds around the nucleus occurs.
2. Ionic polarization: in this case positive and negative ions in crystal are separated from their equilibrium positions.
3. Dipolar polarization: this polarization is found only in materials having permanent dipole moment such as water. The electric field makes electric dipoles rotating in direction of the field.
4. Space charge polarization: this polarization is due to accumulation of charge developing at interface such as grain boundaries within the materials.

Each source of polarizations does not response to electric field at all frequencies. Figure 2.10 illustrates frequency dependence of various polarizations. At a

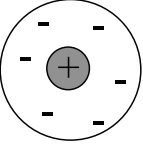
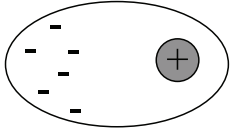
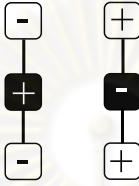
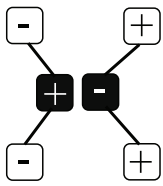
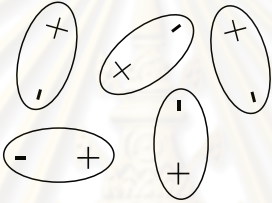
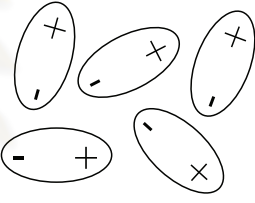
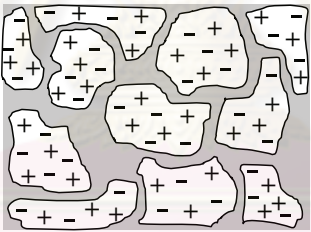
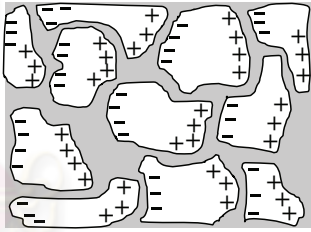
Polarization mechanism	Unpolarized state ($E = 0$)	Polarized state ($E \neq 0 \rightarrow$)
Electronic		
Ionic		
Dipolar		
Space charge		

Figure 2.9: Schematic of various polarization mechanisms.

very low frequency range (less than 10^2 Hz), all the four polarizations respond to applied electric field. As the frequency of electric field increases from 10^2 - 10^8 Hz (radio frequency), space charge polarization is unable to follow the field. At the frequency range 10^8 - 10^{12} Hz (microwave frequency), both dipolar and electronic polarization can occur. For this reason, microwave frequency is utilized generating heat to warm food because it operates at the relaxation frequency of molecules of water. At high frequency beyond 10^{14} Hz, there is only electronic polarization. This is due to an electron having small mass. In other words, it has tiny inertial

resulting in only free electron responded to electric field at high frequency or short time taken to change in the field.

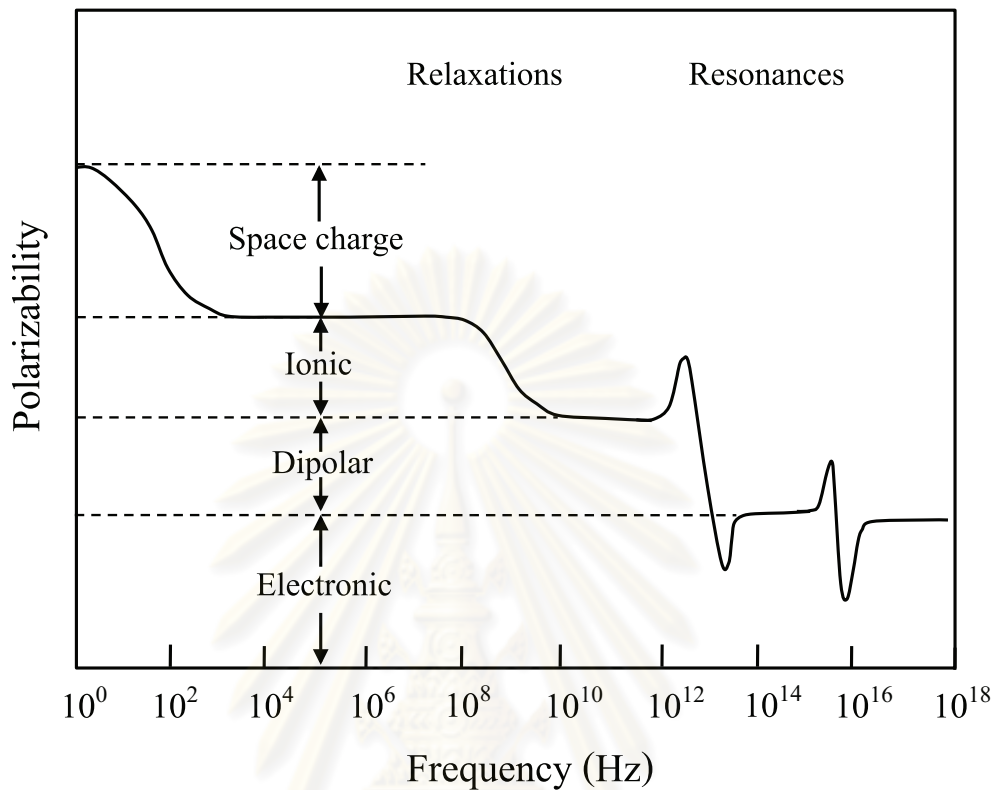


Figure 2.10: Frequency dependence of polarizability.

From electromagnetic theory, it was known that the dielectric constant (ϵ_r) in high frequency range is related to refractive index (n) and relative permeability (μ_r) according to Maxwell's equations following the expression [106]:

$$n = \sqrt{\epsilon_r \mu_r} \quad (2.21)$$

As $\mu_r = 1$ for nonmagnetic substance, the equation 2.21 becomes:

$$n = \sqrt{\epsilon_r} \quad (2.22)$$

Refractive index values are measured at a standard optical frequency, normally at visible light range which is hundreds of THz. From equation 2.22, if the dielectric constant was measured in optical frequency range, it would be in the range of 2.89-4.41.

In this section, the dielectric constant of the films was determined by converting the capacitance obtained from a commercial LF impedance analyzer. The dielectric measurement was carried out in the radio frequency range, which the frequency used in this work is in the range of 10-1000 kHz. We noted that the obtained dielectric constant which is converted from the capacitance values in the radio frequency range can not be compared to that the obtained values from refractive index which is in the optical frequency range. This is how the discrepancy comes from.

2.5.3 Dielectric loss

As a.c. voltage is applied to a perfect insulator (air is between two conducting plates), the current leads the voltage by a phase angle 90° as presented in Fig. 2.11(a) resulted in no consumption of energy (power consumption, $P = IV(\cos 90^\circ) = 0$). Nevertheless, if the plate of capacitor is filled with dielectric material, the current does not lead the applied voltage precisely 90° but leads by $(90-\delta)^\circ$ as shown in Fig. 2.11(b). The total current vector, it has both parts of real and imaginary. The loss current, I_L is the in-phase component of current whereas the charging current, I_C is the out of phase current component.

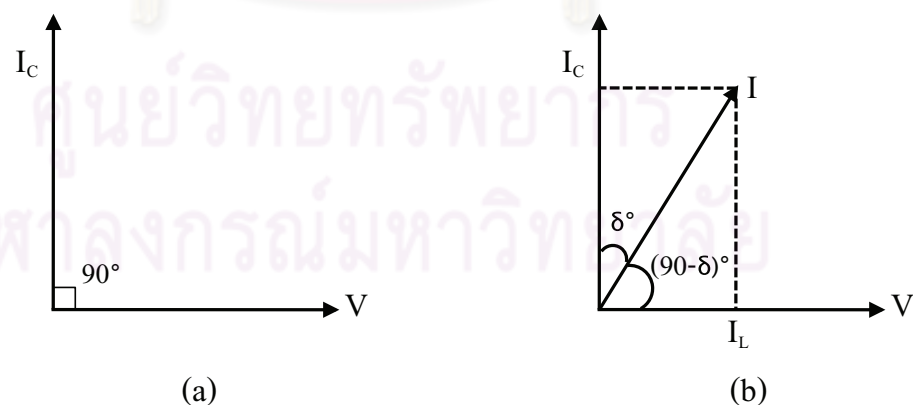


Figure 2.11: Phasor diagram of (a) an air capacitor and (b) capacitor filled with dielectric.

Since the current does not lead the voltage exactly 90° , there is a consumption of a certain amount of energy for which is absorbed by the electric material and dispersed in the form of heat. Such dissipation of energy is so called dielectric loss. Thus, the dielectric loss is an important parameter that indicates the quality of the dielectric material. The dielectric constant in alternating field is written as a complex function:

$$\varepsilon_r^* = \varepsilon_r' + i\varepsilon_r'' \quad (2.23)$$

where the value of ε_r' defines out of phase current (I_C) component whereas the value of ε_r'' determines in-phase current (I_L) component. Quantitative dissipation of energy is described in the term of loss tangent or loss factor ($\tan\delta$) which is defined as a relative magnitude of ε_r'' with respect to ε_r' :

$$\tan\delta = \frac{\varepsilon_r''}{\varepsilon_r'}. \quad (2.24)$$

For this purpose, the material with both high dielectric constant and low value of dielectric loss is demanded for fabricating capacitor in the smallest physical space.

2.6 Gas sensor

Gas sensor is a device which transforms the chemical information to electrical signal. It comprises of two main parts including receptor and transducer functions (see Fig. 2.12). The receptor has a function to recognize the gas molecules. In this part is based on the reaction, i.e. adsorption or electrochemical reaction, between the gas molecules and receptor. Such interaction could be exhibited in the form of physical and chemical effects on receptor like for example change in surface or bulk properties or work function. For another part, transducer has an obligation to convert the effects taken place in the former section into electrical signal such as resistance. For semiconductor gas sensor, the change in work function due

to having oxide surface plays a role as receptor function and the change in its resistance is output signal [27].

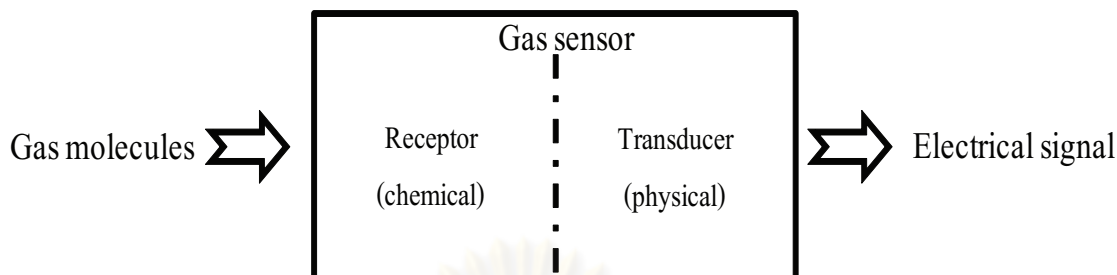


Figure 2.12: Schematic of basic structure of gas sensor having reactor and transducer.

2.6.1 Mechanism of gas sensor

The electrical output signal of semiconducting oxide gas sensor is displayed by means of variation of the resistance when it exposes to two given gas species, one is target gas which is usually compared with purify air. The changes in resistance may be increasing or decreasing depending on the kind of sensor materials (n-type or p-type semiconductor) and the type of gases (reducing or oxidizing gas). Here, we will give you an example of increasing in resistance of a p-type semiconductor. Figure 2.13 shows typical transient signal of a sensor made from p-type semiconductor under reducing gas atmosphere as a function of time. The response time is defined as the time that it takes sensor signal to reach 90% of its steady state [107]. The recovery time is the time taking the sensor to be within 10% of the initial value (before exposure to the target gas). Regularly, the response time is much shorter than recovery time. The Δ in Fig. 2.13 represents the difference between initial value and the value taking the sensor to reach steady state.

In order to understand the basic of sensing mechanism and how the sensor can covert the chemical information into electrical resistance, the energy band diagram of semiconductor needs to be mentioned. In this work, however, the gold was deposited onto our film surface as to be electrode, a metal-semiconductor

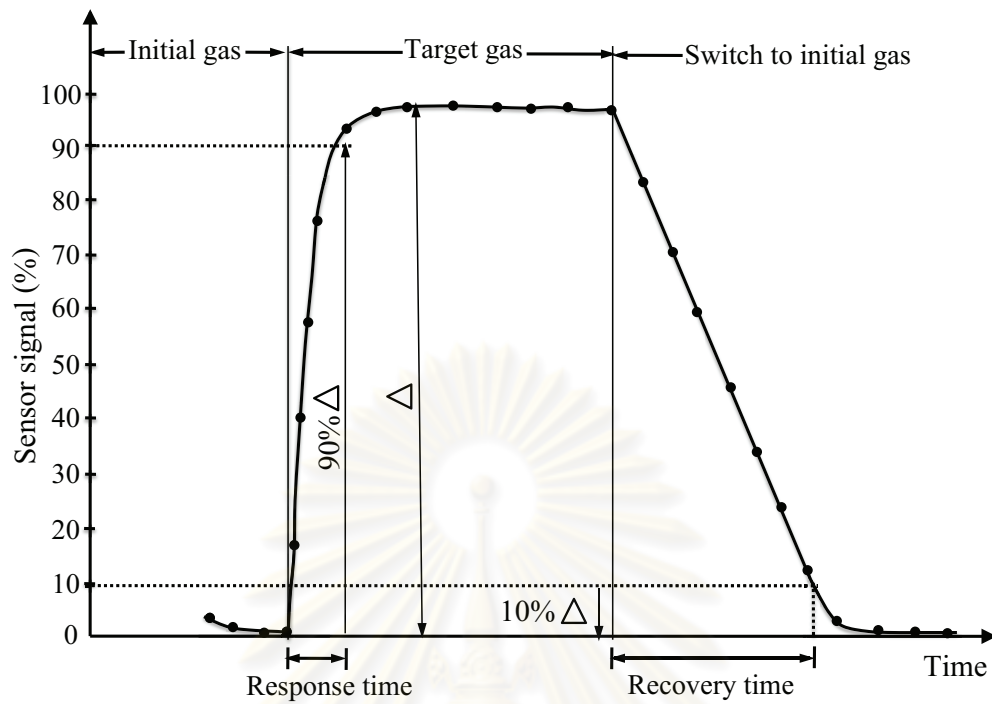


Figure 2.13: Typical transient signal of a sensor as a function of time.

contact, called Schottky junction, can occur. The schematic diagrams of the band structure of metal and p-type semiconductor junction before and after contact are depicted in Fig. 2.14(a) and 2.14(b), respectively.

ศูนย์วิทยทรัพยากร
จุฬาลงกรณ์มหาวิทยาลัย

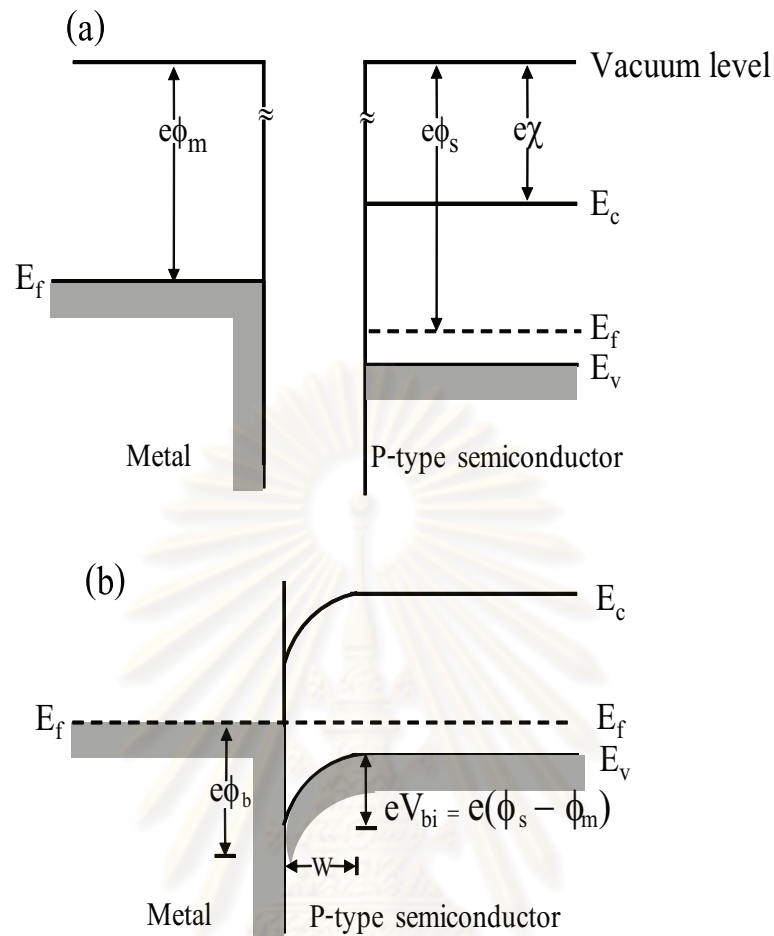
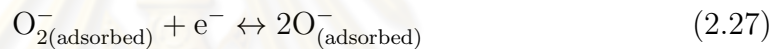
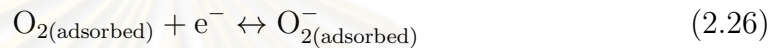


Figure 2.14: Energy band diagram of a metal-p-type semiconductor junction for $\phi_s > \phi_m$ (a) before and (b) after contact.

Before making contact, the Fermi level (E_f) in metal is higher than that in p-type semiconductor. The parameters ϕ_m and ϕ_s are the work function of metal and semiconductor compared with vacuum level, respectively. χ is called the electron affinity of semiconductor. After contact, according to equilibrium principle of the Fermi level equalization across interface, the flow of electrons from metal into the lower energy state in a p-type semiconductor happens making the accumulation of electrons in a semiconductor near the junction. This result produces depletion layer or space charge layer (W) along with the potential barrier having a height of $eV_{bi} = e(\phi_s - \phi_m)$ due to downward band bending. This barrier impedes the electron movement from the semiconductor into the metal. Reversely, potential

barrier with height of $e\phi_b = e(\phi_m - \chi)$, also known as Schottky barrier, prevents the electron transfer from the metal into the semiconductor. The gas sensing properties are based on the interaction between gas molecule and sensor surface. When the sensor is heated under air atmosphere, the oxygen acts as trap sites which captures electrons from the film surface to form in three species including O_2^- , O^- and O^{2-} as described in equation (2.26)-(2.28) [108, 109, 110].



Usually, O_2^- is formed at temperature of 100 °C whereas O^- and O^{2-} can be generated at higher temperature about 400 °C [30]. Owing to the removal of such electrons from the surface, the density of the electrons near the film surface decreases resulting in the reduction in the potential barrier. Hence, the sensor resistance falls under air atmosphere. Here, ethanol (C_2H_5OH) which is a reducing gas was used as testing gas. It acts as electron donating species, reacting with the oxygen anions and thereby releasing electrons to the p-type semiconductor. This results in increase in potential barrier again yield the resistance of the sensor ups under ethanol atmosphere. Figure 2.15 illustrates the concept of potential barrier in p-type semiconducting oxide gas sensor at the film surface in a reducing gas atmosphere.

At high operating temperatures, the adsorbed ethanol molecules can be decomposed into ethylene vapor (C_2H_4) and water vapor ($H_2O_{(vapor)}$) (see equation

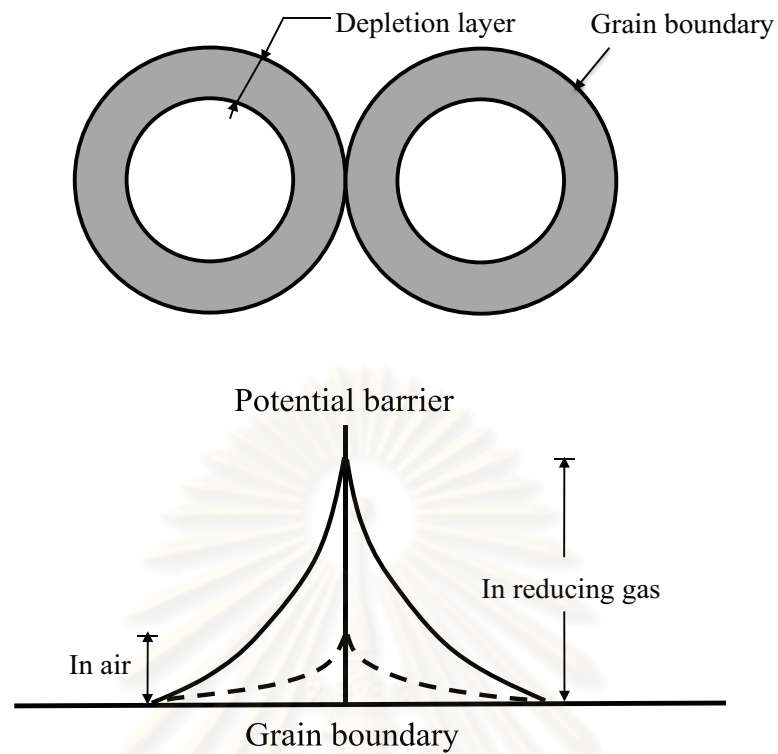
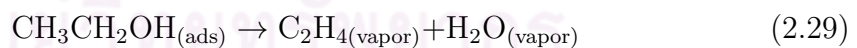


Figure 2.15: Schematic of potential barrier of gas sensor at a grain boundary.

2.29), or can also be composed to acetaldehyde ($\text{CH}_3\text{CHO}_{(\text{adsorbed})}$) and water vapor ($\text{H}_2\text{O}_{(\text{vapor})}$) as described in equation 2.30. Then acetaldehyde can become a vapor of acetic acid ($\text{CH}_3\text{COOH}_{(\text{vapor})}$) which later on desorbed from the sensor surface illustrating in equation 2.31.



As discussed above, the immediately change in resistance of the sensor occurs when it reveals gases. A quantitative definition of the change to evaluate the sensor performance is given in the term of sensor sensitivity. Sensitivity (S_r) of sensor is defined by the rate of the resistance changes when it contacts with a target gas compared with the resistance that it presents in a reference gas as the following:

$$S_r = \frac{R_{\text{gas}}}{R_{\text{air}}} \quad (2.32)$$

for p-type semiconductor gas sensor presented in a reducing gas such as ethanol ($\text{C}_2\text{H}_5\text{OH}$), carbon dioxide (CO_2) and carbon monoxide (CO), and for n-type semiconductor gas sensor exposed to a oxidizing gas such as nitrogen dioxide (NO_2) and ammonia (NH_3). In case of p-type semiconductor gas sensor presenting in an oxidizing gas, the sensor sensitivity is defined as:

$$S_r = \frac{R_{\text{air}}}{R_{\text{gas}}} \quad (2.33)$$

where R_{gas} and R_{air} are the sensor resistance exposed to gases and air, respectively. Equation 2.33 can be used in the case of n-type semiconductor gas sensor presenting in a reducing gas. In any case, the sensitivity values reported in literatures are positive numbers.

2.6.2 The influence of microstructure and grain size of film

From earlier discussion, the gas sensing properties are grounded on chemical interaction which occurs on the surface. Such interaction is affected by many parameters including internal and external causes. The crystallite size, agglomeration, area of inter-grain as well as porosity are internal factors or geometric parameters. Whereas physical-chemical parameters such as chemical and phase composition, physical properties of additives and effect of uncontrolled impurities are classified as external factor of gas sensing properties [111]. It was empirically found that the geometric factors have an enormous impact on gas sensing characteristics [112, 113]. This is due to two reasons, one is microstructure dominating

on distribution of absorption area and another is that the microstructure has an influence on the mobility of free charge carriers. It has been observed that the resistance of a sensor links to many components including the resistance of contact between grain and electrode (R_c), grain boundary contact (R_g), inter-agglomerate contact (R_{agl}) and bulk resistance (R_b) which can be schematically depicted in Fig. 2.16.

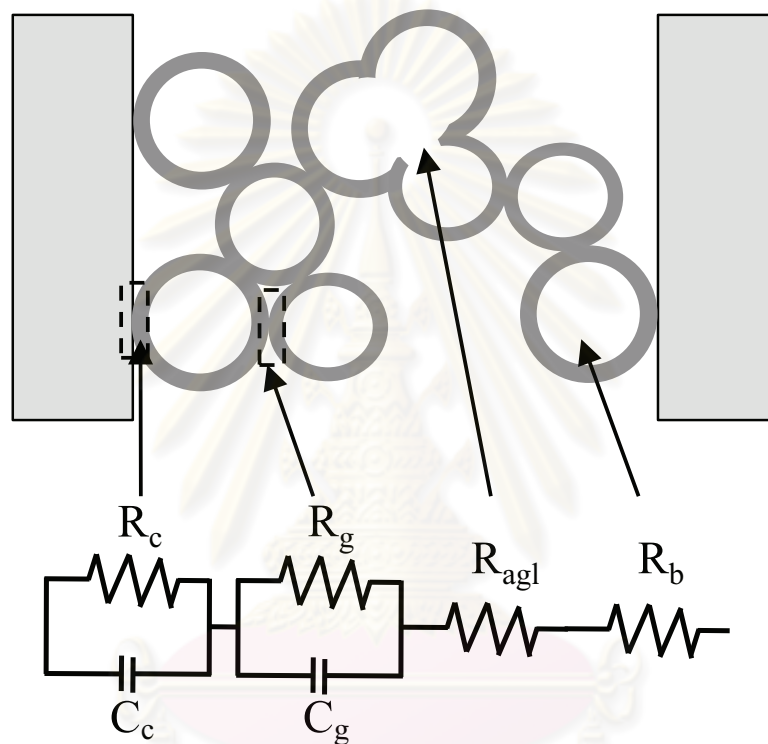


Figure 2.16: Schematic of agglomerated polycrystalline films showing contribution of different components of resistances.

However, among of these contributions, grain boundary contact is most dominant. From experimental observation, gas sensitivity is associated with the relationship between grain size (D) and width of depletion layer (W) which can be divided into three cases describing below and a model narrates the effect of grain size on gas sensitivity as illustrated in Fig. 2.17 [13, 114, 115].

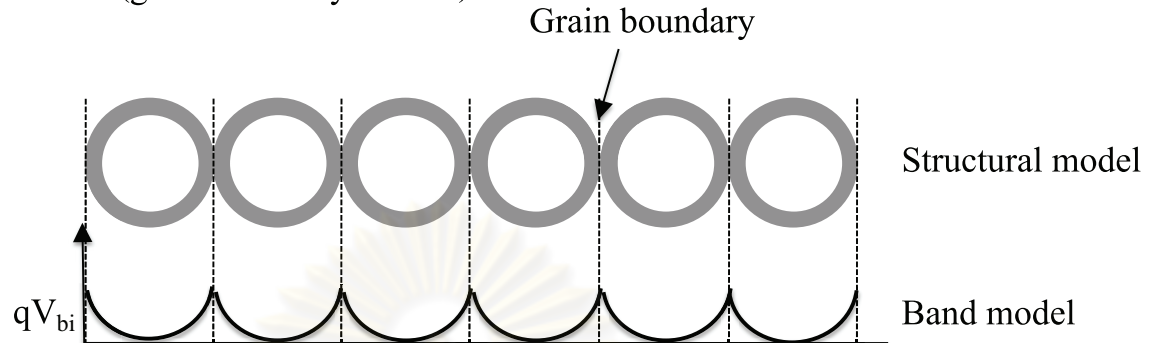
1. $D \gg 2W$: When grain size is far larger than the depletion width, the grain

boundary contacts are most resistant to charge transport through grain boundary (GB) barrier from one grain to another (see Fig. 2.17(a)). Therefore, in this case the GB barrier is considerable to govern the gas sensing mechanism (grain boundary control). As GB barrier does not depend on the grain size, the gas sensitivity is independent of grain size for the sample with larger grain size.

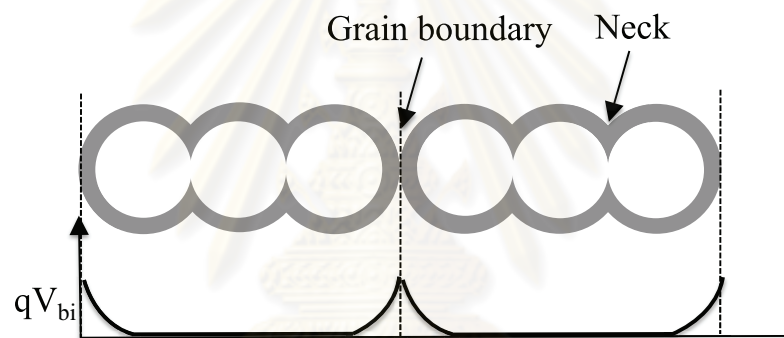
2. $D \geq 2W$: As D approaches $2W$, grain size reduces leading to increase in depletion width, consequently, the depletion layer which encloses each neck forms a constricted conduction channel within each of grain (see Fig. 2.17(b)). In this case necks become the most resistant controlling conductivity of sensor (neck control). Here, the gas sensitivity is improved compared with in first case ($D \gg 2W$) with decreasing grain size.

3. $D < 2W$: In this case the depletion layer extends across the complete grain. The bulk of the crystallites is entirely depleted of charge carriers (see Fig. 2.17(c)). The energy band is quite smooth through entire inter-grain structure. The electrical resistance of grain presides entire resistance of the chain, thus in this case the conductivity is dominated by grains themselves (grain control). It has been experimentally observed that the highest gas sensitivity could be obtained for the sample with this case.

(a) $D \gg 2W$ (grain boundary control)



(b) $D \geq 2W$ (neck control)



(c) $D < 2W$ (grain control)

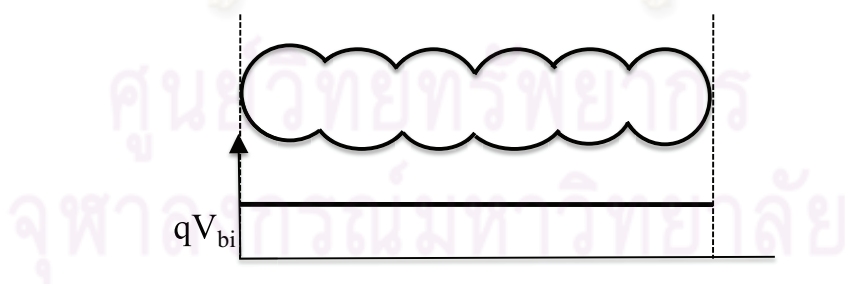


Figure 2.17: Schematic model for grain size effect. Shaded area represents to depletion region (high resistance) whereas unshaded area refers to core region (low resistance).

CHAPTER III

CHARACTERIZATION TECHNIQUES

In this chapter, the techniques employed to characterize films are briefly mentioned. X-ray diffractometry (XRD) was used to examine the crystallinity, the crystal structure as well as crystalline size of the films. Field emission scanning electron microscope (FESEM) and atomic force microscope (AFM) used to investigate the surface morphology, cross-section and grain size will be described. The chemical composition of the films was obtained by using energy dispersive X-ray spectroscopy (EDS). X-ray absorption spectroscopy (XAS) was utilized to verify the oxidation state of Fe in the BaTiO₃ and SrTiO₃ films. Moreover, optical properties as well as determination of optical parameters such as energy gap and refractive index of the films were characterized using the spectra obtained from ultraviolet-visible (UV-Vis) spectroscopy.

3.1 X-ray diffraction

X-ray diffractometry (XRD) is a technique used to characterize structural properties of the materials such as orientation, strain, stresses and defect structure. The apparent advantage in this technique beyond other techniques is that XRD can investigate the defect structure and crystalline phase without destructing the sample. Moreover, high resolution XRD can be used to determine film thickness for such perfect epitaxy films.

3.1.1 X-ray production

X-rays used in diffraction technique are produced when high energy electron collides with a metal target which is in an X-ray vacuum tube. There are various interactions which can occur as presented in Fig. 3.1. As incident ener-

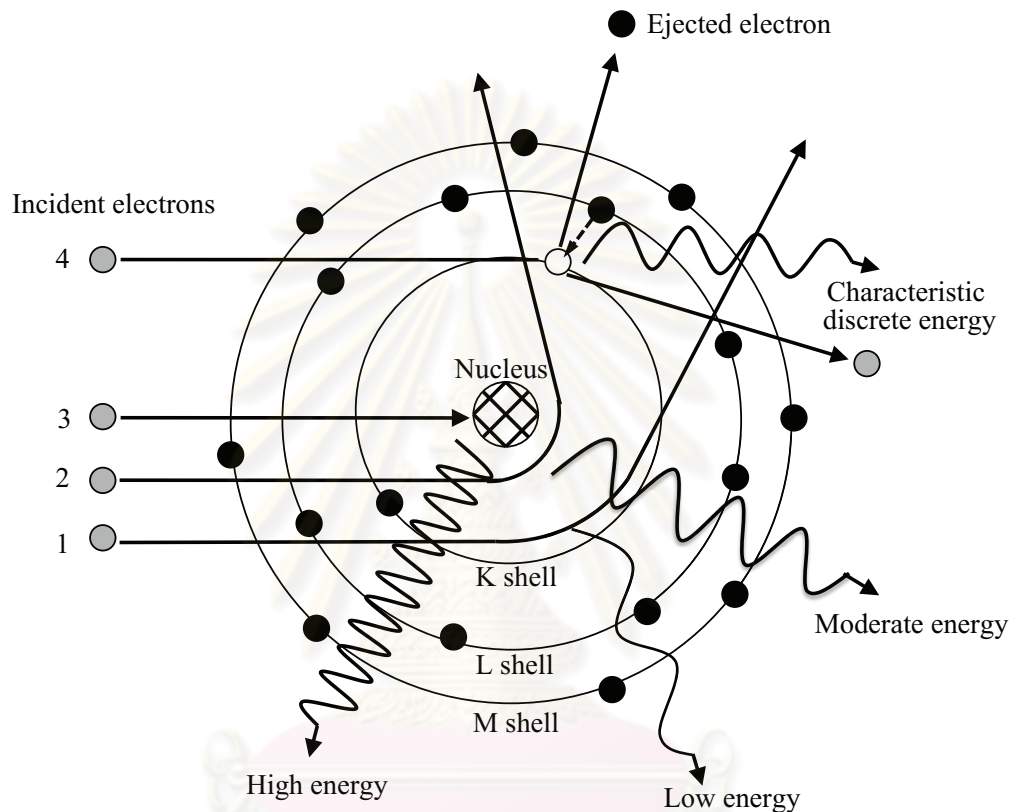


Figure 3.1: Schematic showing probability of X-ray production.

getic electrons interact with coulomb field of the nucleus of the target atom resulting in their energies immediately decelerated yield their energies are changed to the energy of X-ray photon (see event 1, 2 and 3). These X-rays are called brehmsstrahlung. The electron interacts with the nucleus generating maximum X-ray energy and its energy decreases as distance of glancing blow increases. This results in brehmsstrahlung radiation producing over all energies. The intensity of brehmsstrahlung radiation which is outcome from the bombarding electrons interacted with the nuclei in the target material depends on various parameters such as mass and charge of electron and nucleus of the target as well as the energy of the

bombarding electrons [116]. If the incident electron has sufficient energy which is greater than binding energy of the innermost shell, called the K shell, it can knock an atomic electron out of innermost shell of the target atom (see event 4). Then, electron from outer shell fills in the vacant shell emitting characteristic X-ray of which the energy is the difference between binding energies of the two shell. The bombarding and the ejected electron will then interact further with other target atoms. Mostly, there are distinguished two series of X-ray transition, K and L series lines. The spectra lines resulting from transition of electron from outer shell onto K and L shell are called K and L series lines, respectively. In addition, there are several lines in the K and L set, but only the two strongest intensities are often used in diffraction work, K_α and K_β which are considered that the transition from L and M shell to K shell, respectively. Figure 3.2 depicts the schematic of part of X-ray spectra including two main parts which are continuous and characteristic radiation.

3.1.2 Bragg's Law

Crystals consist of lattice planes of atom which is separated by a distance of d , each family of planes has a different d -spacing from one another. The Miller indices (hkl) are utility for describing the orientation of these planes with respect to the a , b , and c crystallographic axes in a unit cell. Therefore, the spacing, d_{hkl} , between planes related to the lattice geometry can be written as follow:

$$\frac{1}{d_{hkl}^2} = \frac{h^2}{a^2} + \frac{k^2}{b^2} + \frac{l^2}{c^2}. \quad (3.1)$$

For a simple cubic ($a=b=c$), the equation 3.1 can be simplified as:

$$\frac{1}{d_{hkl}^2} = \frac{h^2 + k^2 + l^2}{a^2} \quad (3.2)$$

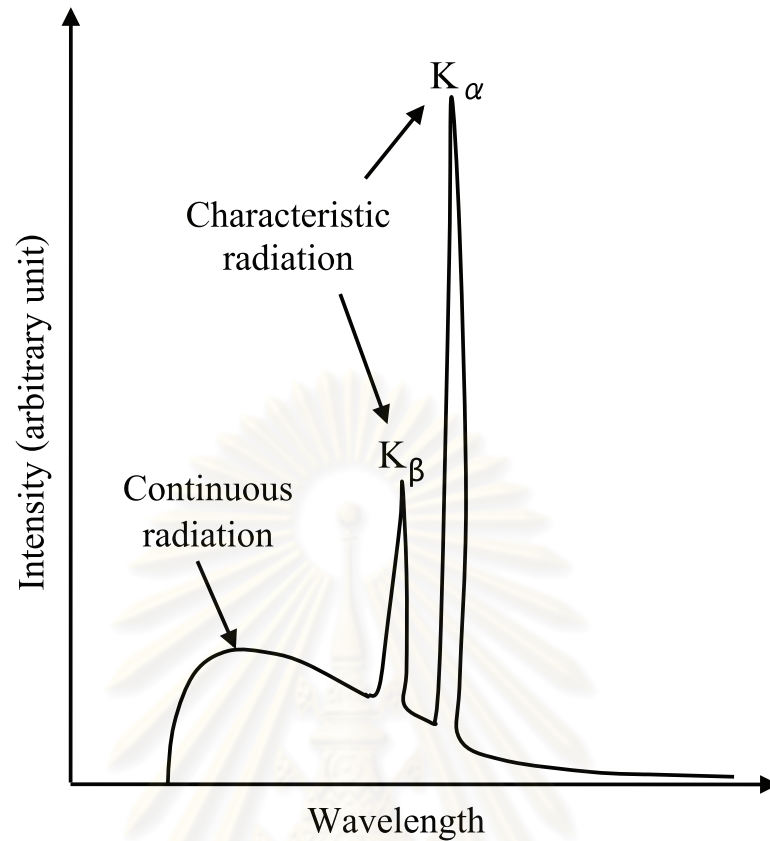


Figure 3.2: Schematic of X-ray spectra includes brehmsstrahlung and K_{α} and K_{β} characteristic radiation.

and the equation below for the crystal with tetragonal structure ($a=b$):

$$\frac{1}{d_{hkl}^2} = \frac{h^2 + k^2}{a^2} + \frac{l^2}{c^2}. \quad (3.3)$$

The incident X-ray beam acts as the probe which hits on a crystal, X-ray diffraction occurs due to fact that X-ray wavelength is comparable to the atomic planes. However, there is a certain condition that diffraction from atomic planes of the crystal will only acquire rise to constructive interference, producing diffracted beam which is detected by a detector. Bragg's law gives the condition for which diffraction peak can be observed from constructive interference happening when the path difference between radiation scattered from adjacent planes is equal to a whole number of X-ray wavelengths. The Bragg's law can be expressed as:

$$2d_{hkl} \sin \theta = n\lambda \quad (3.4)$$

where θ represents the angle between the planes and the incident and diffracted X-ray beam. λ refers to X-ray wavelength.

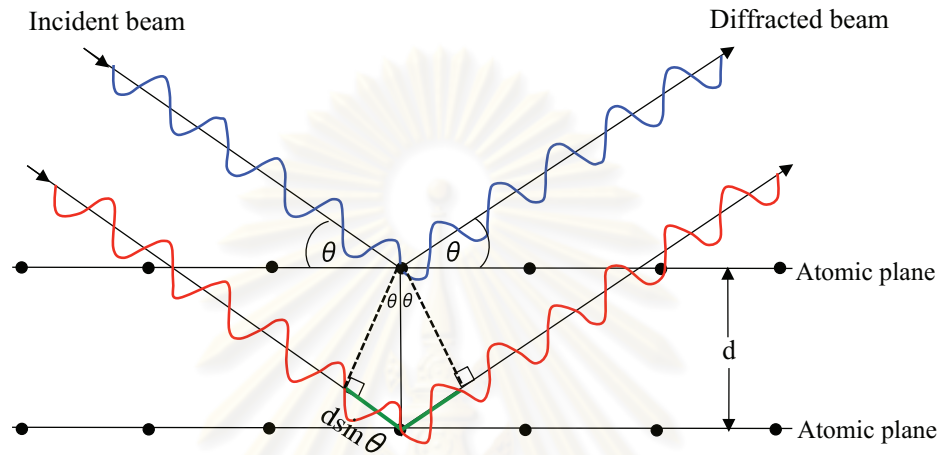


Figure 3.3: Schematic representation of X-ray diffraction from crystal structure according to Bragg's law.

In X-ray diffraction, the position of the scattering matter within the crystal is electron densities, $\rho(\vec{r})$, generating a characteristic diffraction pattern which is obtained from the Fourier Transform of the electron density. The observed intensity, $I(\vec{s})$, is directly proportional to the square of absolute value of structure factor, $F(\vec{s})$, as given below:

$$I(\vec{s}) \propto |F(\vec{s})|^2 \quad (3.5)$$

For each diffraction maximum intensity, the structure factor can be obtained from the electron density according to

$$F(\vec{s}) = \int \rho(\vec{r}) e^{(2\pi i \vec{s} \cdot \vec{r})} d\vec{r} \quad (3.6)$$

where \vec{r} is a vector in the direct space unit cell.

In this work, the crystal structure and crystallite size of all films were characterized by XRD (Model D8 Bruker diffractometer) using $\text{CuK}_{\alpha 1}$ with the wavelength of 1.5406 Å. Continuous scan was taken from 20° to 80° in 2θ scan mode at scan speed of 0.5 sec/step and increment rate of 0.02 degree/step operating at room temperature. The signal was monitored by VÅNTEC-1 detector (Super speed detector). In order to estimate the crystallite size of the films, the well known Scherrer's formula as shown in equation 3.7 [116] was utilized by measuring the full width at half maximum (FWHM) of XRD peak:

$$t = \frac{k\lambda}{B\cos\theta_B}, \quad (3.7)$$

where t is the average crystallite size. λ is wavelength of X-ray and B represents a width measured in radians at an intensity equal to half of the maximum intensity, θ_B is the Bragg angle and k is the shape factor of the average crystallite ($k=0.94$).

3.2 Field emission scanning electron microscopy

Field emission scanning electron microscope (FESEM) is a type of electron microscope which is adapted from conventional scanning electron microscope (SEM) but in FESEM system the electron gun is a field emission (FE) electron gun which is a smallest scanning probe having high potential more than conventional electron gun using tungsten hairpin filament. In other words, FE electron gun can produce the brightness about 1000 times higher than that in SEM. The brightness is a significant factor to obtain the high resolution because the higher brightness, the higher current density, produces smaller beam spot size leading to improve in the depth and higher resolution as well as magnification. Figure 3.4 depicts schematic of basic element of FESEM system. Usually, an extremely fine single crystal tungsten rod tip (100 nm diameter) is used as FE tip. A very high electron field is generated between the tip and the first anode within high vacuum column. The electrons are drawn from the tip without filament heating. The potential

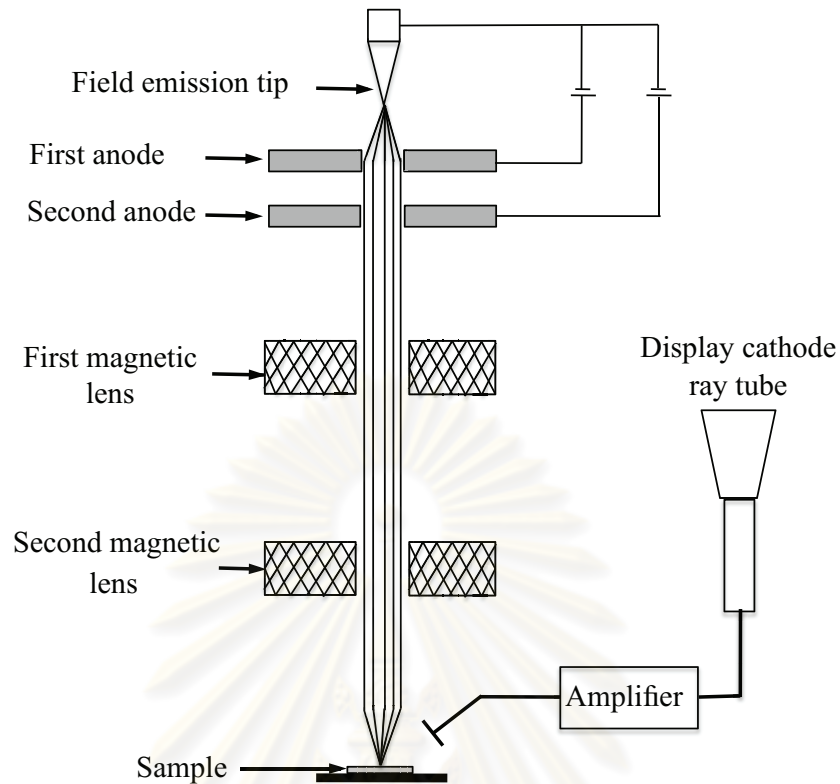


Figure 3.4: Schematic of basic fundamental element of FESEM.

difference between the second anode and the tip accelerates the electrons towards the anode plate and down the column, in the same way as in a conventional SEM. The several magnetic lenses are utility to focus and scan electron beam on sample surface. When the energetic electrons, so called primary electrons, encounter the sample, the interactions between electron and sample happen producing several signals such as backscattered electron, auger electron, characteristic X-ray, continuous X-ray and secondary electron etc. The volume that holds such interactions occurring due to the penetration of electron into the sample is called excitation volume. The size of excitation volume directly depends on energy of electron beam and inversely depends on atomic number (Z) of the specimen. Figure 3.5 shows the interaction of primary electron beam on the surface of sample, presenting the excitation volume for different emission signals. Since the secondary electrons are produced closing to the sample surface (a depth of 5-50 nm) [117], they are suitable for observing the morphology of specimen. Intensity of these emitted electrons is

detected to resolve an image on a cathode ray tube or computer monitor. The higher signal intensity creates a brighter image.

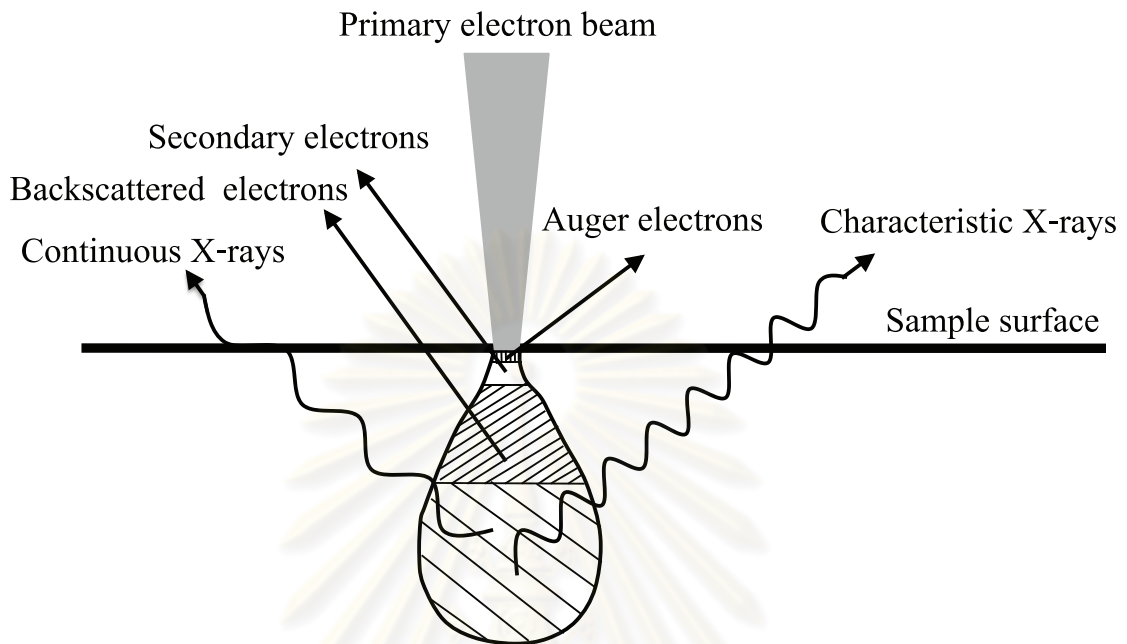


Figure 3.5: The interaction between primary electron beam on sample surface showing the excitation volume produced auger electrons, secondary electrons, backscattered electrons, characteristic X-rays and continuous X-rays with their depths within the sample.

As mentioned above, besides, backscattered electron, auger electron and secondary electron emit during interactions, there is also characteristic X-rays of which the energy corresponds to the difference in energy between the uniquely defined levels of the atom. The production of X-ray is discussed earlier in section 3.1.1. From this reason, it is possible to quantify the element by measuring the energy of the X-ray, which such technique is called energy dispersive X-ray spectroscopy (EDX or EDS). Typically, the EDX detector is integrated into FESEM instrument. The EDX detects energy distribution of emitted electron in counts per second by mean of intensity. This intensity can be converted to atomic percent. Thus, the chemical composition of each element in the sample can be obtained from the area under the peaks.

In this thesis work, surface morphology, cross-section and chemical composition of the films were characterized by using FESEM model HITASHI S-4700 operating at a voltage of 50 kV. Since the sample is not electrically conducted, gold coating and carbon tape were used to avoid electrical charging during analysis.

3.3 X-ray absorption spectroscopy

X-ray absorption spectroscopy (XAS) is the measurement of the X-ray absorption across section of a material as a function of X-ray energy. The absorption spectra provide information about electronic and atomic structure surrounding a probed element. In my thesis work, the probed element is iron (Fe) which was used as a doping element in SrTiO₃ and BaTiO₃ films. The advantages of this technique include the fact that it can be applied to not only solid sample which is regardless crystallinity but also to liquid and gas sample. XAS is mostly taken with a synchrotron radiation because synchrotron generates a extensively range of electromagnetic radiation with high intensity. Synchrotron is a cyclic particle accelerators with particles such as electrons, protons or ionized atoms (usually, being electrons). When electrons are accelerated moving along a curved path to near speed of light, they emit electromagnetic waves in the region of infrared to extremely high energy X-ray at parts tangential to the arc that they travel. XAS is relevant to the photoelectric effect. When energy of photon is absorbed by core electron in the atom of interest, the electron is excited to continuum state (see Fig. 3.6(a)) in the form of photoelectron with energy as expressed in equation 3.8.

$$E_k = \frac{hc}{\lambda} - E_0 \quad (3.8)$$

where E_k is the kinetic energy of photoelectron, E_0 is the binding energy or edge energy of core electron. Term of hc/λ refers to energy of photon. The process can occur only if the energy of photon is greater than the binding energy of electron. When core electron leaves its shell creating hole, the electron from

upper shell falls into the the vacancy releasing fluorescent X-ray (K_{α} , K_{β}) or auger electron (see Fig. 3.6(b) and (c)). Auger electron produces when fluorescent X-ray kicks out another electron from the same or different shell. Due to an unique of electron orbital, the fluorescent X-ray are characteristic of each element and can be utilized for characterization.

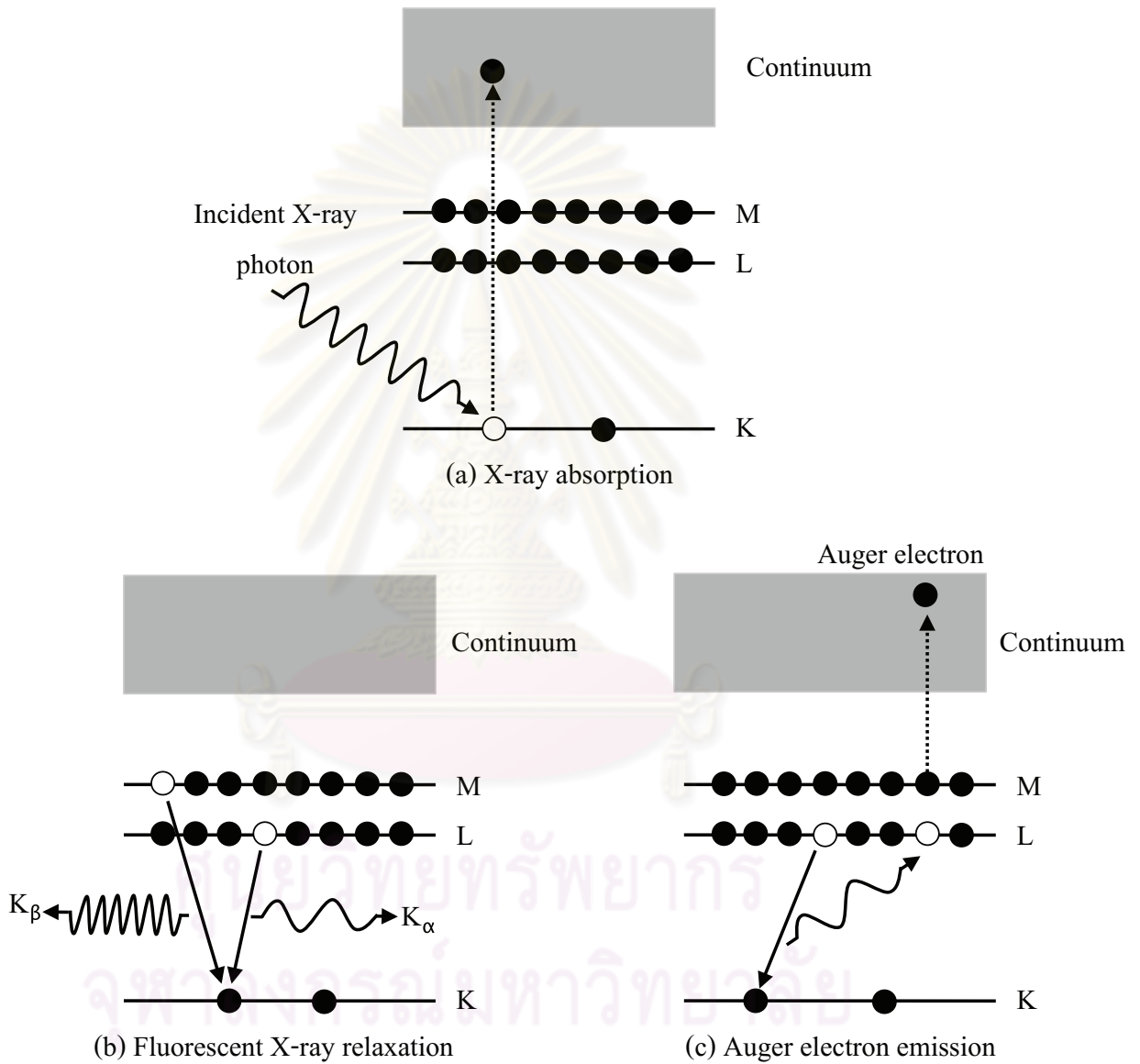


Figure 3.6: Schematic of (a) X-ray absorption, (b) relaxation of electron in excited state emitting fluorescent X-ray and (c) auger electron emission.

There are two modes often taking in XAS measurement including transmission and fluorescent mode. Figure 3.7(a) and (b) illustrate the schematic presentation of transmission and fluorescent mode in XAS measurement, respectively. Transmission mode, the intensity of transmitted beam resulting from the incident beam intensity absorbed by the material. The intensity of transmitted beam gradually decreases according to the Lambert-Beer's law:

$$I_t = I_0 e^{-\mu(E)d} \quad (3.9)$$

where I_0 is the intensity of incident beam, I_t is the intensity of transmitted beam, d is the thickness of the sample and $\mu(E)$ is absorption coefficient which is a function of energy. There is a sharp increase in the absorption as the energy of X-ray equals to the binding energy of core electron. This sharp is called absorption edge. The specific name of absorption edge relates to the shell in which electron absorbed X-ray. For example, the K edge refers to absorption by the electron in K shell. Since the absorption edge corresponds to the binding energy of the electron excited to unoccupied state, the oxidation state of absorbing atom can be determined. In other words, if an atom becomes oxidized, it loses valence electron. The core electron will feel more effective to charge of nucleus making difficult to remove and the value of absorption edge energy is larger than that for unoxidized atom.

Fluorescent mode, this mode performs by detecting fluorescence X-ray using the relation:

$$I_f \propto \mu(E)I_0 \quad (3.10)$$

where I_f is the intensity of fluorescent X-ray. Nevertheless, no matter what mode is used in XAS measurement, the obtained XAS data are similar.

X-ray absorption spectra are typically divided into two main regions, X-ray absorption near edge structure (XANES) and extended X-ray absorption fine structure (EXAFS). Figure 3.8 shows energy ranges in X-ray absorption spectrum. XANES region covers the energy range from slightly below the absorption edge

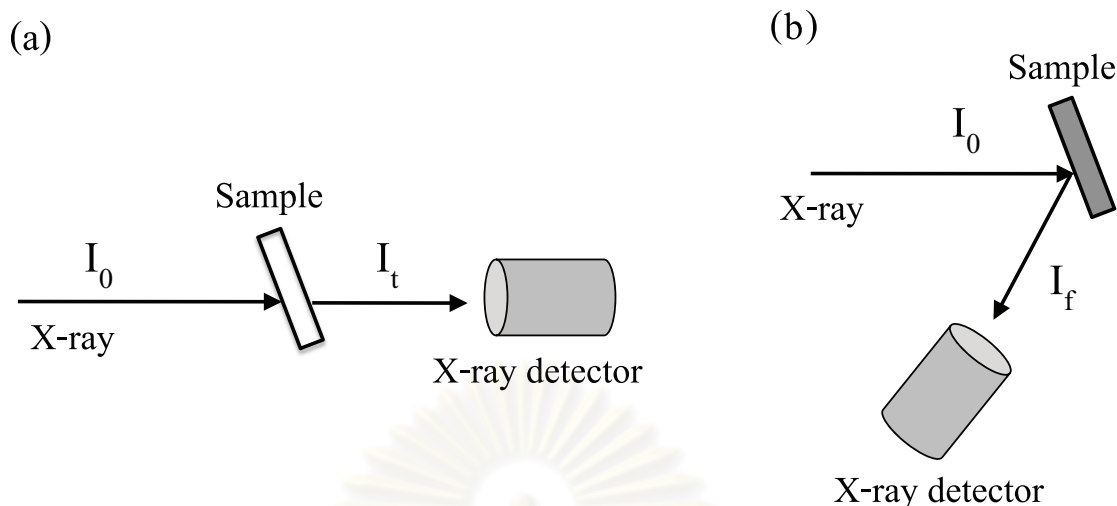


Figure 3.7: Schematic of (a) Transmission mode (b) Fluorescent mode often using in XAS measurement.

extending up to approximately 50 eV off absorption edge [118]. XANES contains information involving the valence number or oxidation state as well as electronic state of probed element. EXAFS region continues to XANES starting from 50 eV up to 1000 eV. The spectrum in EXAFS region appears weak oscillation due to constructive or destructive interference between the outgoing photoelectron wave and backscattered wave from neighbor atom (see Fig. 3.9). EXAFS provides the information concerning interatomic distances and coordination number surrounding absorber atom.

In our XAS experiment, the films were deposited onto silicon substrate in dimension of $2 \times 2 \text{ cm}^2$ to obtain the maximum intensity of X-ray beam. The fluorescent mode was used due to opaque property of the substrate. The XAS spectra were collected on Beamline 8 at Synchrotron Light Research Institute (Public Organization) located at Nakhon Ratchasima, Thailand. Fe foil with absorption edge energy of 7112 eV was used as the standard for calibrating XAS spectra. The sample was placed at the focal spot. All the energies passed through and interacted with the sample. In this work, Fe is probed element and the X-ray absorption energy of Fe^{2+} and Fe^{3+} is approximately 7118 eV and 7123 eV, respectively [119]. Once we know the X-ray absorption edge energy for the

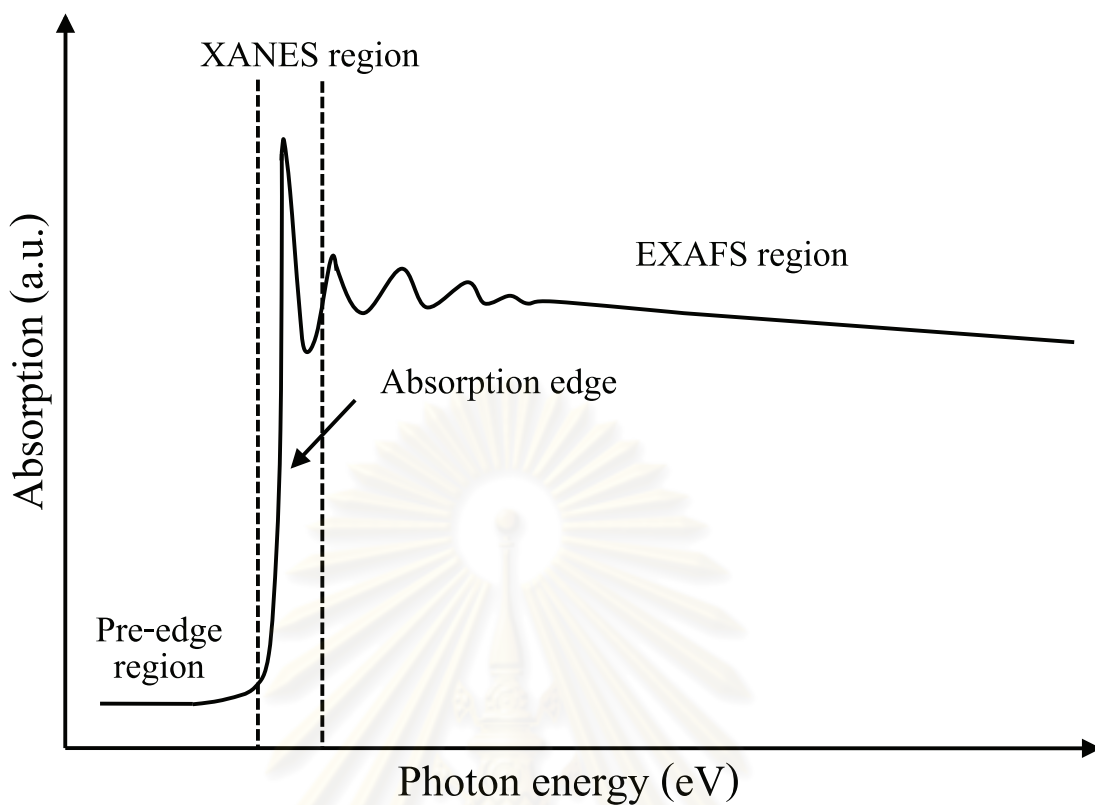


Figure 3.8: XAS spectrum including pre-edge, XANES, EXAFS regions and absorption edge.

probed element, we can easily set the range of X-ray energy scan. Absorption coefficient $\mu(E)$ obtained from I_f/I_0 was plotted as a function of X-ray energy. The absorption edge energy according to oxidation state of Fe in the films was obtained by maximum derivative of the spectra after subtracting pre-edge baseline.

ศูนย์วิจัยทรพยากร
จุฬาลงกรณ์มหาวิทยาลัย

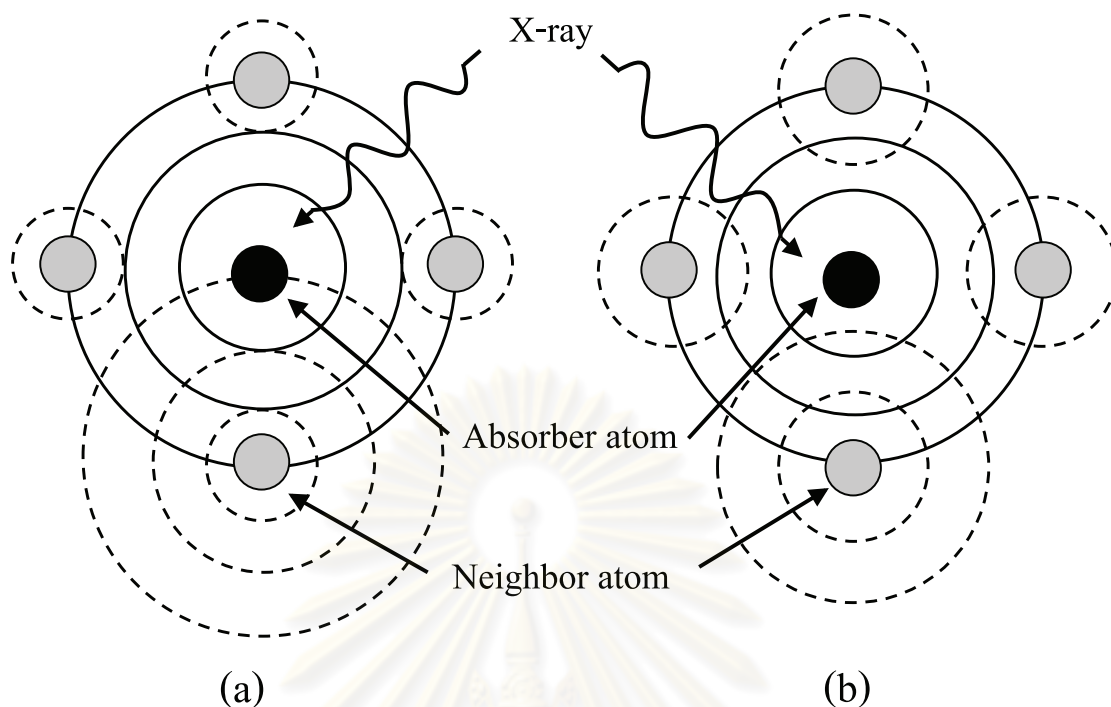


Figure 3.9: Schematics of photoelectron wave outgoing (solid circles) from an absorber atom and backscattering (dashed circles) from neighbor atom (a) constructive interference and (b) destructive interference.

3.4 Ultraviolet-visible spectroscopy

Ultraviolet-visible (UV-Vis) spectroscopy is a type of absorption spectroscopy. The concept in this technique is similar to X-ray absorption spectroscopy which is discussed in previous section. However, UV-Vis spectroscopy is relevant to the absorption spectroscopy in UV-Vis energy range (200-800 nm). In molecules, the energies can be divided into three main parts which are electronic, vibrational and rotational energy. The electronic energy is related to the energy of molecule's electron. The vibrational energy associates with the vibration of atom within the molecule and the rotational energy is relative to the rotation of molecule. Figure 3.10 shows the energy level of molecule. Within electronic states, there are many possible vibrational energy states in which also have many rotational energy states. Since the difference between the electronic energy level is higher than the

energy difference of vibrational and rotational energy, the energies in UV-Vis are enough to promote outer electrons from one electronic energy level to higher one, while vibrational and rotational transition need the lower energy just in the range of infrared and microwave radiations, respectively [120]. At room temperature, most of electrons are in the ground state. Electrons can move to excited state as they absorb the UV or Visible light. The transitions can occur from ground electronic to any vibrational or rotational energy states. However, there is a certain wavelength where the photo energy corresponds to the energy required electron from ground state to excited state.

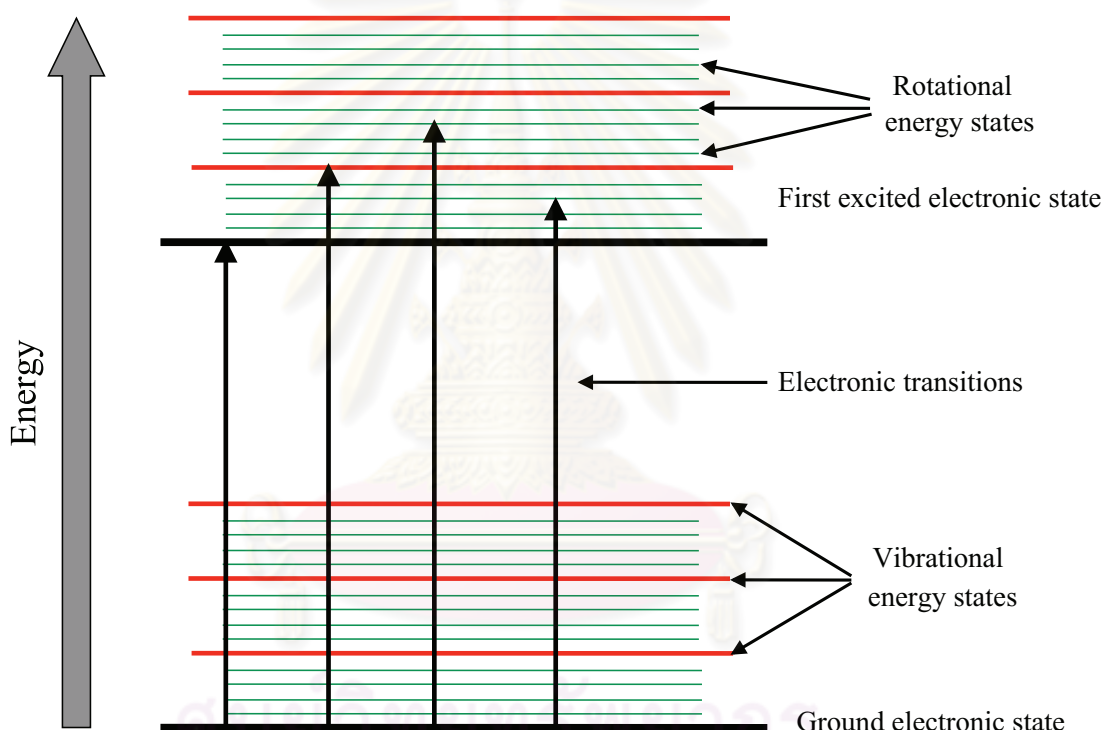


Figure 3.10: Schematic representation of molecule energy showing electronic, vibrational and rotational energy states and electronic transitions.

In this work, absorption spectra were collected by using double beam UV-Vis spectrophotometer (JENWAY: Model 6405 UV/Vis) in over wavelength range 200-800 nm with the scan step of 1 nm. The detector detects the intensity of light passing through the sample (I_t) compared with the intensity of light transmitted through the blank substrate (I_0) which is used as reference. Figure 3.11 shows

schematic of a double beam UV-Vis spectrophotometer. The beam of UV or visible light which is usually produced from deuterium lamp for UV radiation and Halogen lamp for visible radiation is focused on mirror sending the beam hitting a concave diffraction grating to separate into different wavelengths. Each wavelength is divided into two parallel beams having equal intensity by a half-mirror. Each of beams passes through the reference and sample material. The detector records in the percentage ratio of the intensity of light passing through the sample to the reference.

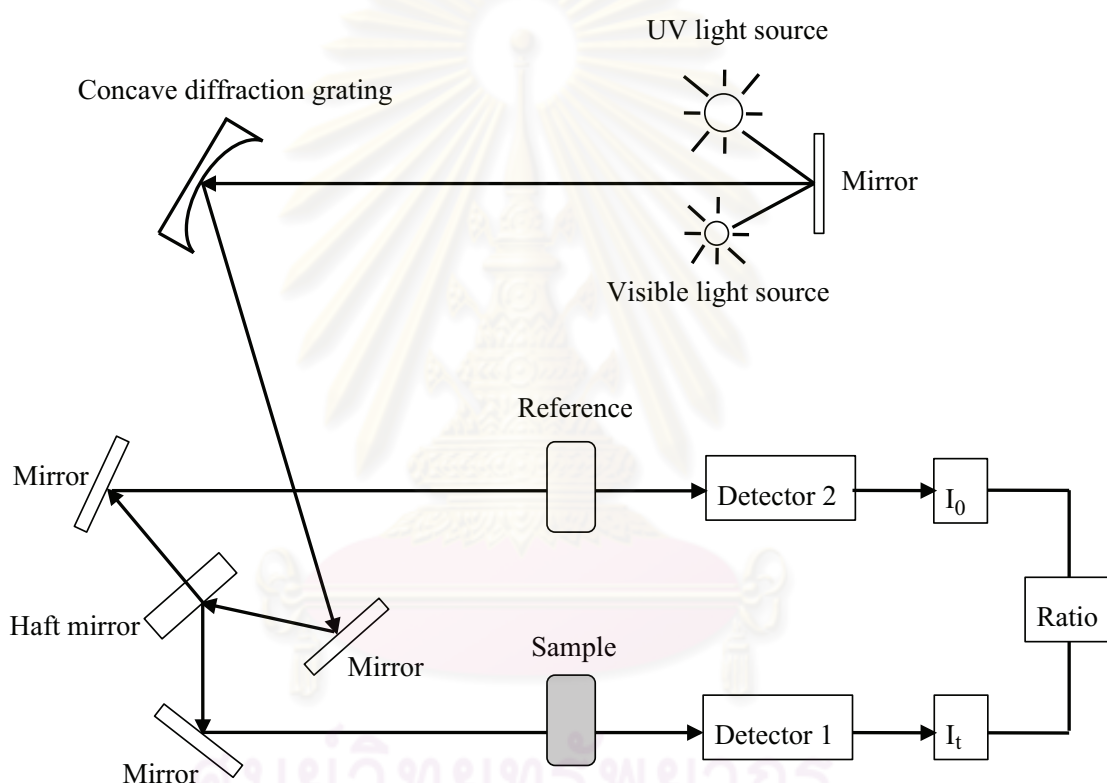


Figure 3.11: Schematic of a double beam UV-Vis spectrophotometer.

The absorbance (A) of sample can be obtained from the relationship as expressed in equation below:

$$A = \log\left(\frac{1}{T}\right), \quad (3.11)$$

where T is transmittance defined as:

$$T = \frac{I_t}{I_0}. \quad (3.12)$$

3.4.1 Determination of refractive index and film thickness

Optical transmission measurements are carried out to determine the film thickness and the optical parameters such as refractive index, extinction coefficient and absorption coefficient depending on the wavelength. In this study, we plot the percentage of transmittance as a function of wavelength. The optical parameters can be obtained using envelope method derived by Swanepoel [121]. Swanepoel's method is based on the assumption that both film and substrate are homogeneous and have uniform thickness [121]. In this thesis work, the multilayer films of BaTiO₃ and SrTiO₃ were deposited on ITO coated on glass substrate. Since the refractive index of BaTiO₃ and SrTiO₃ can be comparable (2.15-2.55 for crystallized BaTiO₃ in the 200-800 nm wavelength range [122] and 2.15-2.35 for crystallized SrTiO₃) [123], which can be considered that their densities are very close. Base on this assumption, the films are homogeneous, so we can use Swanepoel's method to obtained refractive index and extinction coefficient of SrTiO₃/BaTiO₃ multilayer films. Schematic of the optical transmittance spectra which are enveloped is presented in Fig. 3.12.

From enveloped of the optical transmittance, the refractive index as a function of wavelength ($n(\lambda)$) can be obtained from the equation below:

$$n(\lambda) = [N + (N^2 - n_s^2)^{1/2}]^{1/2}, \quad (3.13)$$

where

$$N = \frac{(n_s^2 + 1)}{2} + 2n_s \frac{(T_{\max} - T_{\min})}{T_{\max} T_{\min}}. \quad (3.14)$$

n_s is the refractive index of the substrate, T_{\max} and T_{\min} are the maximum and minimum envelopes of transmittance, respectively (see Fig. 3.12). T_{\max} and T_{\min} are considered to be continuous functions of wavelength. The extinction coefficient which refers to absorption length can be determined from:

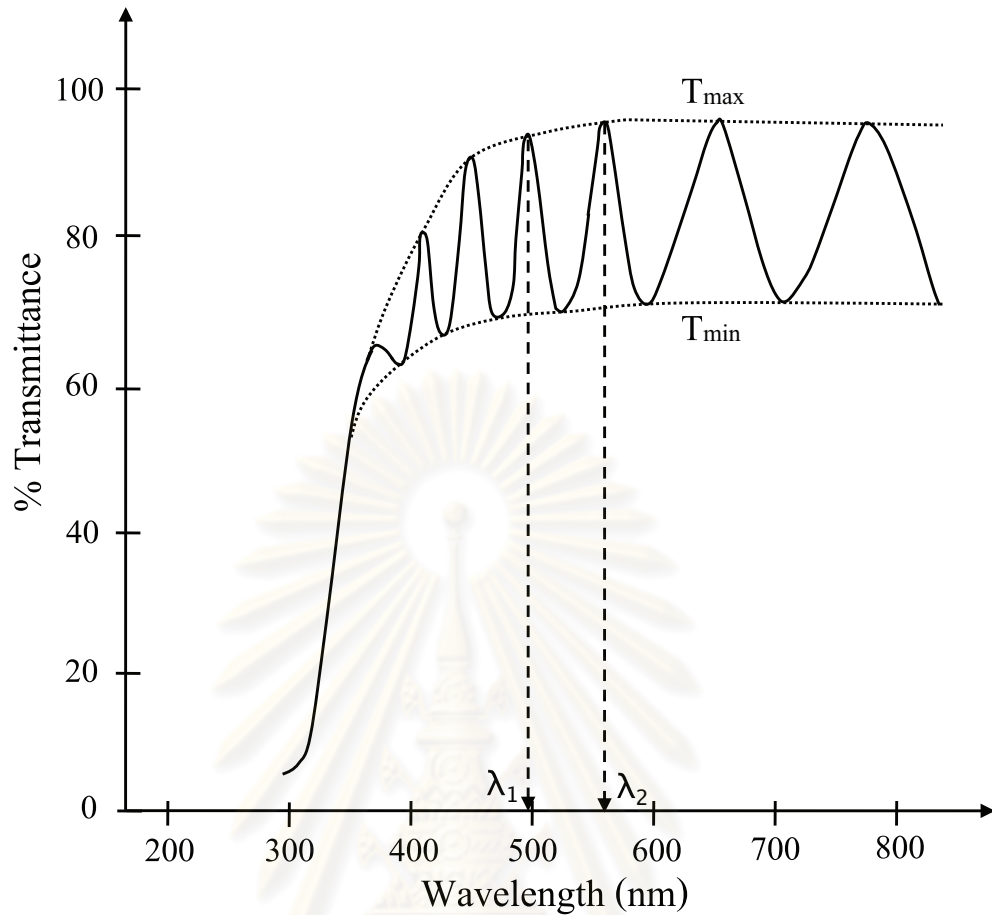


Figure 3.12: A sketch of envelope of the optical transmittance.

$$k = \frac{\alpha \lambda}{4\pi}, \quad (3.15)$$

where α is absorption coefficient calculated from:

$$\alpha = \frac{1}{d} \ln \frac{(n-1)(n_s-n)[1 + (T_{\max}/T_{\min})^{1/2}]}{(n+1)(n_s-n)[1 - (T_{\max}/T_{\min})^{1/2}]}, \quad (3.16)$$

here d is the film thickness.

The thickness of the films obtained from the refractive index corresponding to two adjacent maxima of transmittance according to wavelengths λ_1 and λ_2 was derived from equation 2.10 which we can write:

$$2n_1d = (m + \frac{1}{2})\lambda_1, \quad (3.17)$$

$$2n_2d = (m + \frac{1}{2})\lambda_2. \quad (3.18)$$

From equation 3.17 and 3.18, the films thickness can be solved as expressed follow:

$$d = \frac{\lambda_1\lambda_2}{2[n(\lambda_1)\lambda_2 - n(\lambda_2)\lambda_1]}. \quad (3.19)$$

Another issue is about the refractive index of substrate (n_s) in Sawannepoel's equation, whether we will use the refractive index of glass or the ITO. Actually, we have to use the refractive index of ITO coated on glass substrate as to be the refractive index of substrate in Sawannepoel's equation. However, we do not know the refractive index of ITO coated on glass substrate due to the fact that it consists of 2 layers of ITO and glass. In our experiment, the thickness of ITO coated on glass substrate is 100 nm which is smaller than that of glass substrate with the thickness of 1.2 mm. From this reason, we can assume the refractive index of total substrate to be approximated the refractive index of glass, 1.47 for this crude calculation.

3.4.2 Determination of energy gap and Urbach energy

The fundamental absorption is associated with exciton transition corresponding to the selection rules. The relation between absorption coefficient and optical band gap or energy gap (E_g) derived by Tauc [124] is given by the following equation:

for direct transition

$$(\alpha h\nu)^2 \sim (h\nu - E_g), \quad (3.20)$$

and for indirect transition

$$(\alpha h\nu)^{1/2} \sim (h\nu - E_g), \quad (3.21)$$

where $h\nu$ is photon energy. Since envelope method is not valid in the strong absorption region, the absorption coefficient is obtained from Lambert-Beer's law:

$$\alpha = \frac{1}{d} \ln\left(\frac{1}{T}\right). \quad (3.22)$$

The energy gap can be determined by plotting $(\alpha h\nu)^n$ ($n=2$ for direct band gap and $n=1/2$ for indirect band gap) versus $h\nu$ and extrapolating the linear portion of the plot to $(\alpha h\nu)^n = 0$, in the other words, the energy gap is the photon energy at the point where $(\alpha h\nu)^n = 0$.

The exponential increase of the absorption coefficient with the photon energy was firstly discovered by Urbach in silver bromide [125]. The optical absorption spectra show the tail before absorption edge. The tail part near the absorption edge follows the expression:

$$\alpha = \alpha_0 \exp\left(\frac{\sigma(h\nu - E_0)}{kT}\right) = \alpha_0 \exp\left(\frac{h\nu - E_0}{E_U}\right), \quad (3.23)$$

where σ is the steepness parameter, α_0 and E_0 are the Urbach bundle convergence point coordinates. k is the Boltzmann constant and T is the temperature. E_U is Urbach energy which is equal to the absorption edge energy width. By plotting $\ln\alpha$ versus $h\nu$ near absorption edge, the Urbach energy can be obtained from inverse of the slope of straight line of the plot. The presence of band tail near absorption edge is due to having the localized state in the band gap depending on structural defect.

3.5 Atomic force microscopy

Atomic force microscopy (AFM) has become an important characterization technique for investigating surface morphology in microscopic level. AFM utilizes atomic force between a tiny cantilever tip (mostly used silicon tip) and sample. The tip is attached to the end of cantilever and beneath the cantilever with a low spring constant. As a laser beam focuses on the end of cantilever and the sample is then scanned beneath the tip, the tip is either repelled by sample surface or attracted to surface leading to the cantilever deflection. The photodetector records

the changing vertical position of the laser beam reflecting off the cantilever as shown in Fig. 3.13, which indicates the local height at that location on the sample.

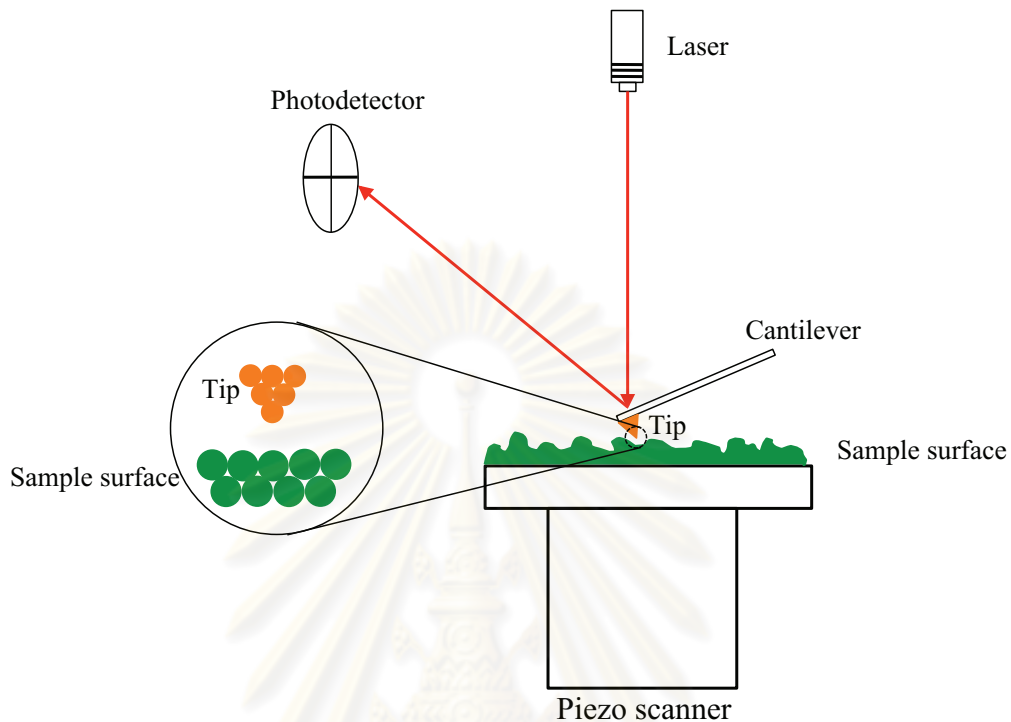


Figure 3.13: Schematic of atomic force microscope.

There are three modes in AFM, which are contact mode, non-contact mode and tapping mode. The interactive force between an atom of the tip and the surface in each mode follows Lennard-Jones potential as demonstrated in Fig. 3.14. In the contact mode, the tip scans sample closing to the sample surface with a distance of a few angstroms. The tip is pushed against the sample due to repulsive force. By maintaining the constant distance between the tip and the sample surface, the force between them is obtained according to Hooke's law:

$$F = -kx, \quad (3.24)$$

where F is force, k is the spring constant of cantilever and x is cantilever displacement. Contact mode in AFM is mostly used for high resolution image due to generating large repulsive force on the surface. Nevertheless, in this mode the sample can be damaged, non-contact mode is introduced to characterize the sample

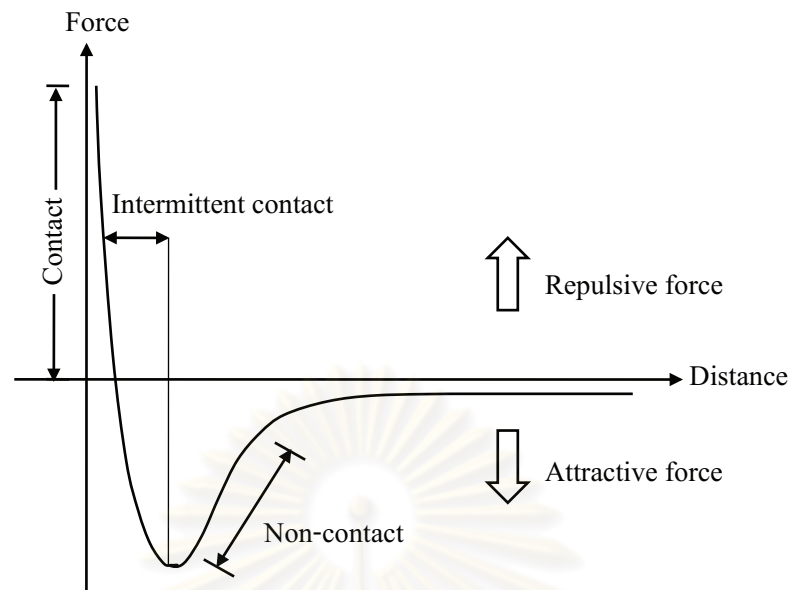


Figure 3.14: interaction force between an atom at the apex of the tip and an atom in the sample surface as a function of distance between the tip and the surface following Lennard-Jones potential.

having soft surface. In non-contact mode, the tip and the sample surface are held in the distance of 2-30 nm which is much larger than that in contact mode. When the sample is scanned underneath the tip with maintaining distance constant, the attractive forces between the tip and the sample are detected. In non contact mode, AFM measures weak Van der Waals forces due to fluctuating tip. Since the magnitude of force in non-contact mode is smaller than that in contact mode, the data could not be accuracy. Thus, tapping mode is developed for obtaining more quality images. Tapping mode is hybrid between contact and non-contact mode. In this mode, the cantilever is oscillated at its resonant frequency so that the tip just taps the sample surface. This mode has advantages beyond the two modes mentioned earlier that the sample is not damaged by the tip and the detector records the large signal of repulsive force.

In this thesis, we used tapping mode of AFM model Veeco Nanoscope V for investigating the surface morphology of the films. The films were scanned in the dimension of $0.3 \times 0.3 \mu\text{m}^2$.

CHAPTER IV

EXPERIMENTAL DETAILS

In the first section of this chapter, we will present the details of film deposition including precursor synthesis, substrate preparation, film growth conditions as well as the procedure for film deposition by using spin coating technique. Then, the details of device fabrication such as mask fabrication and electrode deposition will be described. The last of this, the measurement parts for characterizing gas sensing and dielectric properties as well as conversion of dielectric constant from capacitance of the films will be presented.

4.1 Synthesis of BaTiO₃ and SrTiO₃ precursors

Analytical grade barium acetate (Ba(CH₃COO)₂) (99.5%)[Aldrich], strontium acetate (Sr(CH₃COO)₂) (99.5%)[Aldrich], titanium n-butoxide (Ti(C₄H₉O)₄) (99%)[Acros organics], acetic acid (CH₃COOH) (99.7%)[Mallinckrodt], methanol (CH₃OH) (99.8%)[Ajax finechem] and lab chemical grade iron (II) sulphate (FeSO₄·7H₂O) (98%)[Ajax finechem] were used as the starting materials.

Figure 4.1 illustrates the layout of the synthesis of undoped BaTiO₃ and SrTiO₃ as well as the detail is elaborated as follows. 0.02 mol barium acetate (2.5588 g) or strontium acetate (2.0567 g) was first dissolved separately into 20 ml (21 g) acetic acid to obtain a light yellow transparent solution for BaTiO₃ and a colorless SrTiO₃ solution. After homogenization, 0.01 mol (3.4378 g) titanium n-butoxide was added to the solution and followed by addition of 1.75 ml (1.3884 g) methanol to reduce viscosity and prevent the formation of a precipitate of TiO₂.

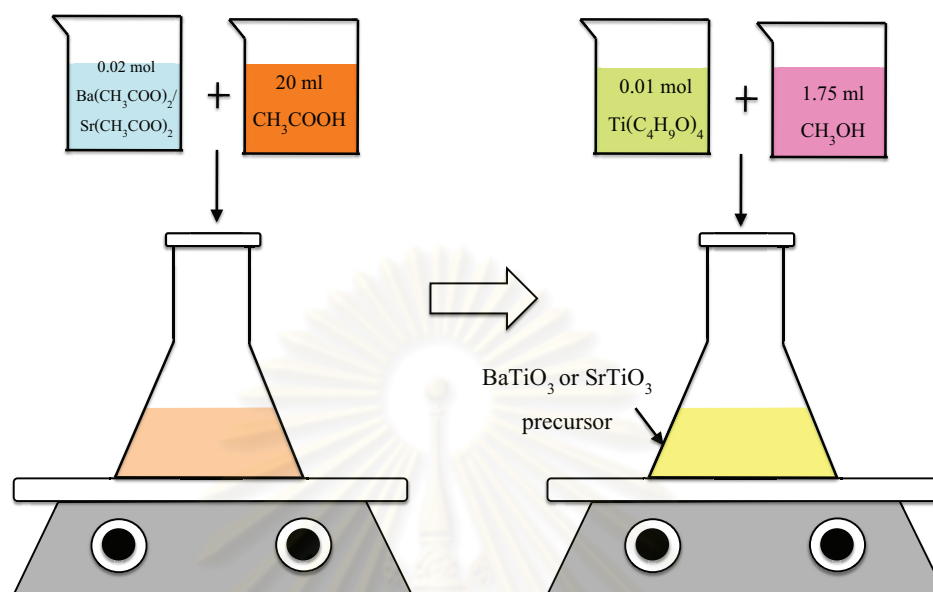


Figure 4.1: The layout of synthesis of barium titanate or strontium titanate by sol gel method.

The whole process of synthesis the precursor was done in an ambient atmosphere at near $60\text{ }^{\circ}\text{C}$ with stirring on a hot plate at which sol-gel reaction gradually takes place. For synthesis Fe-doped BaTiO_3 or SrTiO_3 precursor, iron (II) sulphate was added to the solution after achieving uniformity of barium acetate or strontium acetate in acetic acid. In this thesis, the Fe doping concentrations were varied to 2 wt%, 4 wt% and 8 wt%, respectively.

4.2 Substrate preparation and conditions for film deposition

In this study, $\text{SrTiO}_3/\text{BaTiO}_3$ multilayer films were deposited on different types of substrate depending on their applications. To investigate their optical properties, indium tin oxide (ITO) coated on a glass substrate with dimension

2.5x2.5 cm² was used as a substrate. ITO films were prepared by rf-magnetron sputtering method under argon plasma to a thickness of 100 nm. The ITO films were post-annealed at 400 °C for 90 min in a argon atmosphere. The ITO deposition process was done at Department of Physics, Faculty of Science, Mahidol University by Dr. Somsak Dangtip, Mr. Ponyachai Learngarunsri and Mr. Narong Boonyopakorn. The typical resistivity of the ITO film was 3x10⁻⁴ ohm cm with transparency above 90% in the visible region. Single side polished silicon wafer with (100) plane having dimension of 2x2 cm² was used as a substrate to examine oxidation state of iron. To characterize their electrical properties including dielectric constant as well as gas sensing performance by mean of the change in the resistance, alumina (Al₂O₃) wafer (99.6%) with dimension of 2x2.5 cm² was selected to be a substrate due to its insulator property and low cost. The alumina wafer substrates were purchased from Semiconductor Wafer, Inc (<http://www.semiwafer.com>). Some physical properties of alumina substrate using in this work are presented in Table 4.1.

Table 4.1: The physical properties of alumina substrate.

Physical properties	
Crystal structure	Rhombohedral (at room temperature)
Lattice parameters	a=4.7587 Å and c=12.9929 Å
Density	3.85 g/cm ³
Dielectric constant (at 1 MHz)	9.8 at 300 K
Loss tangent (at 1 MHz)	0.0002 at 300 K
Melting point	2052 °C
Thermal expansion (x10 ⁻⁶ °C ⁻¹)	8.2

Prior to the film deposition, the substrates were cleaned by detergent. They were then ultrasonically cleaned for 20 min in acetone, methanol and followed by deionized water, respectively. Finally, they were dried with a nitrogen blowgun.

As mentioned earlier, the films were investigated in their two main proper-

ties. One is optical properties and another is electrical properties. The first stage, we focused on the effect of annealing temperature on their optical properties. The films with two layers of SrTiO₃ and BaTiO₃ which were alternating deposited were grown. The reason that only two film layers were deposited is to meet the need of making it as a thin buffer for flat panel applications. Annealing temperatures were varied to identify the best crystal structure of the films. The maximum annealing temperature was limited at 650 °C to avoid softening and deformation of the glass substrate. For the films using for electrical characterization, they were deposited with five layers of undoped and Fe-doped SrTiO₃ and BaTiO₃ as well as varied Fe doping contents. This is to ensure that we obtained the film thickness thick enough to measure the electrical properties of the films. The annealing temperature was kept constant at 1000 °C. Lists of desired layer structure to grow the films, the annealing temperature as well as the used substrate in this study are given in Table 4.2. Fig. 4.2 shows the schematic of desired layer structure of the films. S/B refers to the top and the bottom deposition being SrTiO₃ and BaTiO₃, respectively. In this case, BaTiO₃ was deposited first and followed by SrTiO₃. S/B/S/B/S is relevant to the first layer being SrTiO₃ grown alternating with BaTiO₃ until five layers were completed. S/S/S/S/S refers to the films deposited by SrTiO₃ with five layers and B/B/B/B/B is relevant to the films grown by BaTiO₃ until we obtained the films with five layers. For the case of S/B/S/B/S doped with Fe, the layer structure is the same with that of undoped S/B/S/B/S films. For example, to grow 2 wt% Fe-doped S/B/S/B/S the first layer was done by 2 wt% SrTiO₃ deposited alternating with 2 wt% BaTiO₃ until the films have five layers.

4.3 Spin coating process

In this thesis, the films were grown by using spin coating technique. This technique is simpler and cheaper than others, as well as doping by using such technique can be done easily. Beside the capability to produce a large surface

Table 4.2: Deposition conditions for film growth.

Investigated properties	Structure of deposited films	Annealing temperature (°C)	Used substrate
Optical	Undoped S/B	300, 400, 500 550, 600 and 650	ITO coated on a glass
Electrical	Undoped S/S/S/S/S Undoped B/B/B/B/B Undoped S/B/S/B/S 2, 4 and 8 wt% Fe-doped S/B/S/B/S	1000	Alumina

coating, the spin coating technique can also perform in the real application in industrial manufactures. Figure 4.3 shows the photograph of the spin coater used in this thesis (Model: P6700 series).

The procedure for the film deposition as illustrated in Fig. 4.4 is described by the following. The synthesized precursor solutions are undoped SrTiO_3 and BaTiO_3 , Fe-doped SrTiO_3 and BaTiO_3 . The desired precursor was spun onto the cleaned substrate with the spinning speed of 1000 round per minute (rpm) for 45 second. After the first deposition, the films were preheated on a hot plate at 120 °C for 20 min to remove the solvent. They were then heated up at rate of 10 °C per minute from room temperature to desired temperature in a furnace (Model: Carbolite RHF 17/10). The desired temperature was held for 20 min, then cool down in air atmosphere to room temperature. The same procedure was done with the solution until we meet the films with desired structure as shown in Table 4.2. The schematic of annealing process is demonstrated in Fig. 4.5.

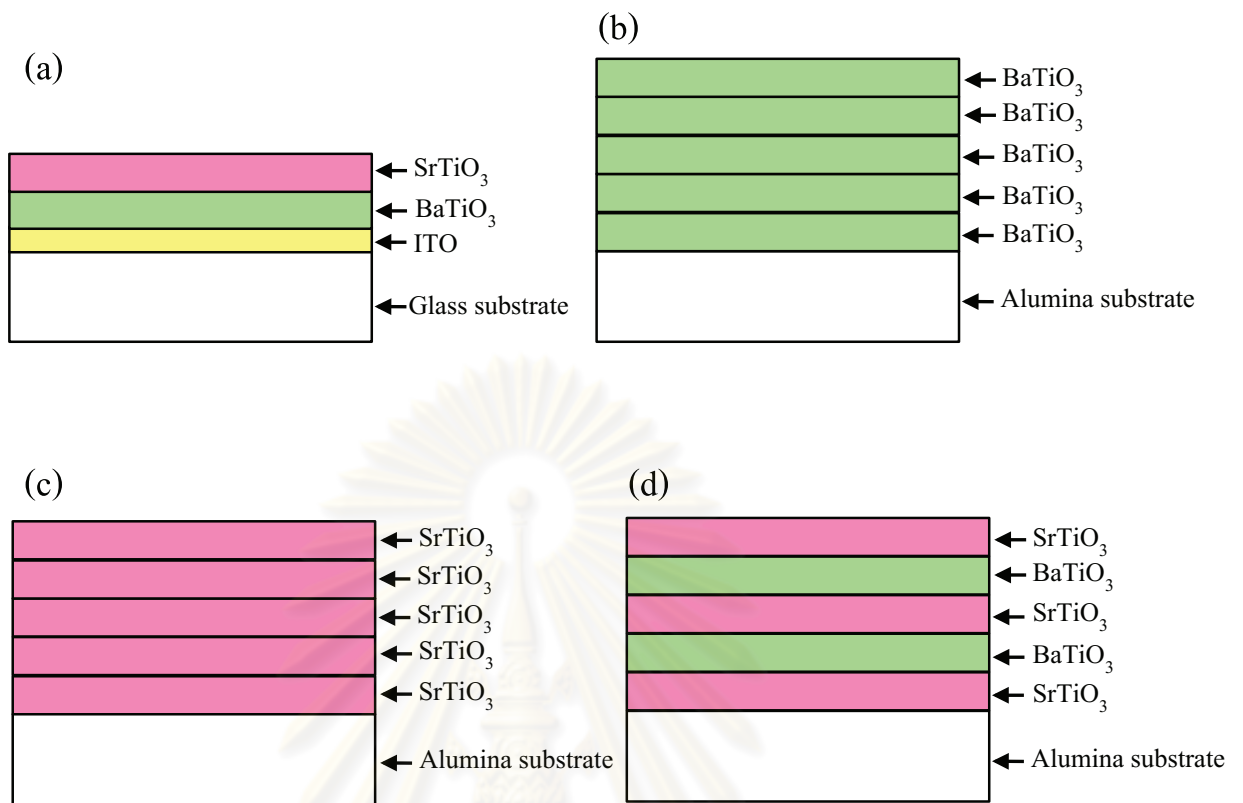


Figure 4.2: Schematic representation of (a) SrTiO₃/BaTiO₃ film on ITO coated on glass substrate, (b) BaTiO₃/BaTiO₃/BaTiO₃/BaTiO₃/BaTiO₃ film on alumina substrate, (c) SrTiO₃/SrTiO₃/SrTiO₃/SrTiO₃/SrTiO₃ film on alumina substrate and (d) SrTiO₃/BaTiO₃/SrTiO₃/BaTiO₃/SrTiO₃ film on alumina substrate.

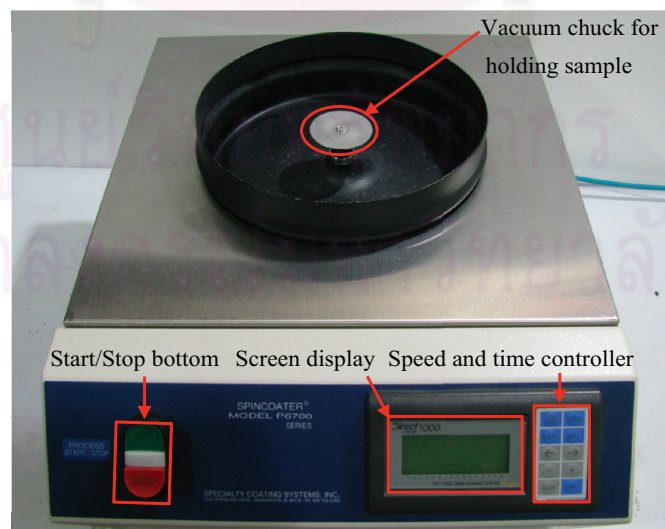


Figure 4.3: The photograph of spin coater machine model P6700 series.

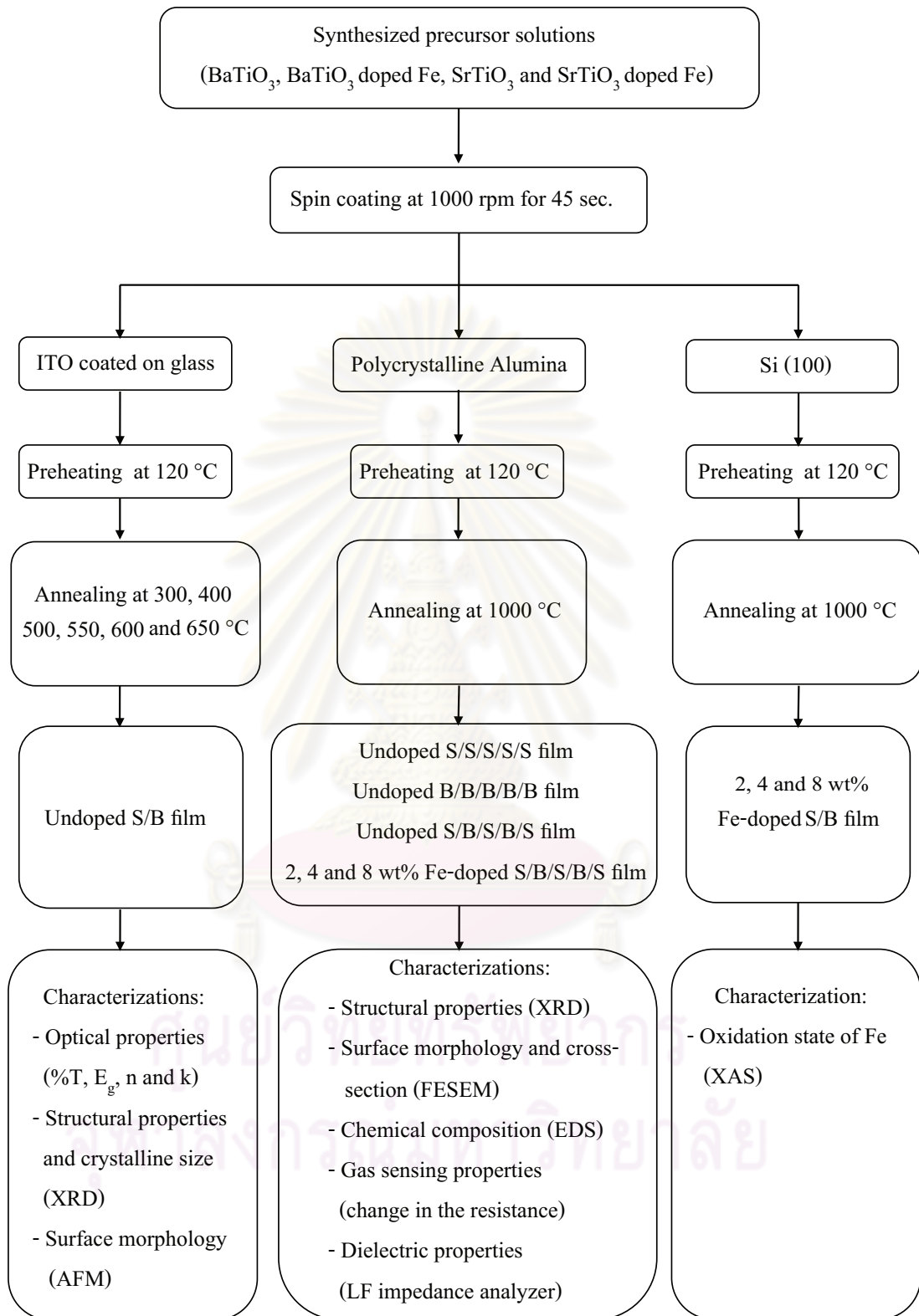


Figure 4.4: The flow chart for multilayer film deposition with different growth conditions by spin coating process.

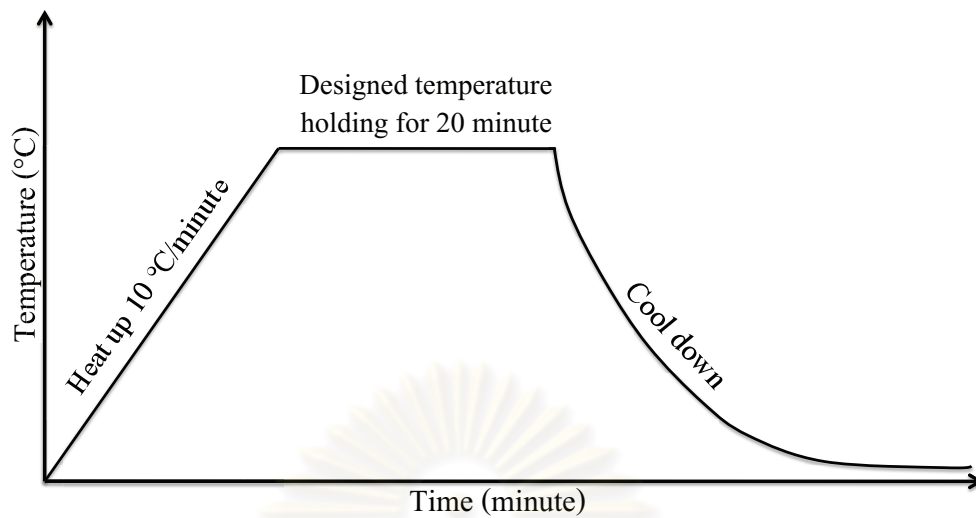


Figure 4.5: The schematic of annealing process.

4.4 Fabrication of device

In this work, the films were fabricated as a device including capacitor and gas sensor. The electrode needs to be applied onto the film surface. Many electrode geometries, for instance, top/bottom, intermediated, transmission line and interdigitated electrode have been used with a device [113, 126, 127]. Among of these electrode configurations, interdigitated geometry has outstanding advantage that is allowing a large contact area between electrode and film on the whole small footprint. It has been reported that the electrode configuration and its parameter such as electrode width and spacing as well as overlapping figure length have an impact on electrical properties of the films [128, 129, 130]. Hong et al. studied the effect of different electrode configurations on the dielectric properties of lanthnum-doped lead titanate thin film. Their work presented that the dielectric constant of the film with interdigitated electrode was larger than that of the films with parallel electrodes under the same technological conditions [131]. This could be due to the more leakage current in form of parallel electrodes. Another study by Li et al. showed that the device with interdigitated electrode exhibited higher

capacitive humidity sensitivity of silicon nanoporous pillar array than that of device with two-side comb electrodes [132]. In this study, therefore, the electrode which is designed with interdigitated structure was used for measuring dielectric constant as well as detecting changes in the electrical properties of sensing films. All of parts for fabricating device including mask fabrication as well as electrode deposition were done at Nanoelectronics and MEMS Laboratory, National Electronics and Computer Technology Center (NECTEC). The detail for fabricating device is described in next section.

4.4.1 Mask fabrication

In this study, the electrode was deposited on the film surface through a shadow mask which was created by photolithography (lift-off) technique. Such technique is widely used for making pattern in micro scale. The configuration of interdigitated electrode using in this study is illustrated in Fig. 4.6. The gap width and their coinciding figure length were about $100\ \mu\text{m}$ and $1500\ \mu\text{m}$, respectively.

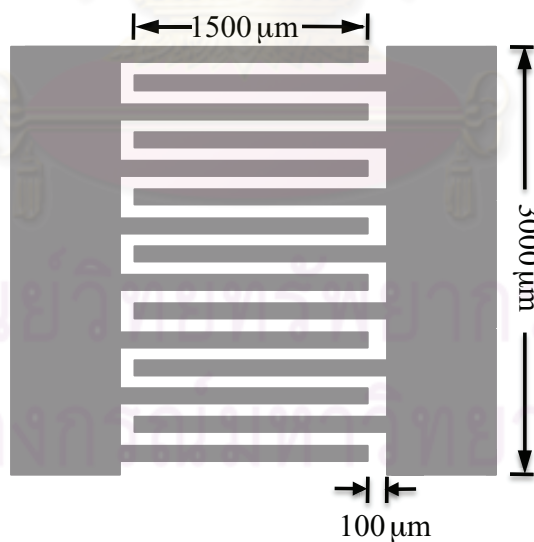


Figure 4.6: The schematic of configuration of interdigitated electrode.

The schematic of photolithography process steps as presented in Fig. 4.7 and detail are expressed by the following;

1. A stainless steel with 5 mm thickness was used as a substrate. It was cleaned by detergent and it was then blown to dry with nitrogen stream.

2. Cleaned stainless steel substrate was coated with a positive photo resin film which is a light sensitive resist by using a LAM-150 dryfilm laminator at temperature about 100 °C.

3. Interdigitated pattern which was printed on transparent sheet containing 90 pieces of configuration was put on the resist and they were then exposed to ultraviolet light by UV-800 crystal machine for 10 second. In this stage, the image was created that the exposed region of the resist becomes pale region; whereas, the unexposed area of that transforms opaque area.

4. Due to solubility property of the resist after irradiated by ultraviolet light, photoresist (region of exposed resist) was removed in the developing fluid (developer) that swells which remained the option of the unexposed resist generating inverse patterning.

5. The whole substrate was deposited with Nikle (Ni) material by electroplating process. In this process, current was increased according to operating time as shown in Table 4.3.

6. The last step, the substrate was placed in solvent to dissolve and remove the remaining resist together with the Ni mask. The photograph of Ni mask is shown in Fig. 4.8.

Table 4.3: The current and time using in electroplating process.

Current (A)	Time (hour)
0.3	0.5
0.6	0.5
0.9	1
1.2	3

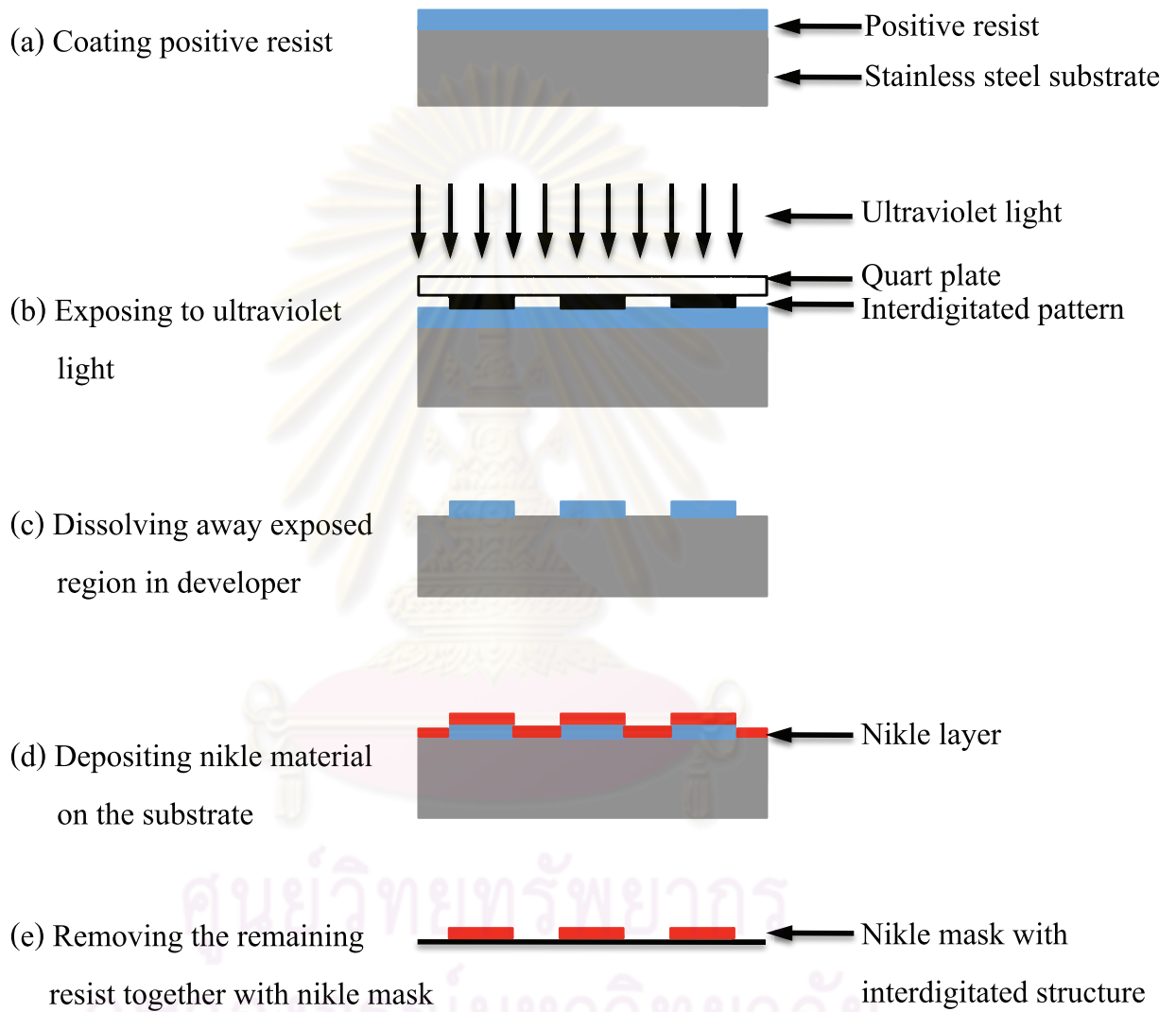


Figure 4.7: The schematic of photolithography process steps.

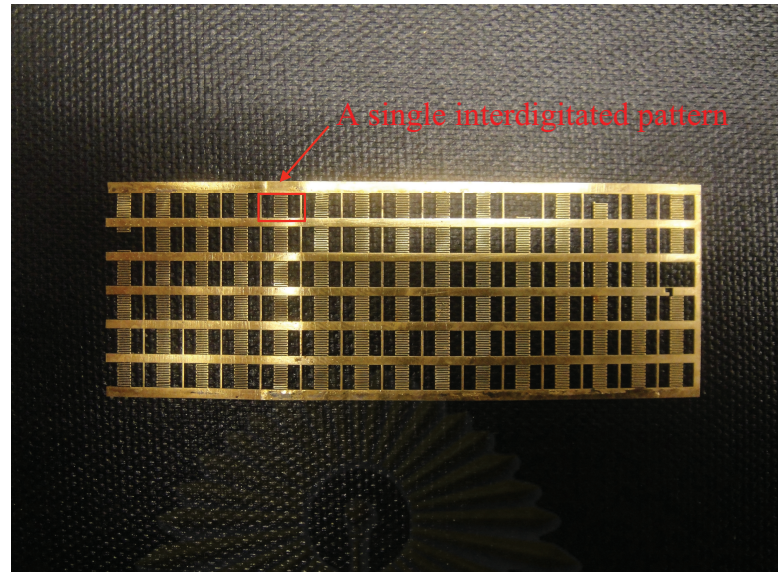


Figure 4.8: A photograph showing a set of Ni interdigitated mask containing 90 pieces of configuration.

4.4.2 Electrode deposition

After electroplated mask was obtained, the electrode was applied on the film surface by using a DC sputtering technique. In sputtering process, we used aligned several small magnets to attach the nickel mask with the films closely (see Fig. 4.9). Chromium (Cr) was firstly sputtered on the films with the thickness about 50 nm and followed by gold (Au) with the thickness about 200 nm. The chromium was utilized to improve the adherence between the surface of films and the gold. Because we obtained the films with electrode in the form arrays of devices, a dicing saw (Model: ADT 7100 series 2 VECTUS) was utilized to separate arrays of devices come out as a single of device. The dimension of a device as shown in Fig. 4.10 was about $2 \times 3 \text{ mm}^2$.

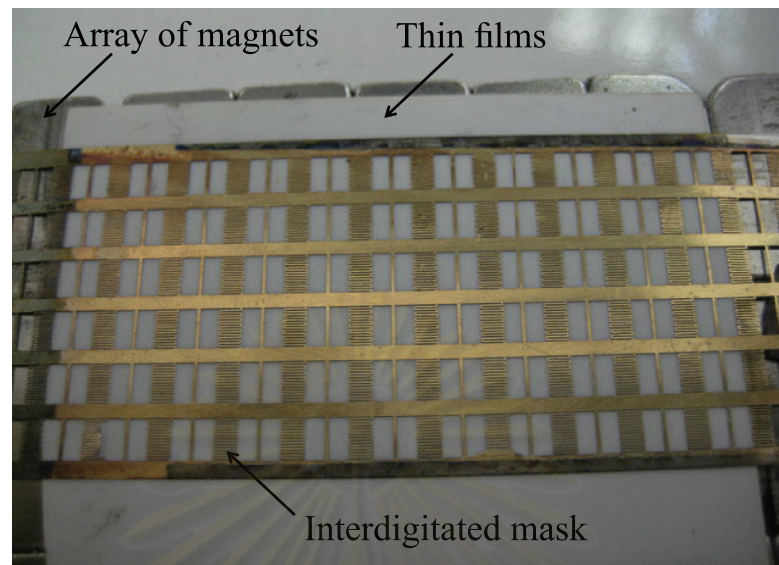


Figure 4.9: The photograph showing the interdigitated mask mounted the films closely by using array of magnets.

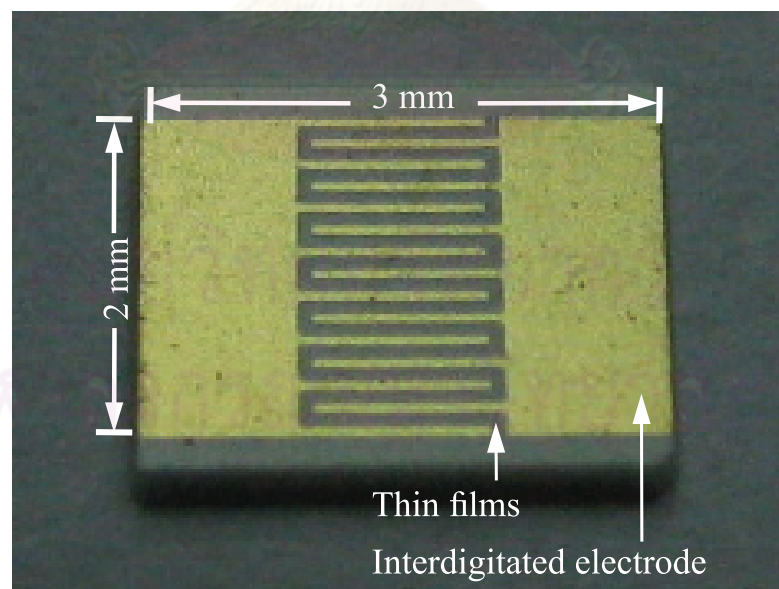


Figure 4.10: The photograph of a device.

4.5 Gas sensing property measurement

Gas sensing characterization was carried out at Nanoelectronics and MEMS Laboratory, National Electronics and Computer Technology Center (NECTEC). Figure 4.11 shows schematic set up for gas sensing measurement. In the schematic diagram, it consists of three main parts as the following;

1) Gas testing chamber, inside the chamber the sensors were placed on the a stage which was heated by Ni-Cr heater controlled by varying the supply voltage from power supply and thermocouple was used to monitor the temperature of the stage. Figure 4.12 shows the gas testing chamber and Fig. 4.13 shows the stage and probes used for measuring the resistance of the films.

2) Gas flowing system comprises of purified air (Air zero, 99.99%) tank and ethanol vessel. The flow rate of gases was controlled by mass flow controller.

3) Temperature controller and measuring circuit were operated by Labview program (national instrument).

In this study, ethanol vapor (C_2H_5OH) was chosen as examining gas to characterize the gas sensing properties of the films. It was received by flowing purified air through a vessel of ethanol generating bubbles. Total flow of ethanol vapor and purified air was kept constant of 2000 sccm. The ethanol vapor and purified air were then mixed in different proportions to obtained desired concentrations which were flowed into the chamber through mass flow controller. For example, in the case for characterizing gas sensing properties of the films toward ethanol vapor concentration of 100 ppm, we flowed purified air with flow rate of 1990 sccm and ethanol vapor with flow rate of 10 sccm. In this work, the desired ethanol concentrations using in this study are 100, 200, 300, 500 and 1000 ppm. The sensors were heated by Ni-Cr heater to different operating temperatures which are 250 °C and 350 °C

In order to characterize gas sensing, after the sensors were probed already, purified air was introduced into the testing chamber with constant rate of 2000

scm for 15 min to generate the base line. After that, the sensors were exposed to desired ethanol vapor concentration for 5 min. After completing 5 min the ethanol vapor flow was stop whereas the purified air was immediately introduced to the chamber for 15 min for each concentration. Digital multimeter (Model: Fluke 8845) interfaced with Labview software was utilized to measure the film resistances which were continuously monitored with DC voltage across the films of 10 volt . The sensor responses are based on the change in resistance of the sensor after exposing to the gas.

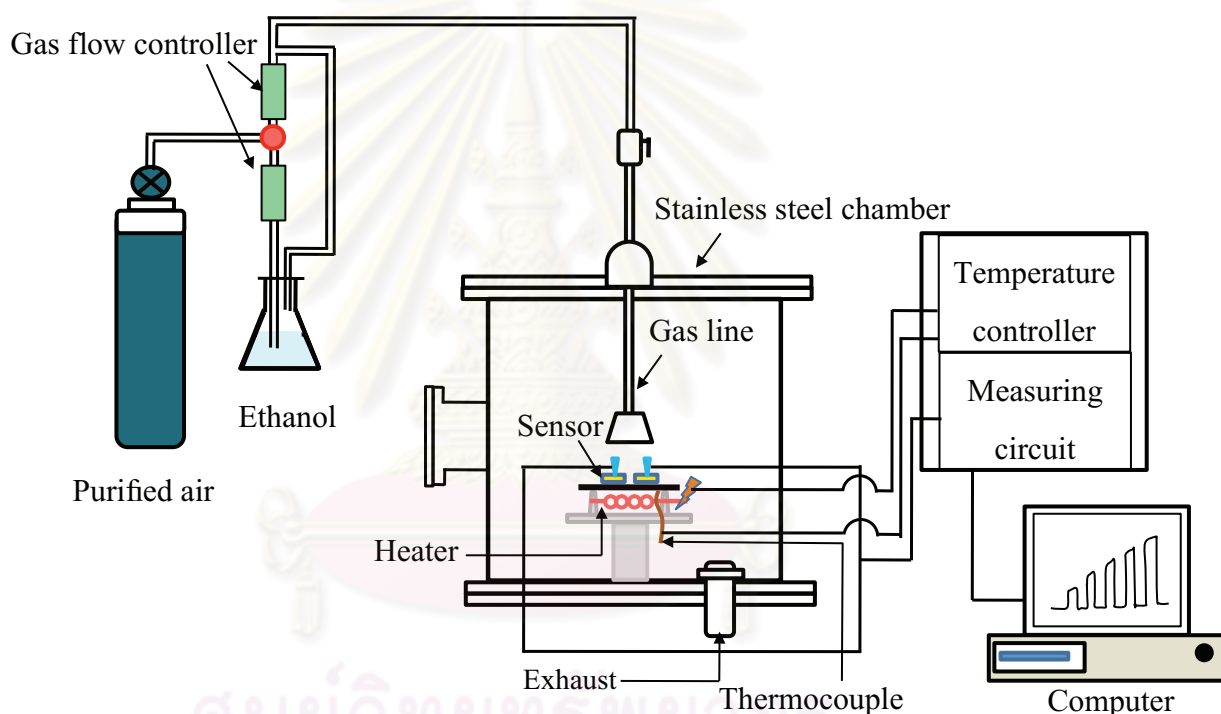


Figure 4.11: Schematic set up for gas sensing measurement.

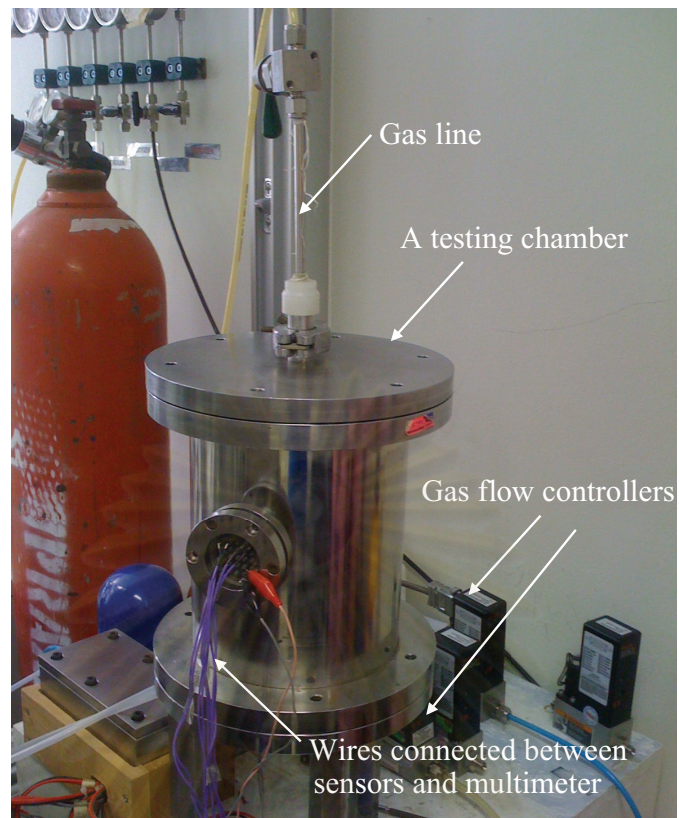


Figure 4.12: A gas testing chamber.

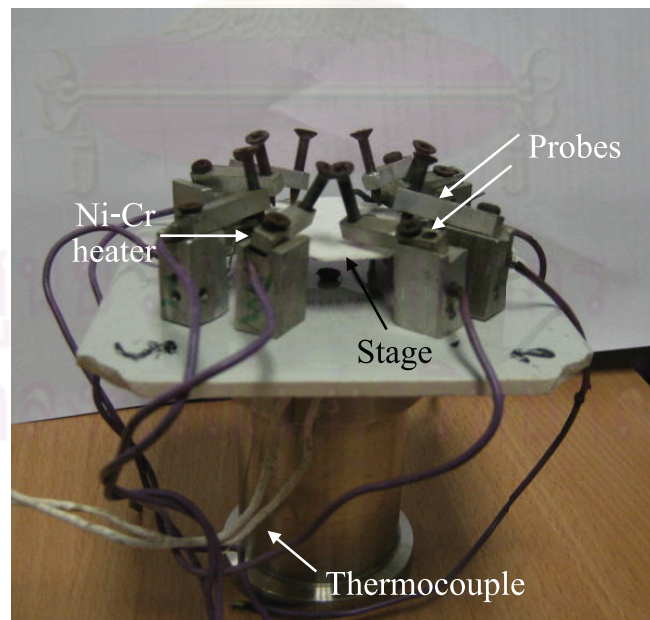


Figure 4.13: The photograph presenting the stage and probes used for measuring the resistance of the films .

4.6 Gamma ray irradiation

A ^{60}Co source (Gammacell 220 exell) a dose rate of 10 kGy/hr was used to expose the capacitors to gamma irradiation. The process for irradiating gamma ray was done at Office of Atoms for Peace. We used foam as a stage to mount the capacitors and put it in the middle of aluminum cylinder which is surrounded with gamma source (see Fig. 4.14). Red Perspex dosimeters were used to calibrate the gamma ray doses. For the details of Red Perspex dosimeters, it is kept the Institutes secrete. Figure 4.15 shows the Red Perspex dosimeters put near the capacitors.

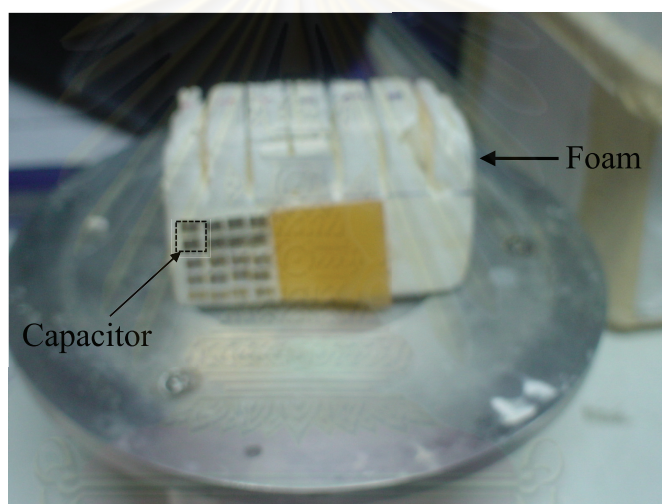


Figure 4.14: The photograph showing the capacitors mounted on foam sent them to gamma source.

Table 4.4 presents the doses of gamma ray using for irradiation.

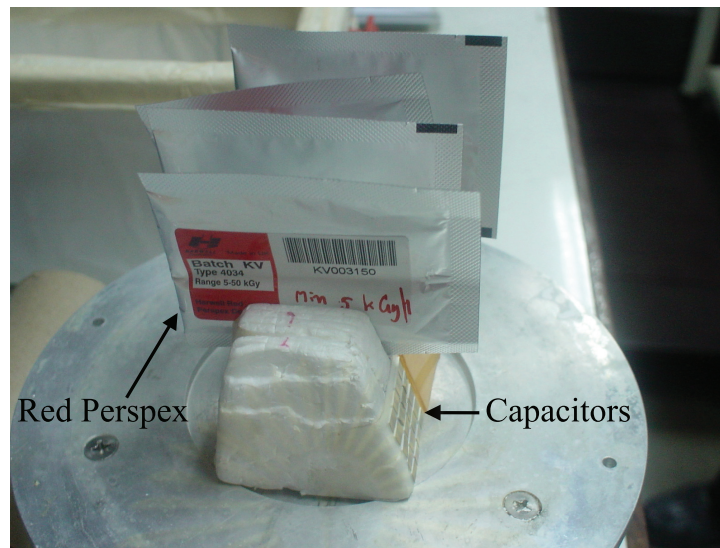


Figure 4.15: The photograph showing the Red Perspex used for calibrating the gamma ray doses.

Table 4.4: The doses of gamma ray using for irradiation.

Time (min)	Doses (kGy)	approximately doses (kGy)
35	4.82	5
71	10.57	10
213	28.64	30

4.7 Dielectric property measurement

In this thesis work, a commercial LF impedance analyzer (Model: HP 4192A) is utilized in dielectric property measurement. The obtained capacitance of the films from the impedance analyzer was converted to dielectric constant by using Farnell's analysis. The detail of conversion from capacitance to dielectric constant will be given in section 4.7.1. In this work, a ring resonator was used for capacitance measurement. However, in fact this ring resonator does not need for this work because the capacitance was measured in the low (rf) frequency range (10 kHz-1 MHz). Regularly, ring resonator was utilized for measuring the

capacitance in high frequency range of GHz. In high frequency measurement, two capacitors were connected microwave ports and the transmission measurement on the device was done by a network analyzer. The quality factor, Q , and resonant frequency, f_0 , of lowest mode which depend on ring resonator configuration such as diameter of ring [133] are used to calculate the capacitance and dissipation of the capacitors. The ring resonator used in this work was fabricated by Mark Dalberth [46] and Satreerat Hodak [47]. Figure 4.16 shows the schematic diagram of a ring resonator used in capacitance measurement. In my thesis work, only one capacitor was needed to do the experiment. The capacitor was put on a ring resonator and silver paint was pasted to link the capacitor and ring resonator (see Fig. 4.17). The ring resonator box was attached to the impedance analyzer as seen in Fig. 4.18. The impedance analyzer was interfaced with Labview software written by Mr.Surakarn Thitinan to measure the capacitance of the films. For using this program, the frequency range as well as frequency interval were put in the unite of kilohertz whereas the applied voltage was fixed. Before clicking at the run button, the “set” button was pressed to reset the new input frequency values. The output data can be obtained in .txt file.

In this study, the capacitance of the films was measured at room temperature as a function of frequency in the range of 10-1000 kHz as frequency interval was set at 10 kHz. The applied voltages were varied in -25 to 25 volt range.

ศูนย์วิทยทรัพยากร
จุฬาลงกรณ์มหาวิทยาลัย

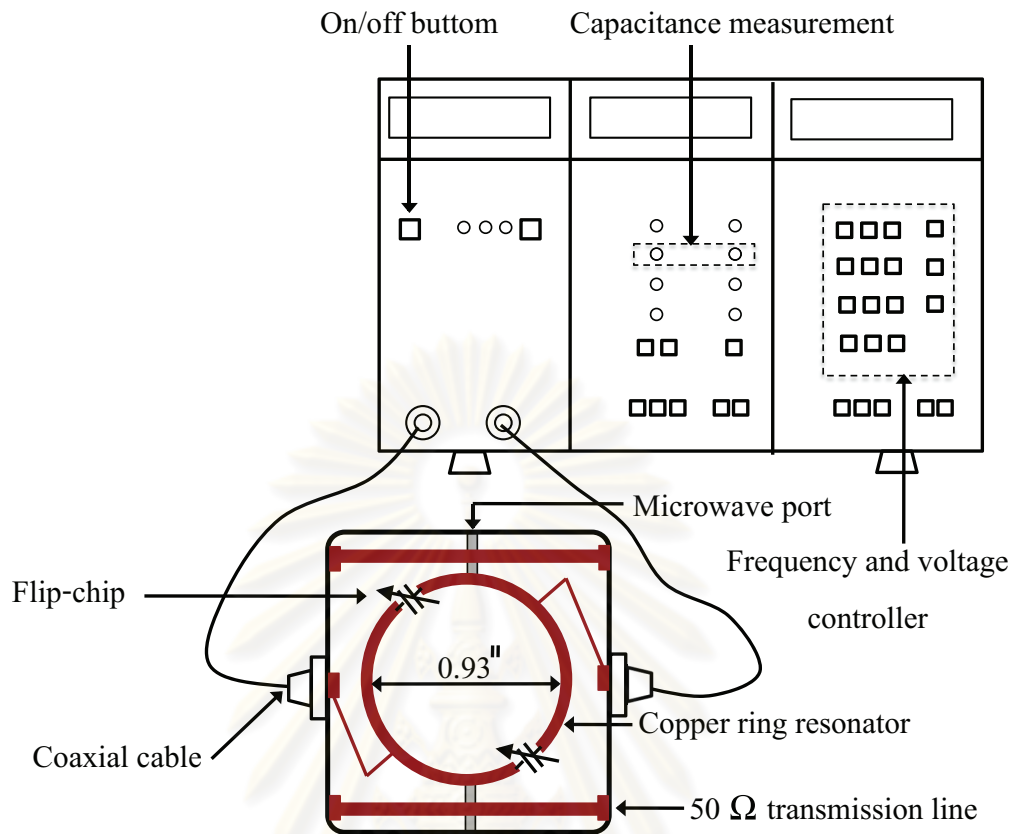


Figure 4.16: The schematic diagram of a ring resonator used in capacitance measurement. Flip chip presented as variable capacitors.

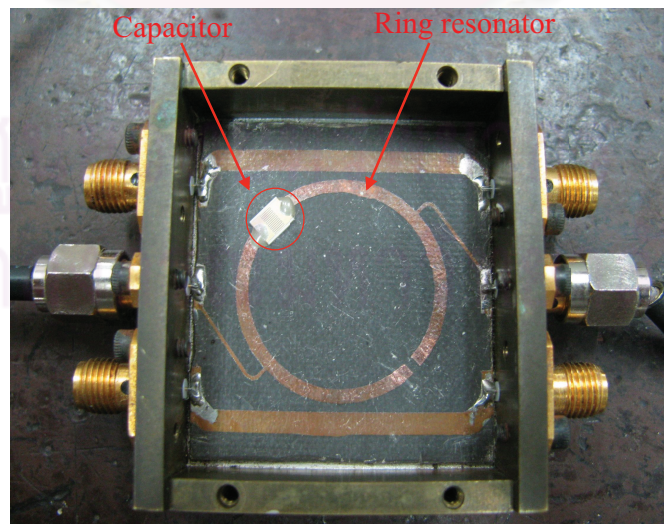


Figure 4.17: The image of interdigitated capacitor connected to a ring resonator.

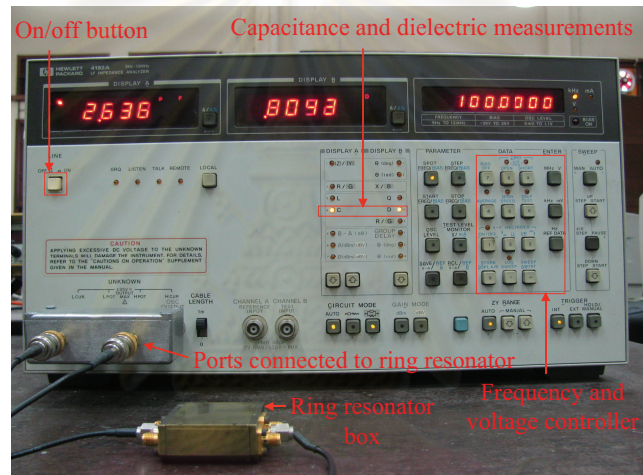


Figure 4.18: The photograph of LF impedance analyzer model HP 4192A connected to a ring resonator box.

ศูนย์วิทยทรัพยากร
จุฬาลงกรณ์มหาวิทยาลัย

4.7.1 Dielectric constant determination of interdigitated capacitor

In this work, dielectric constants of film capacitors having interdigitated electrode configuration were determined based on an analytical method derived by Farnell et al. [134]. Farnell's analysis can be applied under assumption that both film and substrate are insulating and the electrode configuration is interdigitated pattern. Farnell et al. used numerical simulations to calculate the dielectric constant of a simplified two-dimensional periodic interdigitated electrode. The semi empirical equation developed by Farnell et al. follows the expression:

$$\varepsilon_f = \varepsilon_s + \frac{C - K(1 + \varepsilon_s)}{K(1 - \exp(\frac{-4.6h}{G+W}))}, \quad (4.1)$$

where ε_f and ε_s are dielectric constant of the films and substrate, respectively. h is the thickness of the films. G and W are the spacing and width of figure, respectively. K is a constant value in unit pF depending on the area and gap of electrode, which is calculated by:

$$K = 6.5\left(\frac{G}{W+G}\right)^2 + 1.08\left(\frac{G}{W+G}\right) + 2.37. \quad (4.2)$$

The C value is approximately the capacitance per unit length, which is given by:

$$C = \frac{C_m}{LN}, \quad (4.3)$$

where C_m is the experimentally measured capacitance in unit pF. L is the overlapping figure length in unit m. N is the number of the spacing of figure. All parameters of interdigitated electrode structure used for calculating dielectric constant are depicted in Fig. 4.19.

In our experiment, $G = 100 \mu\text{m}$, $W = 100 \mu\text{m}$, thus $K = 4.535 \text{ pF}$, $L = 1500 \mu\text{m}$, $N = 14$ and the film thickness is approximately 600 nm .

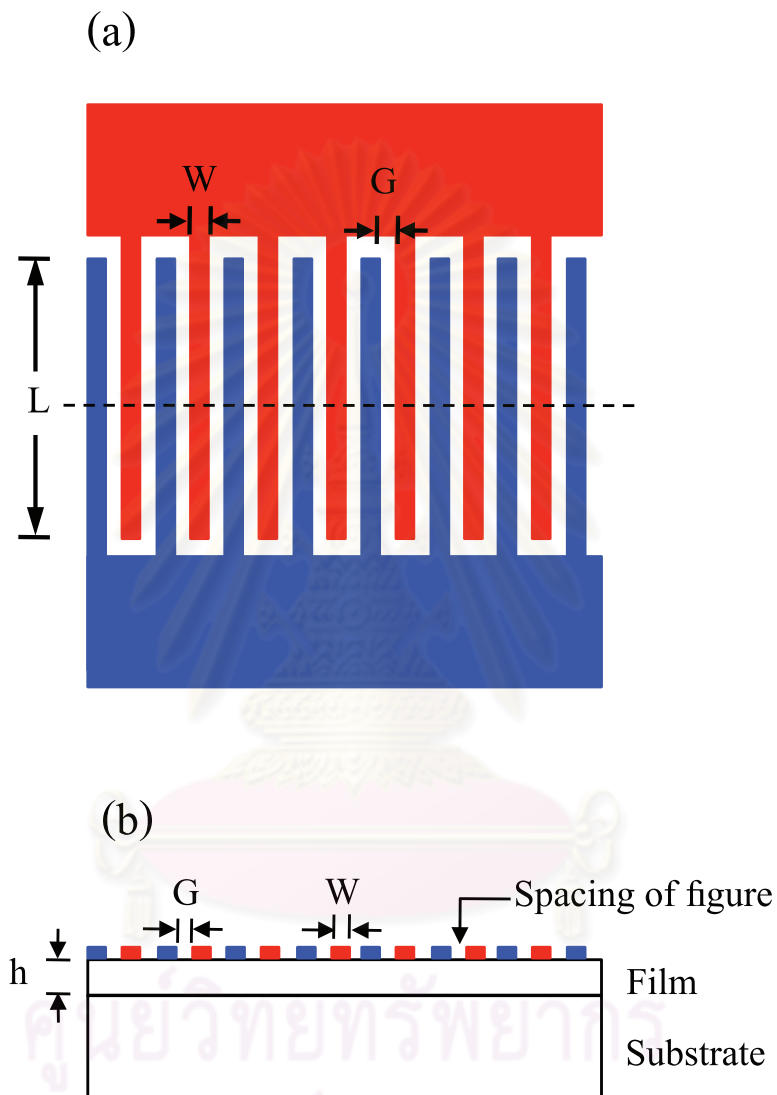


Figure 4.19: Schematic representation of (a) top view and (b) cross section of capacitor with interdigitated electrode structure showing all parameters for calculating dielectric constant of films.

CHAPTER V

RESULTS AND DISCUSSIONS

This chapter presents the results and discussion of all which are divided into three main parts. First, we will discuss the effect of annealing temperature on the structural properties, surface morphology and optical properties of the films. Second, the effect of Fe doping on structural properties, surface morphology as well as gas sensing properties of the films will be demonstrated. At the end, we will present the effect of multilayer films, Fe dopant and the effect of gamma ray irradiation on dielectric properties of the film. Moreover, the result of oxidation state of Fe in the films will be also illustrated.

5.1 Effect of annealing temperature on structural properties and surface morphology of SrTiO₃/BaTiO₃ films

XRD pattern of SrTiO₃/BaTiO₃ multilayer films deposited on ITO coated glass substrate as a function of the annealing temperature varied in the range of 300-650 °C is illustrated in Fig. 5.1. The XRD results exhibit that for the films annealed at lower temperature (300, 400, 500 and 550 °C), there are no characteristic diffraction peaks of both BaTiO₃ and SrTiO₃, whereas the films present distinct crystalline peaks at higher annealing temperature of 600 and 650 °C which is indicated the appearance of characteristic peaks of BaTiO₃ and SrTiO₃.

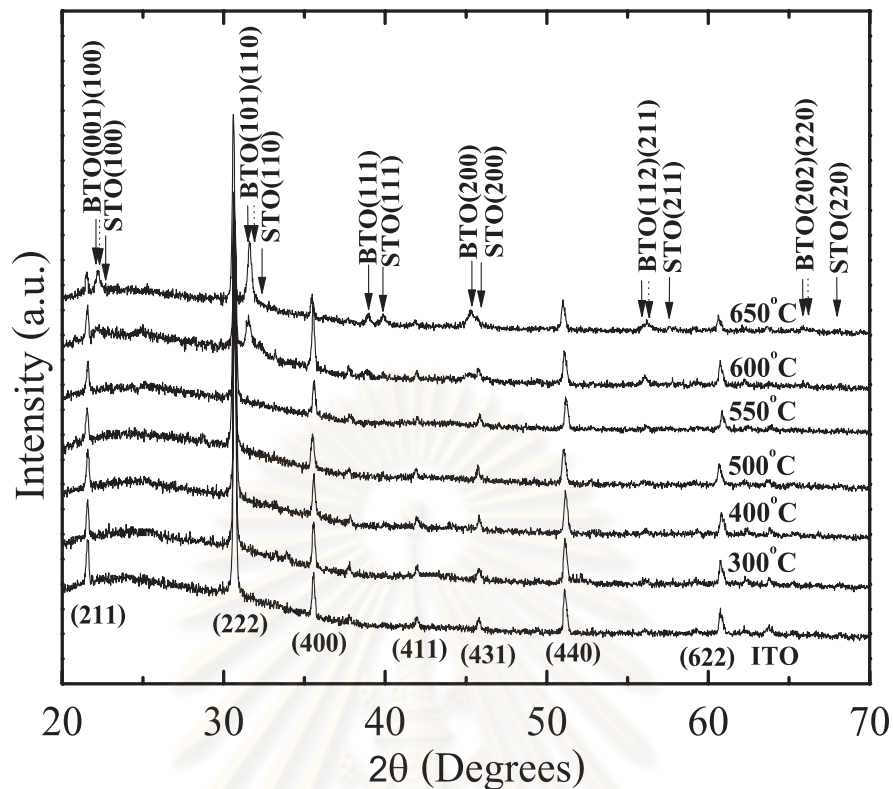


Figure 5.1: X-ray diffraction pattern of SrTiO₃/BaTiO₃ films annealed at different temperatures on ITO/glass.

We found that the peaks of XRD pattern are sharper and more intense with increasing annealing temperature. Previous work done by a senior student named Miss Supa Sirinam at Satreerat's laboratory has been studied the effect of annealing temperature on the crystal structure of the films [135]. Three types of films including BaTiO₃ and SrTiO₃ multilayer films as well as uniform BaTiO₃, SrTiO₃ films were grown on silicon substrate with different annealing temperatures of 300, 800 and 1000 °C. The films were prepared with the thickness of 150 nm. Figure 5.2 shows XRD pattern of BaTiO₃ and SrTiO₃ multilayer films annealed at 800 °C and Fig. 5.3 presents XRD pattern of uniform BaTiO₃ and SrTiO₃ films annealed at 1000 °C. She found that the films annealed at high temperature of 1000 °C exhibited the most intensity of BaTiO₃ and SrTiO₃ peaks of XRD pattern. For the films annealed at 800 °C, she also inverted the order of the film layer. STO/BTO 1:1 refers to the first layer done by BaTiO₃ solution and follows by SrTiO₃ solu-

tion in the second layer. BTO/STO 1:1 represents SrTiO₃ located in the bottom layer and BaTiO₃ located in the top layer. By comparing the XRD patterns of STO/BTO and BTO/STO films, they clearly found that the film located in the first layer showed higher and narrower peaks. This is due to the fact that the films located in the first layer was annealed for two times longer than that of the top film.

From their conclusion, the strongest intensity of XRD peaks for BaTiO₃ and SrTiO₃ was achieved from the films annealed at 1000 °C. Thus, in this thesis work, we chose the annealing temperature of 1000 °C for growing the multilayer films on alumina (Al₂O₃) substrate to investigate their gas sensing properties. We fixed the annealing temperature to 1000 °C, but Fe doping contents were varied. Figure 5.4 shows the XRD pattern of multilayer films deposited on Al₂O₃ substrate. The XRD characteristic peaks of BaTiO₃ and SrTiO₃ were also observed. The XRD results of the films grown on Al₂O₃ will be more discussed in section 5.4.



ศูนย์วิทยทรัพยากร
จุฬาลงกรณ์มหาวิทยาลัย

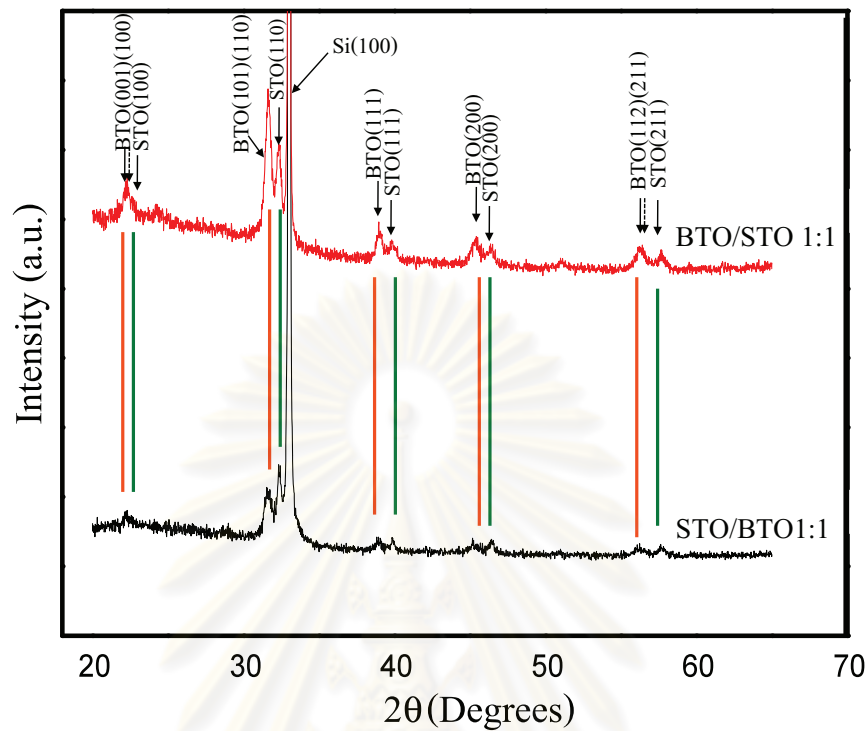


Figure 5.2: X-ray diffraction pattern of $\text{SrTiO}_3/\text{BaTiO}_3$ films on Si substrate annealed at temperatures of $800\text{ }^\circ\text{C}$.

For XRD results of the film deposited on ITO coated on glass substrate, the weak intensity of X-ray spectra of the films annealed at 600 and $650\text{ }^\circ\text{C}$ was observed suggesting that the films are not well crystallized. In addition, the full width at half maximum of the peaks decreases as the temperature increases. This results also agree with increased crystallinity of the films annealed at higher temperature. The average crystallite size (t) measured in a vertical direction to the surface of the sample was calculated using Scherrer's formula as expressed in equation 3.7. In this study, the most (111) plane of BaTiO_3 and SrTiO_3 has chosen to analysis average crystallite size due to no overlapping with ITO peak. The crystal sizes of BaTiO_3 and SrTiO_3 films annealed at $600\text{ }^\circ\text{C}$ are approximately 26 ± 5 nm and 14 ± 5 nm, respectively, whereas that for BaTiO_3 and SrTiO_3 annealed at

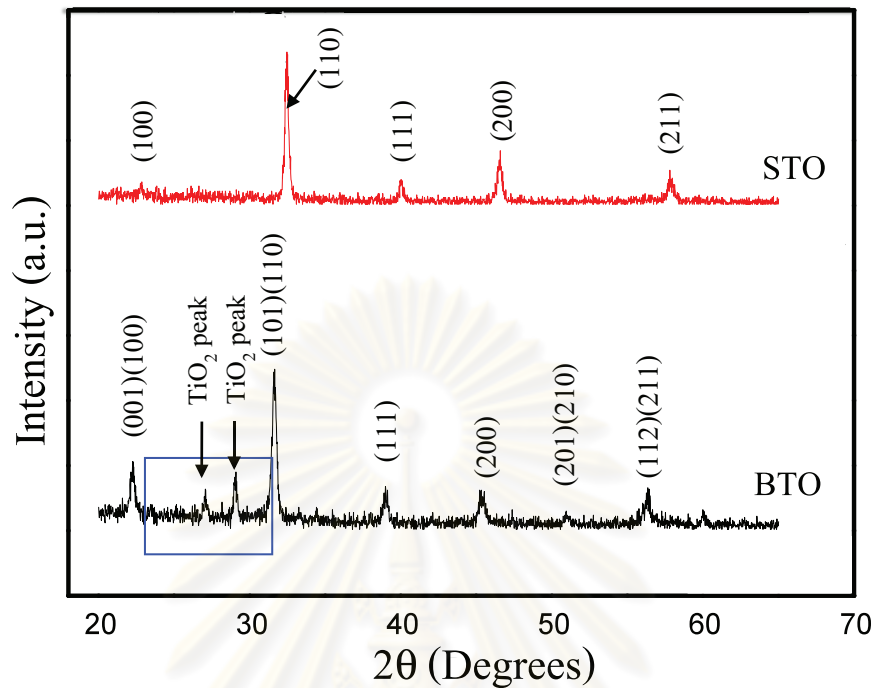


Figure 5.3: X-ray diffraction pattern of uniform BaTiO₃ and SrTiO₃ films on Si substrate annealed at temperatures of 1000 °C.

650 °C are about 44 ± 4 nm and 37 ± 4 nm, respectively. It has been clearly seen that the crystal size of the multilayer films increases with increasing annealing temperature. The average crystallite size of BaTiO₃ is slightly larger than that of SrTiO₃. This is because the first layer was done with BaTiO₃ solution which was annealed for two times longer than that of the top SrTiO₃.

The XRD pattern of the films annealed at 600 and 650 °C shows a separation of the BaTiO₃ peaks suggesting that BaTiO₃ transforms into tetragonal structure, while a splitting of SrTiO₃ peak did not observe indicating that SrTiO₃ is cubic structure. The lattice parameters of SrTiO₃ for cubic phase and BaTiO₃ for tetragonal phase were calculated using equation 3.2 and 3.3, respectively. The most intense BaTiO₃ (110) and another (111) were chosen for calculating that of BaTiO₃. For SrTiO₃, we have chosen (111) plane for calculating lattice parameter

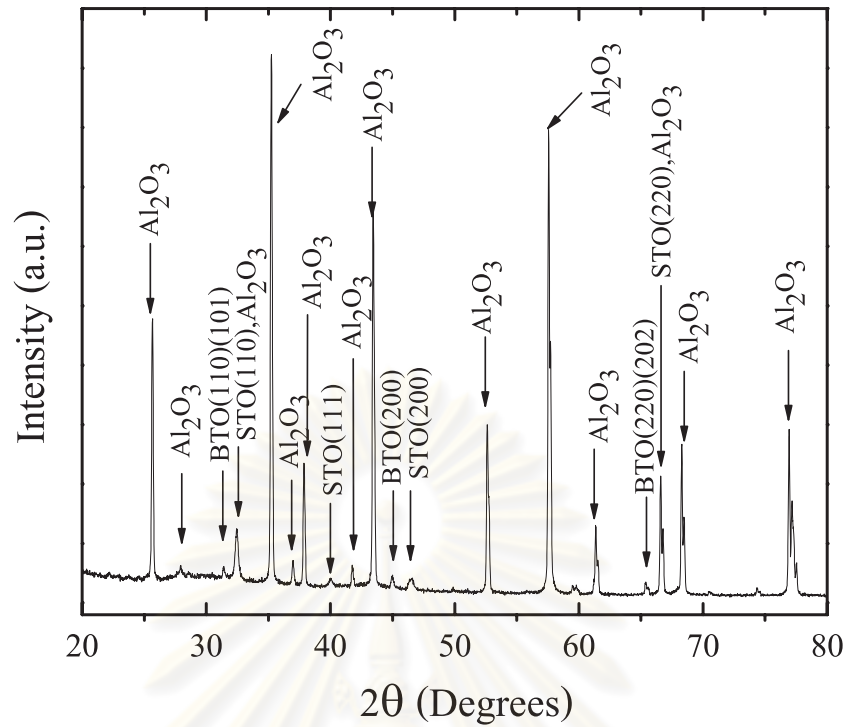


Figure 5.4: X-ray diffraction pattern of SrTiO₃/BaTiO₃ films on Al₂O₃ substrate annealed at temperatures of 100 °C.

due to its most intensity. Our calculated lattice parameter for BaTiO₃ were $a = 3.995 \pm 5 \text{ \AA}$ and $c = 4.011 \pm 5 \text{ \AA}$, while that for SrTiO₃ was found to be $3.905 \pm 5 \text{ \AA}$ which is close to the value of bulk BaTiO₃ and SrTiO₃ [56, 136]. All the films annealed at 600 and 650 °C showed the same XRD pattern and any phase transition did not observe. Figure 5.5 illustrates AFM images of SrTiO₃/BaTiO₃ films as a function of annealing temperature. We found that the grain size of the films also increases as annealing temperature increases reaching near 30 nm at the annealing temperature of 650 °C. In addition, AFM results for the films prepared by Miss Supa Sirinam confirmed that the grain size of the films increases with increasing annealing temperature. The grain size for multilayer films annealed at 800 °C was approximately 50 nm and it increased up to 100 nm as annealing temperature increased to 1000 °C. The increase in grain size with increasing annealing temperature was also observed in other literatures [77, 137]. This results can be explained that increasing temperature enhances atom mobility yield a more ef-

fective recrystallization of the material of the films leading to larger grain size.

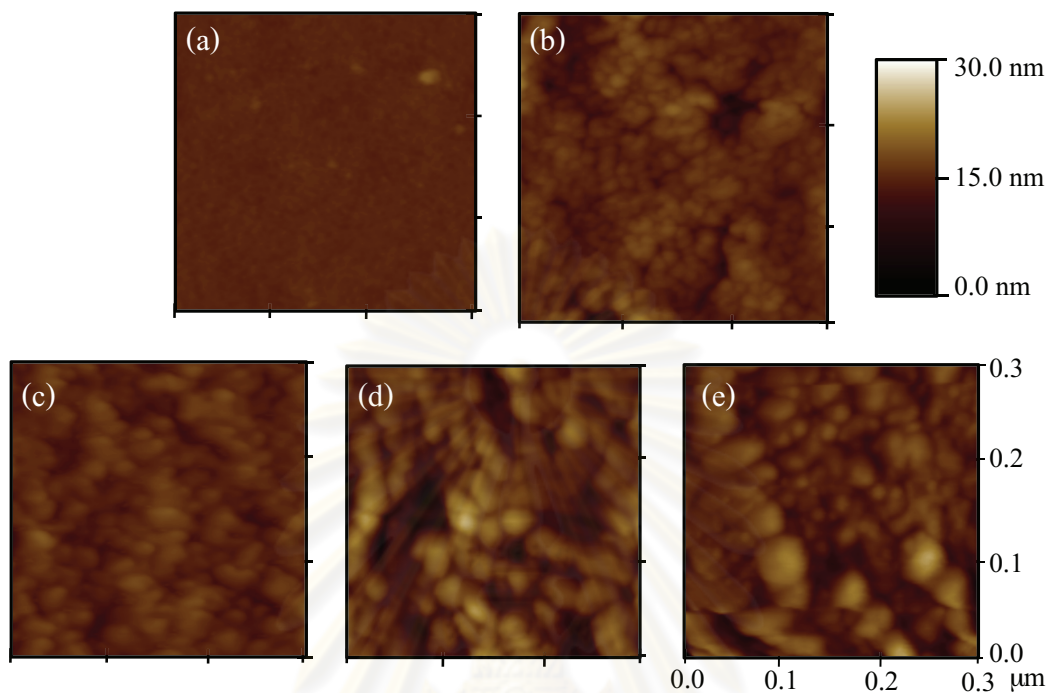


Figure 5.5: AFM images ($0.3 \mu\text{m} \times 0.3 \mu\text{m}$) of $\text{SrTiO}_3/\text{BaTiO}_3$ films deposited on ITO coated glass annealed at different temperatures (a) 300 °C, (b) 500 °C, (c) 550 °C, (d) 600 °C and (e) 650 °C.

ศูนย์วิทยทรัพยากร
จุฬาลงกรณ์มหาวิทยาลัย

5.2 Effect of annealing temperature on optical properties of SrTiO₃/BaTiO₃ films

The films deposited on ITO coated on a glass substrate were used for characterizing the effect of annealing temperature on their optical properties due to transparent property. In addition, such substrate is appropriate to transmission mode of UV-Vis spectroscope. Figure 5.6 shows the optical spectra of SrTiO₃/BaTiO₃ films on ITO coated on glass annealed at different temperatures in the 200-800 nm wavelength range. The insert in Fig. 5.6 shows the optical spectra of glass and ITO coated on glass substrate. We found that all the films annealed at high temperature were transparent and exhibited optical transmittance of near 85% in the visible region. The oscillations in the transmittance due to interference have low depths of modulation indicating inhomogeneity of the films across the light. All the films presented a sharp absorption onset in the near UV region.

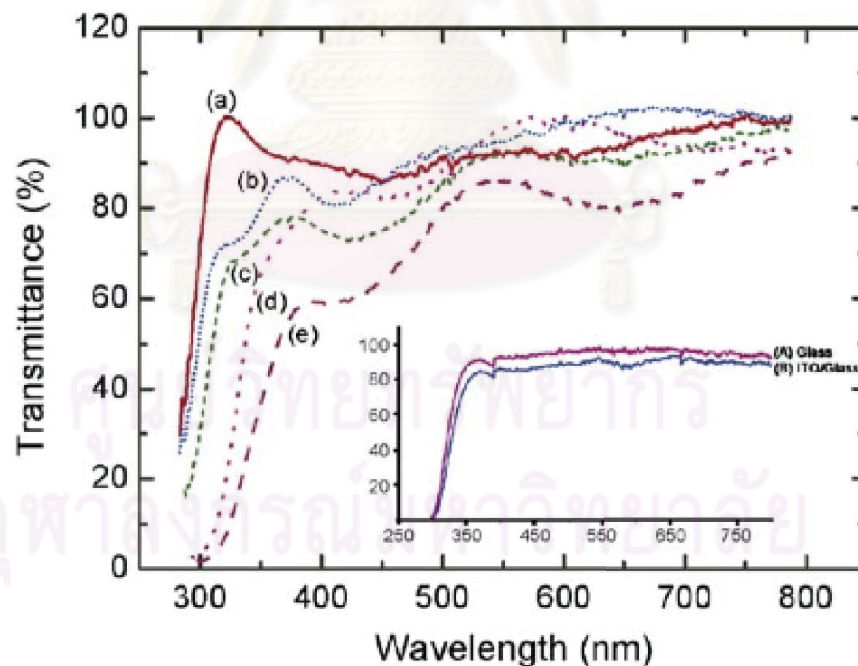


Figure 5.6: Transmittance spectra of SrTiO₃/BaTiO₃ films annealed at different temperatures (a) 300 °C, (b) 500 °C, (c) 550 °C, (d) 600 °C and (e) 650 °C.

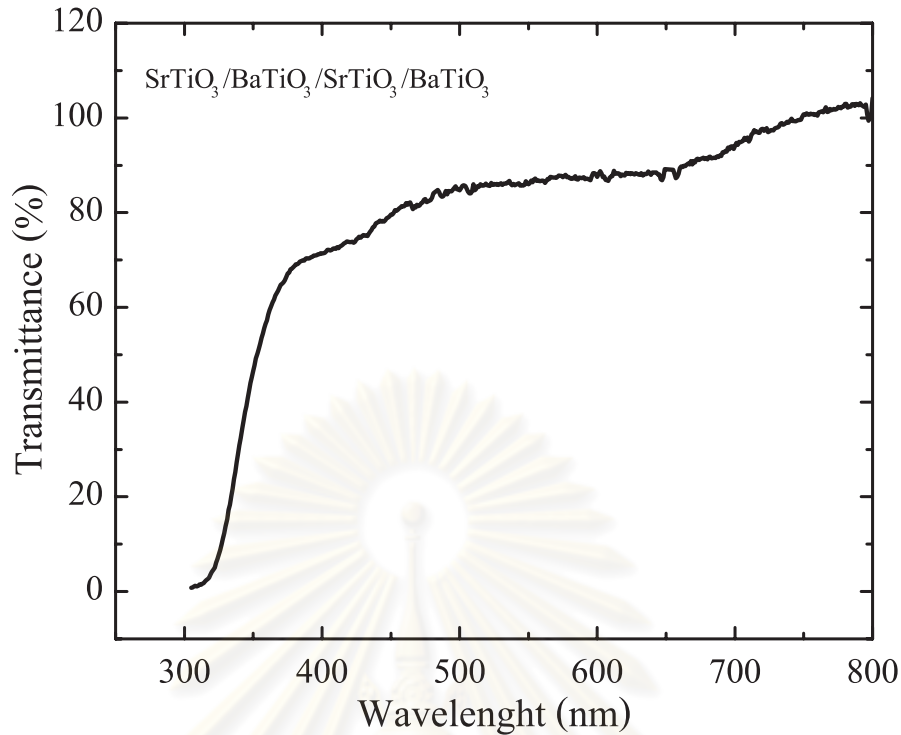


Figure 5.7: Transmittance spectra of $\text{SrTiO}_3/\text{BaTiO}_3/\text{SrTiO}_3/\text{BaTiO}_3$ films annealed at $600\text{ }^\circ\text{C}$.

Moreover, we deposited $\text{SrTiO}_3/\text{BaTiO}_3/\text{SrTiO}_3/\text{BaTiO}_3$ film (4 layers) on ITO coated on glass substrate. Figure 5.7 illustrates the optical spectra of $\text{SrTiO}_3/\text{BaTiO}_3/\text{SrTiO}_3/\text{BaTiO}_3$ film annealed at $600\text{ }^\circ\text{C}$. The transmission spectra of the multilayer film with 4 layers exhibited indistinct oscillation in transmission curve and lower depth of modulation compared with that of the films grown with 2 layers. This is due to the fact that the multilayer film with 4 layers has more film interfaces leading to weaker total interferences. Thus, in this study the $\text{SrTiO}_3/\text{BaTiO}_3/\text{SrTiO}_3/\text{BaTiO}_3$ film can not be a good candidate to examine the refractive index and extinction coefficient by using Swanepoels method. Nevertheless, work by Ornicha Kongwut and Assistant Professor Dr. Satreerat Hodak has been studied the optical properties of uniform BaTiO_3 with 4 layers annealed at $800\text{ }^\circ\text{C}$ as shown in Fig. 5.8 [67]. By comparison, the transmission spectra of uniform BaTiO_3 presented more depth of modulation compared with that of multilayer $\text{SrTiO}_3/\text{BaTiO}_3$ films with the same thickness.

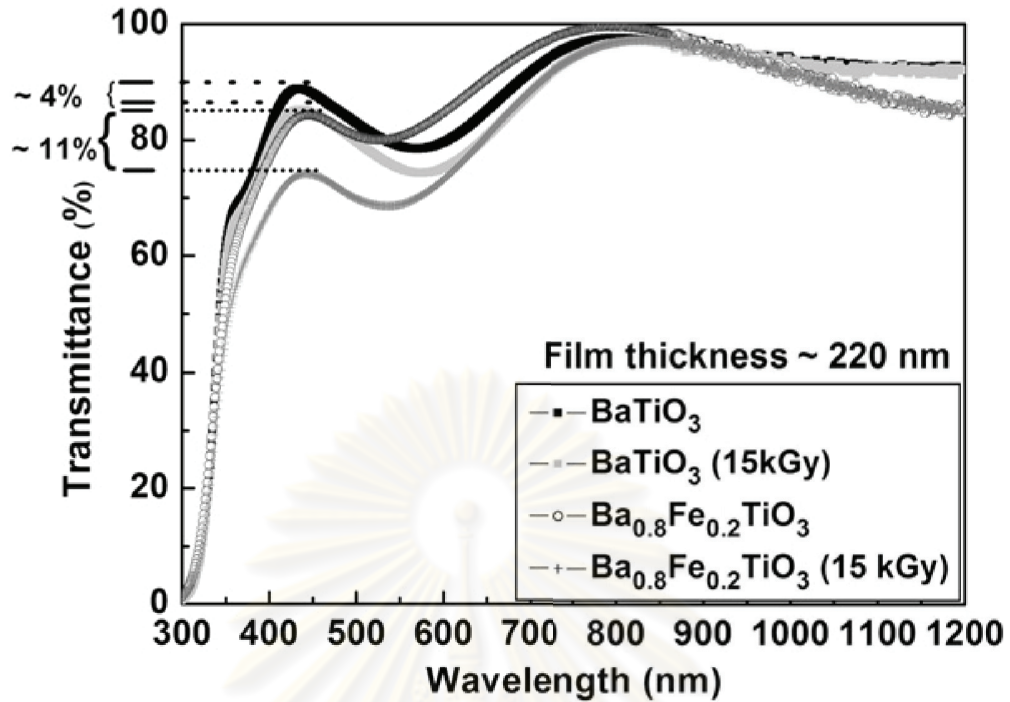


Figure 5.8: Transmittance spectra of BaTiO₃ and Ba_{0.8}Fe_{0.2}TiO₃ films before and after gamma irradiation at a dose of 15 kGy reported by Kongwut et al.

From the optical transmission spectra, the absorption coefficient (α) of the films was determined from equation 3.22. The absorption edge of the films shifts to higher wavelengths with increasing annealing temperature. This is due to exciton-phonon coupling or dynamic disorder which is the main factor contributing to absorption edge broadening for crystalline materials [138]. In amorphous materials, imperfections and disorder generating additional broadening due to static disorder. In the films of smallest grains change in Urbach-type absorption tail manifest the static inhomogeneity due to presence of localized states within the gap which can be quantified by the steepness of band edge [138]. The band edge steepness value can be obtained from the slope of the plot of α^2 and $h\nu$ at the beginning band-to-band absorption [139]. The band edge steepness of our films increased as the annealing temperature increased indicating that the density of localized state decreased with heating temperature. Another quantitative measurement of band edge characteristic can be derived from so-called Urbach rule illustrated in equation 3.23 [125]. The Urbach energy value ($E_U = (kT/\sigma)$) was

obtained by plotting $\ln \alpha$ versus $h\nu$ in band tail absorption region and taking inversely slope.

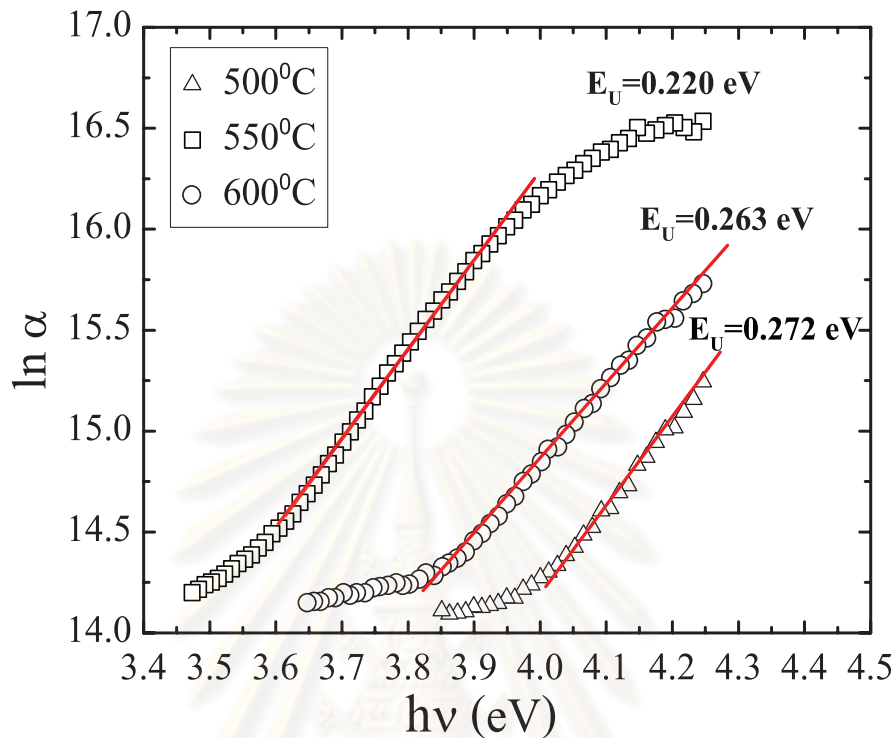


Figure 5.9: Determination of Urbach energy for SrTiO₃/BaTiO₃ films annealed at 500, 550 and 600 °C from the absorption coefficient.

Figure 5.9 demonstrates the plot of $\ln \alpha$ as a function of $h\nu$ for the films annealed at 500, 550 and 600 °C. The calculated Urbach energy was found to be 0.272, 0.263 and 0.220 eV for the films annealed at 500, 550 and 600 °C, respectively. As the annealing temperature increases, larger grains are formed which brings an increased band edge steepness. This may be due to the reduction of the surface to volume ratio as crystal grow larger since the localized states most likely from surface states. In order to determine energy gap of the films, the Tauc relation between the absorption coefficient and direct and indirect band gap energies (E_g) given in equation 3.20 and 3.21, respectively was used [124, 140]. We plotted $(\alpha h\nu)^n$ ($n=2$ for direct transition and $n=1/2$ indirect transition) versus $h\nu$. The energy gap was obtained by extrapolating the linear portion of the plot to zero frequency. We found that the best fit to a straight line was obtained for n

= 2 indicating that a direct allowed transition occurs at Γ point in the Brillouin zone from the valence band maximum to the conduction band minimum.

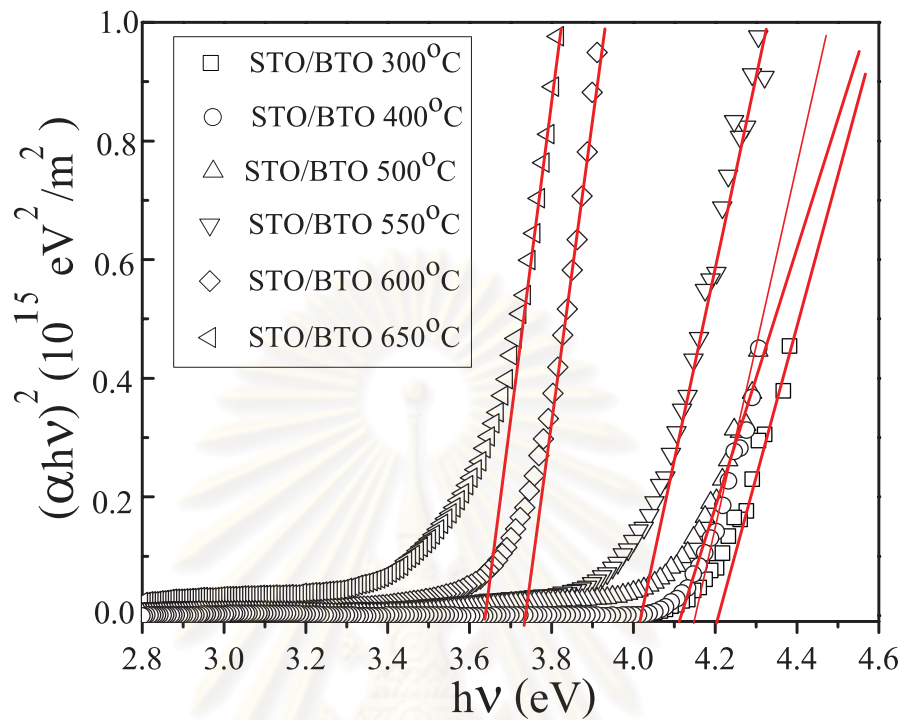


Figure 5.10: Plot of $(\alpha h\nu)^2$ versus $h\nu$ for $\text{SrTiO}_3/\text{BaTiO}_3$ films annealed at various temperatures.

Figure 5.10 shows the plot of $(\alpha h\nu)^2$ versus $h\nu$ at various annealing temperatures. The same absorption region has been used to evaluate optical band gap [141, 142]. The band gap energy as a function of annealing temperature is illustrated in Fig. 5.11. We found that the value of energy gap for the films annealed at lower temperature (300, 400, 500 and 550 °C) gradually decreases with increasing annealing temperature which is in the range of 4.19-4.03 eV. An abruptly decrease towards the bulk band gap value is observed for the films annealed above 600 °C yielding the energy gap value in the 3.64-3.74 eV range. It has been reported that the experimental direct and indirect band gap energies for BaTiO_3 are 3.6 and 3.2 eV, respectively [143], whereas those for SrTiO_3 are 3.75 and 3.25 eV, respectively [144, 145]. The band gap of the amorphous phase is about 0.3-0.5 eV larger than that of the crystalline phase [143, 144, 145]. The abrupt decrease of energy gap

from around 4 to 3.74 eV is due to obtaining a more crystalline phase when the films annealed above 600 °C. Similar change in energy gap for BaTiO₃ and SrTiO₃ has been observed in work by Zhang et al. and Bao et al. [77, 81].

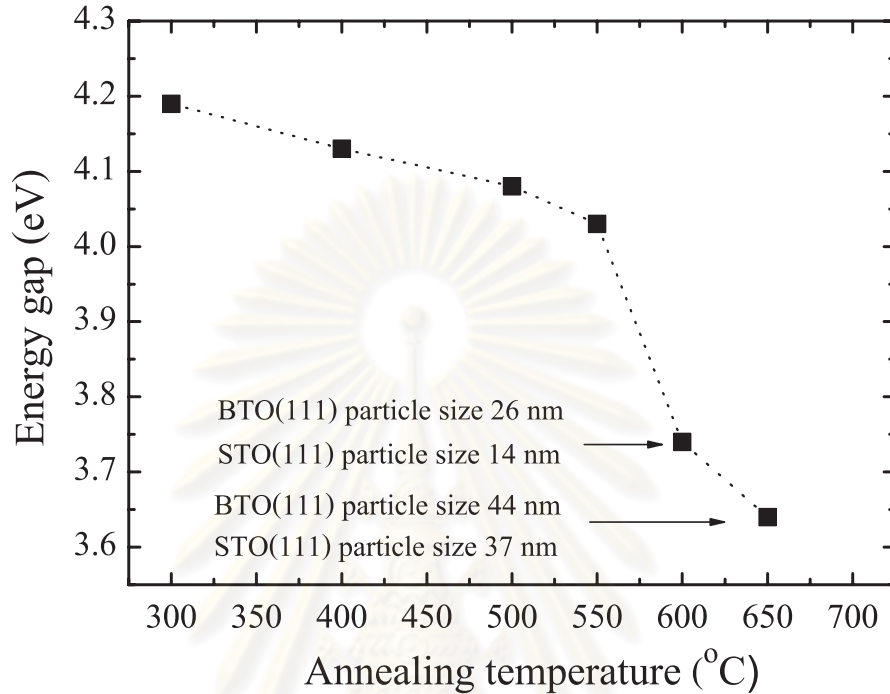


Figure 5.11: Temperature dependence of the optical band gap energy for SrTiO₃/BaTiO₃ films.

The crystallinity and the grain size of the films increase with increasing annealing temperature resulting in a decrease of energy band gap. The shift of optical band gap energy can be also explained in terms of quantum-size effect in which the films with large crystallites will have red-shifted absorption onsets. By way of comparison, we used the quantum confinement prediction for energy gap [146];

$$E_g(r) = E_g(\text{bulk}) + \frac{2\pi^2\hbar^2}{r^2} \left(\frac{1}{|m_e|} + \frac{1}{|m_h|} \right) \quad (5.1)$$

$$E_g(r) = E_g(\text{bulk}) + \frac{2\pi^2\hbar^2}{r^2\mu} \quad (5.2)$$

where, m_e , m_h , μ and r are the effective mass of electron, the effective mass of hole, the reduce mass and the diameter of nanoparticle, respectively. Normally, if the particle size is smaller than the corresponding DeBroglie wavelength, the size quantization effects can be observed in the band gap. The theoretical calculated DeBroglie wavelength (a_B) for BaTiO_3 and SrTiO_3 is about 15 nm obtained by calculating from below equation;

$$a_B = \frac{4\pi\varepsilon_0\varepsilon_r\hbar^2}{\mu e^2} \quad (5.3)$$

where ε_r is the dielectric constant, e is elementary charge (1.6×10^{-19} C) and $\hbar = h/2\pi$.

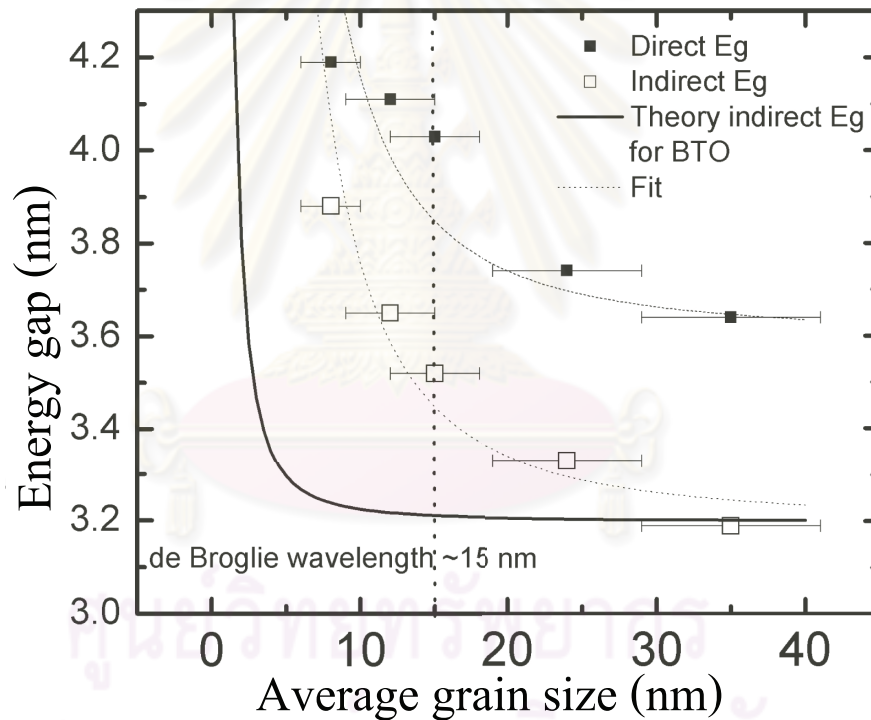


Figure 5.12: Direct and indirect band gap energies versus the average particle size. The solid line is prediction by quantum size effect. The dashed lines are the prediction of the quantum size effect with adjustable effective mass.

Figure 5.12 shows a comparison of theory of quantum confinement model along with the experiment values for the allowed direct and phonon assisted in-

direct transitions. In our calculation for BaTiO₃, we substituted m_e for $0.81m_o$ ($\Gamma \rightarrow R$ direction), here m_o is the mass of a free electron equal to 9.11×10^{-31} kg and m_h for $-2.78m_o$ ($R \rightarrow X$ direction) for indirect transitions. ($\mu = 0.62m_o$ assuming the light electron and hole) [146, 147]. The resulting values of direct band gap energies are larger than those of indirect band gap energies. As the particle size gets larger, the band gap energies approach the bulk values. For smaller crystallite size, there is a shift in band gap from the theoretical curve for both transitions. This is due to the values for the effective mass of electron and the effective mass of hole used in our calculation were obtained from bulk assumption using the first principle calculation [147]. A better agreement between our data and the theory can be obtained by adjusting the reduced mass. Such procedure leads to a reduced mass of $\mu=0.03m_o$ which would be consistent with band curvatures that are significantly larger than the bulk predictions. It has been noted that the band discontinuities are not true infinite potential barriers which softens the confinement of the carriers and may also cause a deviation between the theory and our data. The shift of the energy band gap to the higher energies with decreasing in particle size is caused by destruction of the excitons [148].

We now turn our attention to optical absorption. The optical parameters including refractive index (n), extinction coefficient (k) as well as films thickness (d) can be obtained from the optical transmission spectra using the envelope method derived by Swanepoel [121]. The calculated thickness of the films was found to be 250 ± 20 nm determining from the equation 3.19 which is content with the film thickness acquiring from scanning electron microscope. The absorption of our films was sharp near UV region but not in visible region. In the region of medium and weak absorption ($\alpha \neq 0$), the complex refractive index ($\tilde{n} = n - ik$, where n is the refractive index and k is the extinction coefficient) can be obtained using equation 3.13, 3.14, 3.15 and 3.16. Figure 5.13 presents the variation of the dispersion curve of the films with annealing temperature. The refractive index and the extinction coefficient decrease with the wavelength following a typical shape of dispersion curve near an electronic interband transition, rising rapidly

toward shorter wavelength [149]. We found that the refractive index increases with increasing annealing temperature. It is known that the refractive index of perovskite thin films is proportional to their electronic polarization per unit volume which is inversely proportional to distance between atomic planes. This result can be explained by an increase in the density of the film due to better packing and increased crystallinity as well as more homogeneity that light can be easily through the material of the films compared with the films annealed at lower temperature. The large increase in refractive index and strain relaxation following crystallization obtained for the films annealed at temperature 650 °C is due to crystallization of the perovskite phase. For comparison with bulk STO ($n = 2.30-2.65$) [144] and BTO ($n \sim 2.3$) [150] or well crystallized STO ($n = 2.15-2.35$) [123] and BTO thin films ($n = 2.15-2.55$) [122], the refractive index of our films is lower which is in the range of 1.69-2.10 depending on annealing temperature. This suggests that crystalline structure of our multilayer films leads to a relatively low density [144, 150, 123, 122]. The extinction coefficient of our films is less than 0.05 in the 450-750 nm wavelength range indicating low optical losses with the film annealed at 650 °C exhibiting the lowest loss.

ศูนย์วิทยทรัพยากร
จุฬาลงกรณ์มหาวิทยาลัย

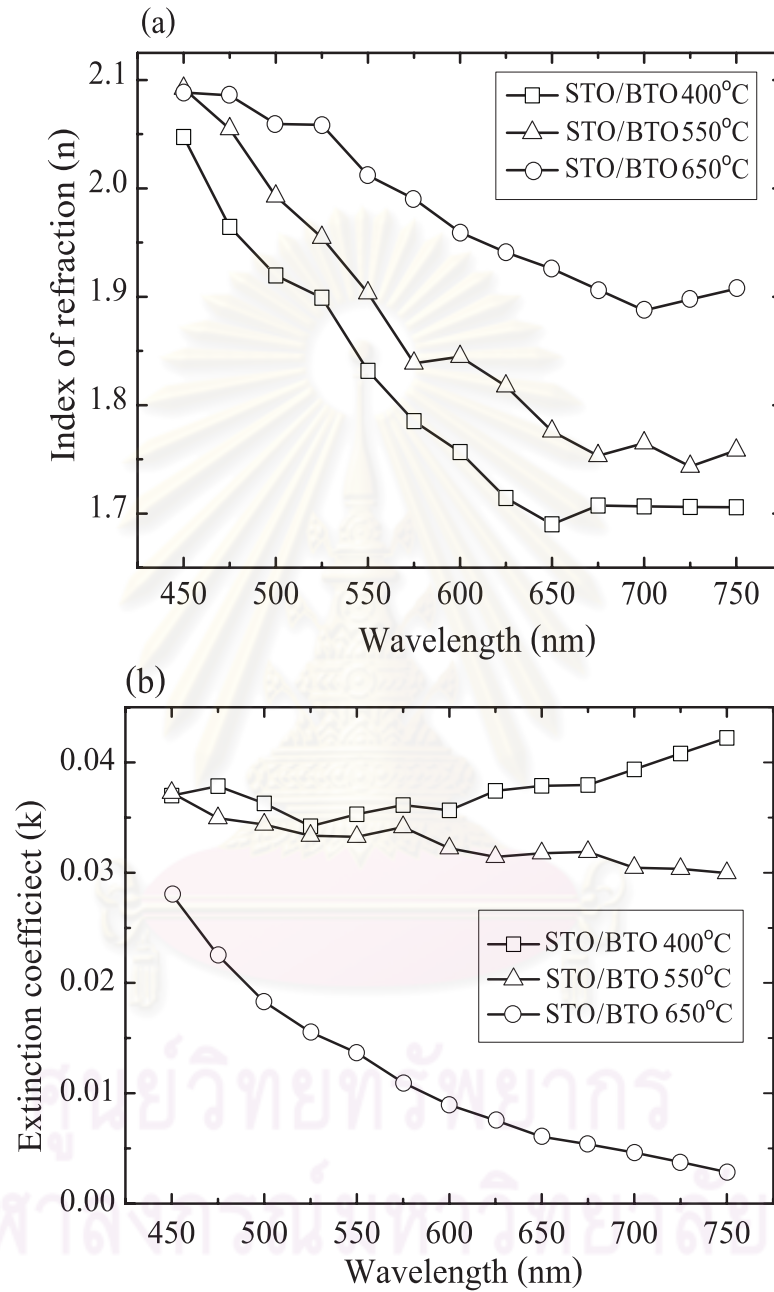


Figure 5.13: The variation of (a) refractive index, n and (b) extinction coefficient, k of the films as a function of wavelength.

5.3 Oxidation state and weight percentage of Fe in SrTiO₃/BaTiO₃ films

To verify a presence of the Fe in doped films as well as identify the oxidation state of Fe, the X-ray absorption near edge structure (XANES) technique and EDS equipped with field emission scanning electron microscopy are necessary to be used first for characterizing Fe-doped films. At first, we planed to add Fe with concentrations of 3, 5 and 10 wt% for BaTiO₃ and SrTiO₃. The detail of calculating weight percentages of Fe is given in Appendix B. Nevertheless, the quantity of Fe contents in the films obtained from EDS experiment is smaller than that obtained from calculation. The weight and atomic percentages of Fe in BaTi_{1-x}Fe_xO₃ and SrTi_{1-x}Fe_xO₃ obtained from EDS are illustrated in Table 5.1 and 5.2, respectively.

Table 5.1: Weight and atomic percentage of Fe in BaTi_{1-x}Fe_xO₃ films

	Weight percentage		Atomic percentage		x
	Ti	Fe	Ti	Fe	
2 wt% Fe-doped films	45.759	2.187	0.956	0.039	0.039
4 wt% Fe-doped films	44.275	4.227	0.925	0.076	0.076
8 wt% Fe-doped films	39.882	8.137	0.840	0.146	0.146

Table 5.2: Weight and atomic percentage of Fe in SrTi_{1-x}Fe_xO₃ films

	Weight percentage		Atomic percentage		x
	Ti	Fe	Ti	Fe	
2 wt% Fe-doped films	45.563	2.002	0.952	0.036	0.036
4 wt% Fe-doped films	44.390	4.197	0.927	0.075	0.075
8 wt% Fe-doped films	41.086	8.320	0.858	0.149	0.149

Figure 5.14(a) demonstrates the XANES spectra of Fe-doped films at Fe K-edge. Figure 5.14(b) shows an expanded pre-edge region of Fe-doped films with various Fe contents. All films have exhibited a small absorption peak at pre-edge region approximately 7114.5 eV which is similar to the value reported for that of Fe³⁺ in other works [151]. The pre-edge peak of XANES spectra is associated with the transition from deep 1s state to the quasi-bound state with 3d state. As expected, the intensity of pre-edge peak gradually increases with the increasing Fe doping concentrations. In the same way, the intensity of the main peak also increases as Fe doping contents increases. The absorption edge was obtained by derivative of the XANES spectra after subtracting pre-edge baseline. We found that the absorption edge energy of Fe in the films was found to be about 7121 eV, indicating a Fe³⁺ (0.64 Å) oxidation state.



ศูนย์วิทยทรัพยากร
จุฬาลงกรณ์มหาวิทยาลัย

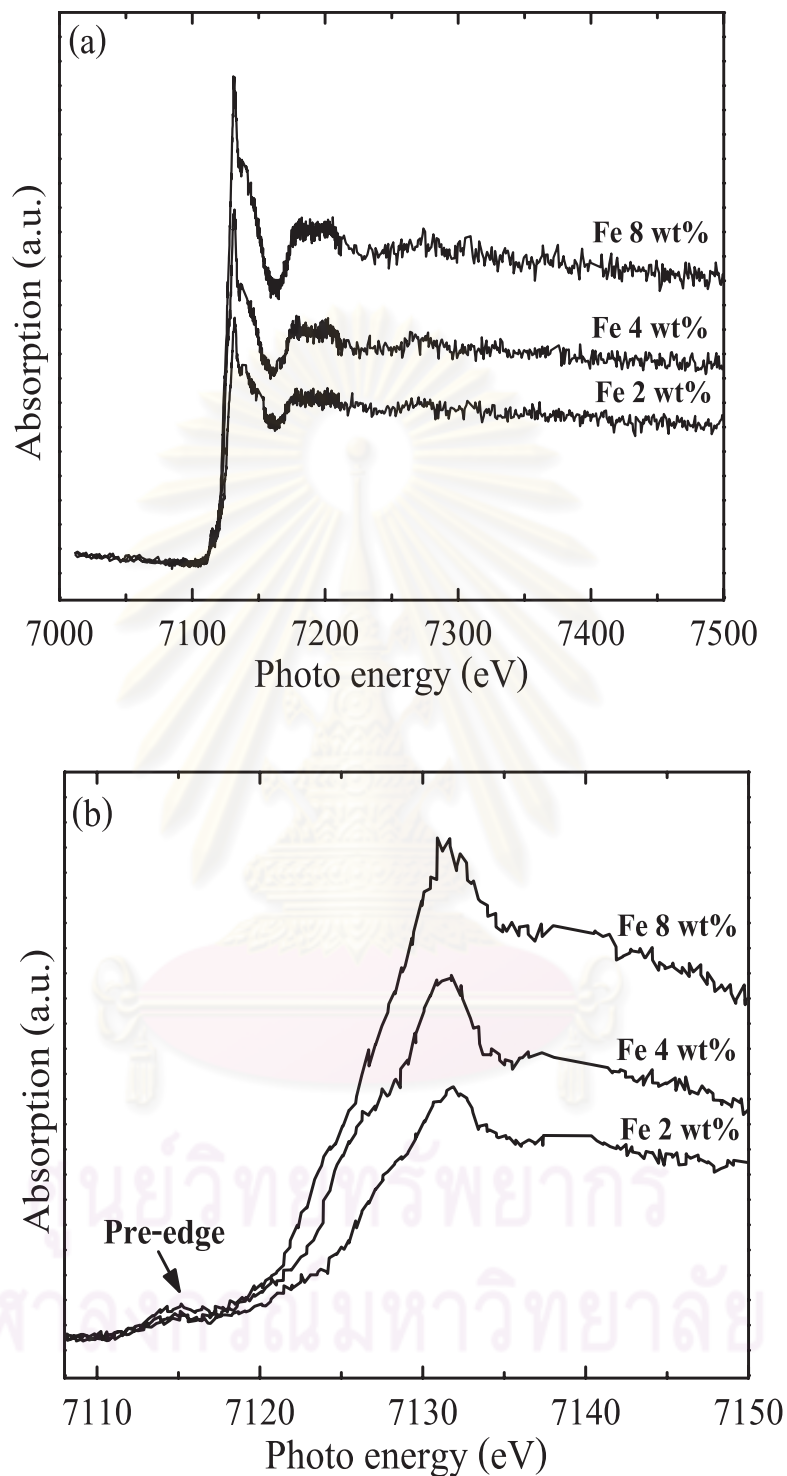


Figure 5.14: (a) Fe K-edge XANES spectra of Fe-doped SrTiO₃/BaTiO₃ multilayer films with various Fe concentrations (b) pre-edge and absorption regions.

5.4 Effect of Fe doping on structural properties and surface morphology of SrTiO₃/BaTiO₃ films

Figure 5.15 shows the XRD pattern of Fe-doped SrTiO₃/BaTiO₃ multilayer films with different Fe concentrations deposited on alumina substrate. Both undoped and Fe-doped films were crystalline and no preferred orientation was observed as illustrated in Fig. 5.15(a). Because of no overlapping between peak of 200 planes of the films and Al₂O₃ substrate, these two peaks were chosen to characterize the effect of Fe doping on lattice parameter of the films. The position of these two peaks gradually shifted to higher diffraction angles with increasing Fe doping concentration as shown in Fig. 5.15(b). This implies that the lattice parameter decreases as Fe concentrations increase. The calculated lattice parameter for undoped SrTiO₃ with cubic structure was 3.902 Å whereas for Fe-doped SrTiO₃ decreased as the Fe content in the film increased (Fe-doped SrTiO₃: 3.900 Å for Fe 2 wt%, 3.894 Å for Fe 4 wt% and 3.884 Å for Fe 8 wt%). We found similar reduction in the lattice parameter of Fe-doped BaTiO₃ (undoped BaTiO₃: 4.009 Å, Fe-doped BaTiO₃: 4.008 Å for Fe 2 wt%, 4.003 Å for Fe 4 wt% and 4.000 Å for Fe 8 wt%). We expected that the Fe ion substitution into Ti⁴⁺ (0.68 Å) due to the compatible radius. The weight percentage of Fe in the film was confirmed with EDS results. Moreover, the full width at half maximum of the peaks also increases as Fe doping concentrations increase. This implies that the crystalline size of the films decreases with more Fe content in the films which was confirmed using FESEM.

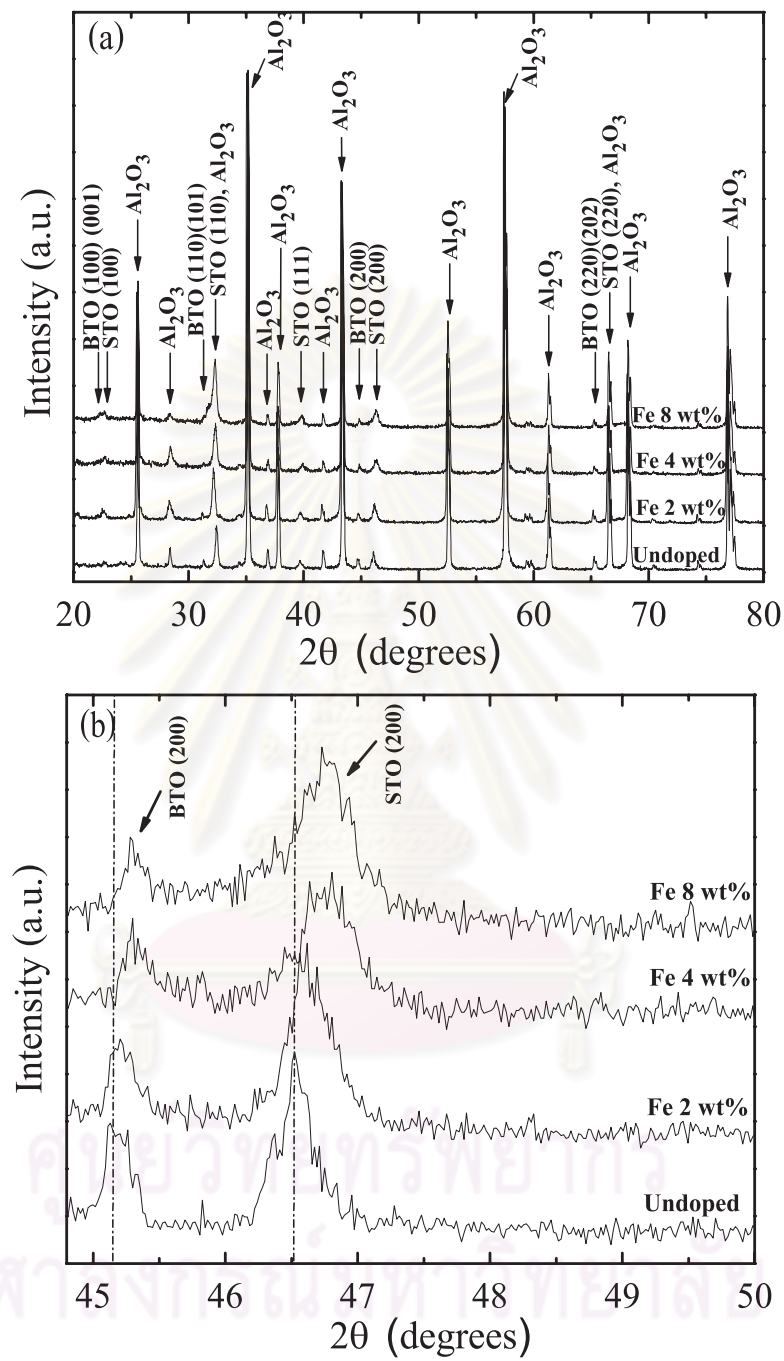


Figure 5.15: (a) X-ray diffraction patterns of Fe-doped SrTiO₃/BaTiO₃ multilayer films with different Fe concentrations deposited on alumina substrate, (b) the zoom of (200) planes.

Figure 5.16 illustrates the FESEM images of the films with various concentrations of Fe dopant. The FESEM results obviously reveal a distinguishable surface morphology between undoped and Fe-doped films. In other words, the undoped films have a mixture of round and facet-shaped morphology while the surface of Fe-doped films has a tendency towards porous structure as the contents of Fe in the films increase. Fe dopant causes the decrease of facet-shaped morphologies and connection of grain boundaries. The grain size of the films strongly depends on Fe doping contents. We found that the average size of particle decreases from 300 nm for undoped films to 200, 100 and 70 nm with the Fe doping concentrations of 2 wt%, 4 wt% and 8 wt%, respectively.

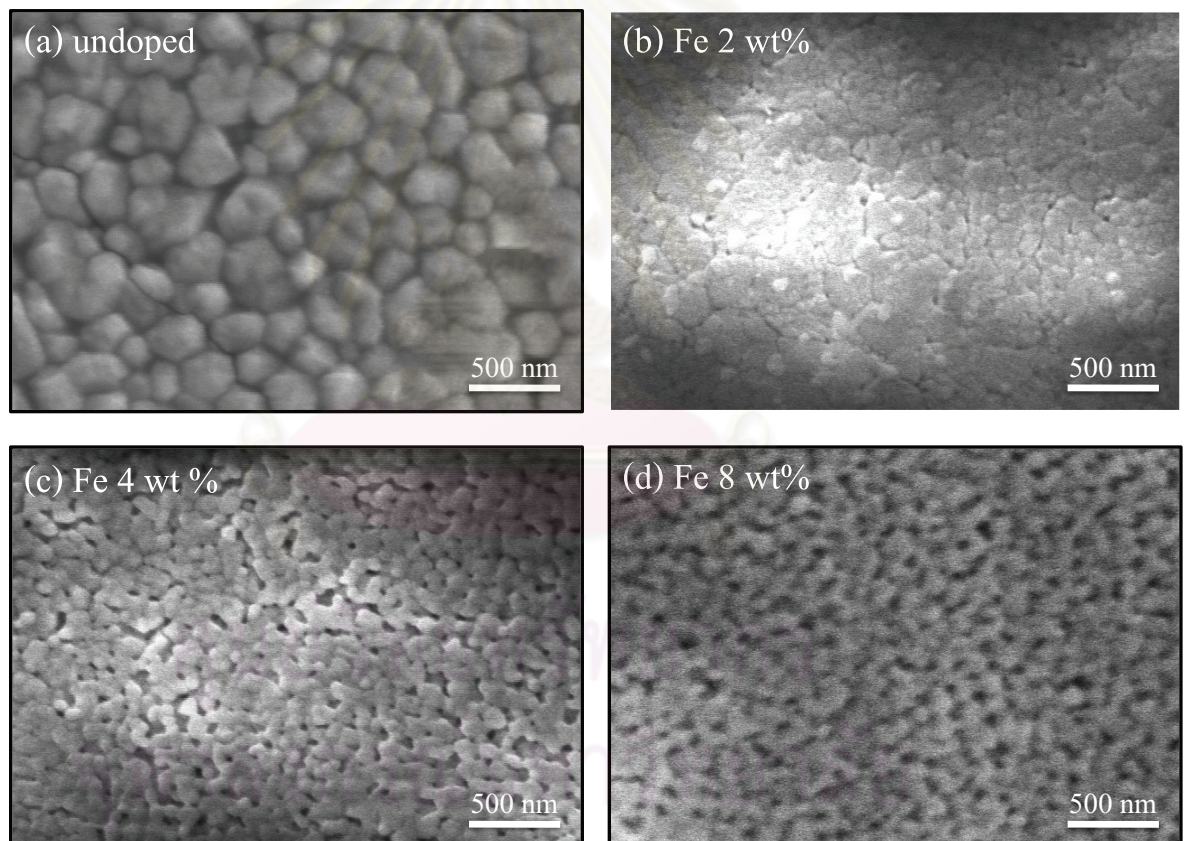


Figure 5.16: FESEM images with magnification of 50,000 of $\text{SrTiO}_3/\text{BaTiO}_3$ multilayer films deposited on alumina substrate (a) undoped, (b) 2 wt%, (c) 4 wt% and (d) 8wt% Fe doping concentrations.

The decrease in the average size may be due to the fact that the particle surface of the $\text{SrTiO}_3/\text{BaTiO}_3$ films was wrapped by Fe ion which obstructs the crystal growth. Our results on reduction in grain size with increasing Fe concentrations are consistent with others [152, 153]. Figure 5.17 shows the cross-section FESEM of the film doped with Fe 2 wt% presenting clear interfaces between the film surface/alumina substrate and the film/the gold electrode. The film thickness is approximately 600 nm.

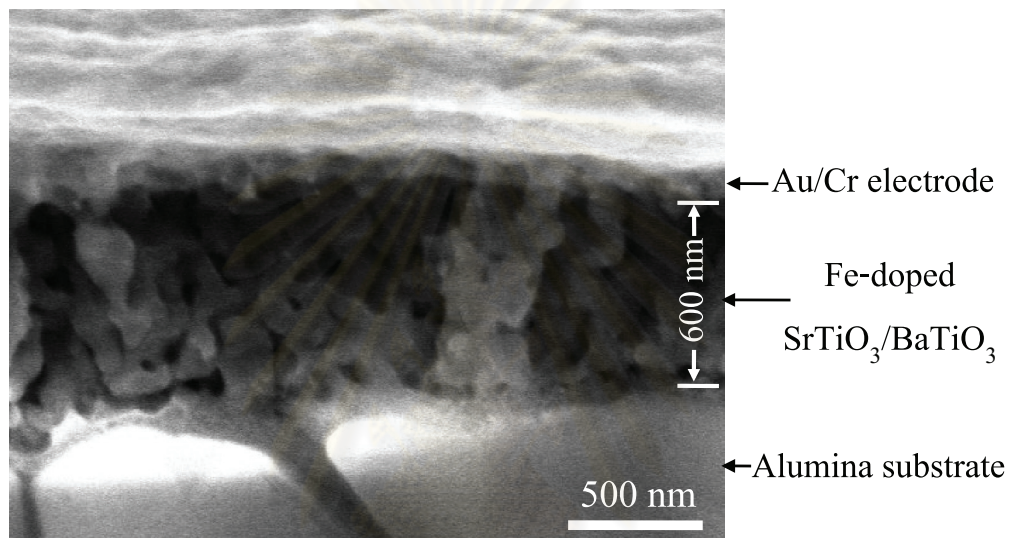


Figure 5.17: Cross-section FESEM images of a device made from 2 wt% Fe-doped $\text{SrTiO}_3/\text{BaTiO}_3$ multilayer films deposited on alumina substrate.

ศูนย์วิทยทรัพยากร
จุฬาลงกรณ์มหาวิทยาลัย

5.5 Effect of Fe doping on gas sensing properties of SrTiO₃/BaTiO₃ films

We have chosen 2 wt% and 8 wt% Fe-doped SrTiO₃/BaTiO₃ multilayer films to study the ethanol sensing ability of our films. Figure 5.18(a)-(d) show the dynamic response to ethanol pulses with concentration ranging from 100 to 1000 ppm of SrTiO₃/BaTiO₃ multilayer films doped with Fe 2 wt% and Fe 8 wt%, respectively. The gas sensing properties are based on the changes in resistance of the films which is caused by the adsorption and desorption of oxygen molecule from the grain surface. More details for gas sensing mechanism were mentioned in section 2.6.1. The number of oxygens which was absorbed on the films surface depend upon the particle size, large specific area of the material and operating temperature [24, 19]. Under air atmosphere, oxygen molecule were absorbed onto the films surface trapping electron and generating various oxygen ion species (O₂⁻, O⁻ and O²⁻). After exposing to ethanol which is a reducing gas, the resistance of our films undergoes due to increasing in electron concentrations near the film surface which suggest that the film is a p-type semiconductor.

In this experimental setup, the time scale of ethanol removal before the next ethanol feeding was 15 min. It was difficult to determine the recovery time of the sensors made from the films doped with Fe 2 wt% operating at 350 °C because the resistance did not come back to 90% of the initial value after removal of ethanol vapor (see Fig. 2.13). However, we have tried to extend ethanol removal time up to 30 min, the resistance did not still come back to nearby 90% of the initial value. Some researchers have observed the same behavior [24, 154]. Ling et al. found that the resistance of ZnO sensor operating at 300 °C turned to about 70 % of initial value after removal NO₃ for 100 min [154]. Work by Hongstith et al. have been observed that the ZnO sensor resistance could come back closing to the initial value as the operating temperature increased. Their results showed that at operating temperature of 220 °C, the resistance turned to around 70% of initial value after removal ethanol gas for 18 minute whereas operating temperature

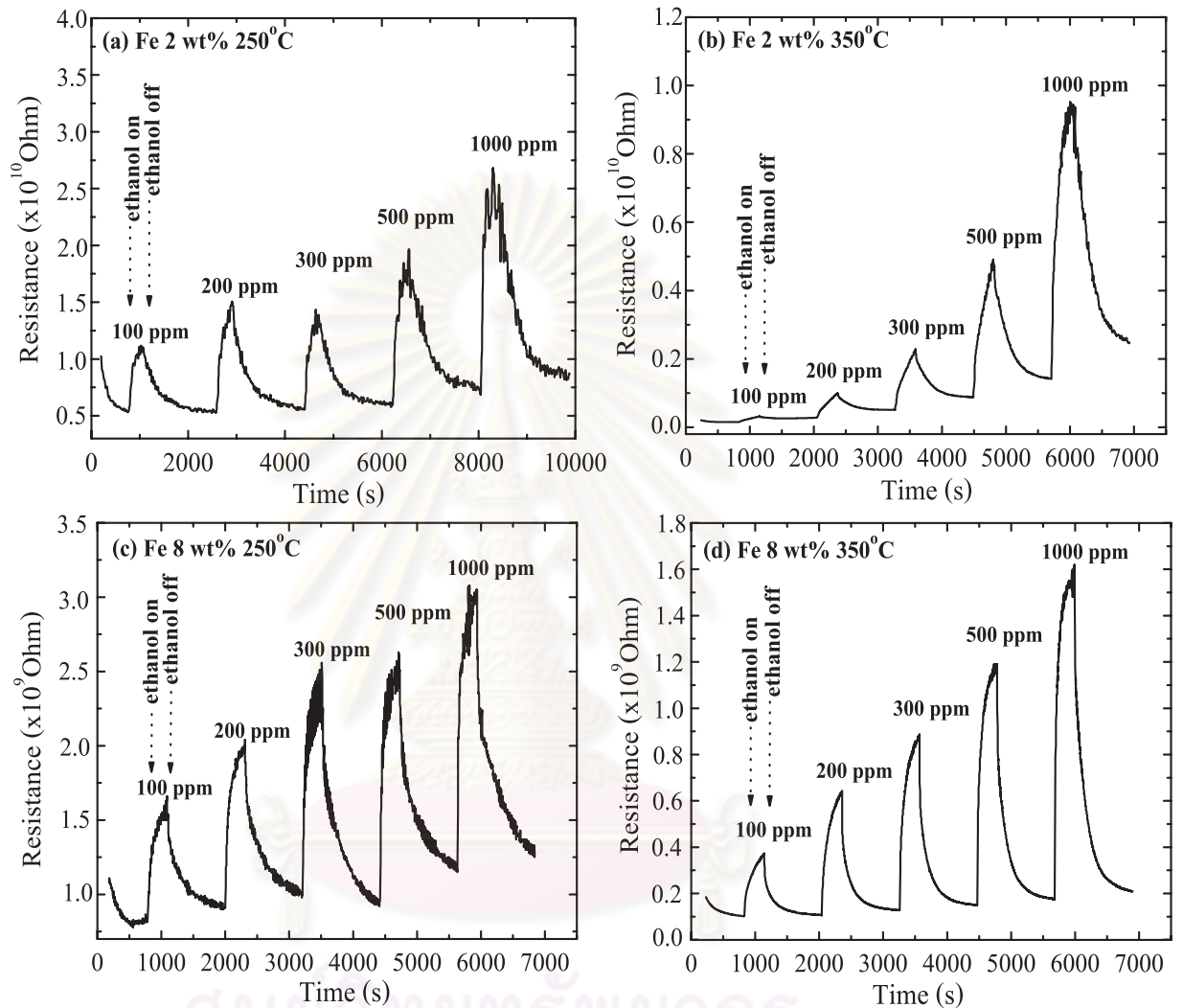


Figure 5.18: The dynamic response to ethanol with concentration ranging 100 to 1000 ppm of SrTiO₃/BaTiO₃ multilayer films doped with (a) Fe 2 wt% operating at 250 °C, (b) Fe 2 wt% operating at 350 °C, (c) Fe 8 wt% operating at 250 °C, and (d) and Fe 8 wt% operating at 350 °C with increasing ethanol concentration in the range of 100-1000 ppm.

increased to 280 °C, the resistance came back to almost the initial value [24]. However, the senior project done by Mr. Pornpipat Wongwarakarn [155] under the supervision of Assistant Prof. Dr. Satreerat K. Hodak have been observed that the resistance of the sensor based on $\text{CaCu}_3\text{Ti}_4\text{O}_{12}$ films can turn to 90% of the initial value after removal of ethanol gas for 15 min for all operating conditions. For our dynamic response curves, there are some conditions that we can approximate the response and recovery time. The response and recovery time for the sensors based on the film doped with Fe 2 wt% operating at 250 °C are presented in Table 5.3 while those of the sensors made from 8 wt% Fe-doped films measuring at 250 and 350 °C are shown in Table 5.4 and 5.5, respectively.

Table 5.3: Response and recovery time of $\text{SrTiO}_3/\text{BaTiO}_3$ films doped with Fe 2 wt% operating at 250 °C.

Ethanol concentration (ppm)	Response time (min.)	Recovery time (min.)
100	4.0	11.7
200	4.4	12.6
300	4.0	12.4
500	3.8	14.7
1000	3.0	14.4

Table 5.4: Response and recovery time of $\text{SrTiO}_3/\text{BaTiO}_3$ films doped with Fe 8 wt% operating at 250 °C.

Ethanol concentration (ppm)	Response time (min.)	Recovery time (min.)
100	4.0	10.8
200	3.0	12.5
300	2.8	7.5
500	2.4	> 15
1000	2.1	11.8

Table 5.5: Response and recovery time of SrTiO₃/BaTiO₃ films doped with Fe 8 wt% operating at 350 °C.

Ethanol concentration (ppm)	Response time (min.)	Recovery time (min.)
100	4.4	4.8
200	3.9	5.7
300	3.5	5.7
500	2.8	5.5
1000	2.4	5.8

Our sensor response shows that the recovery time is longer than the response time. This could be possibly related to the slower chemical reaction kinetics between ethanol molecules and oxygen ions adsorbed on the film surface during the recovery period. If all the oxygen species are depleted, there may be a longer recovery time. The formation of acetic acid, which has the lowest vapor pressure of all the products, may also lead to a longer recovery time due to its ability to bind on surface cations via the carboxylate group discussed earlier in equation 2.31. In contrast, at elevated temperatures, the chemical reaction rate is higher causing a shorter recovery time for the sensors whereas the response time for each case is comparable. Sensitivity as a function of ethanol concentrations are explained by the space charge model as follows [25];

$$S_r = a + bC^N \quad (5.4)$$

where a and b are constants, C is the gas concentration, N is an exponent which could be $1/2$ or 1 depending on oxygen species which coverage on the film surface [156, 157]. It has been proposed that N is 1 for O^- and $1/2$ for O^{2-} . The values of N can be determined from the slope by plotting $\ln S_r$ versus C , which the values of a and b constants approach 0 and 1 , respectively. The sensitivity at different operating temperatures of the films doped with Fe 2 wt% and 8 wt% are shown in Fig. 5.19. The insert in each Fig. 5.19 shows a linear relationship between

$\ln(S_r)$ versus $\ln(C)$. We found that the values of N were in the 0.16-0.24 range for the films operating at 250 °C and increase to the range of 0.38-0.44 for the films operating at higher temperature of 350 °C. Our sensor response at 350 °C according to N nearby 1/2 indicates that oxygen species covered on the film surface being O^{2-} .

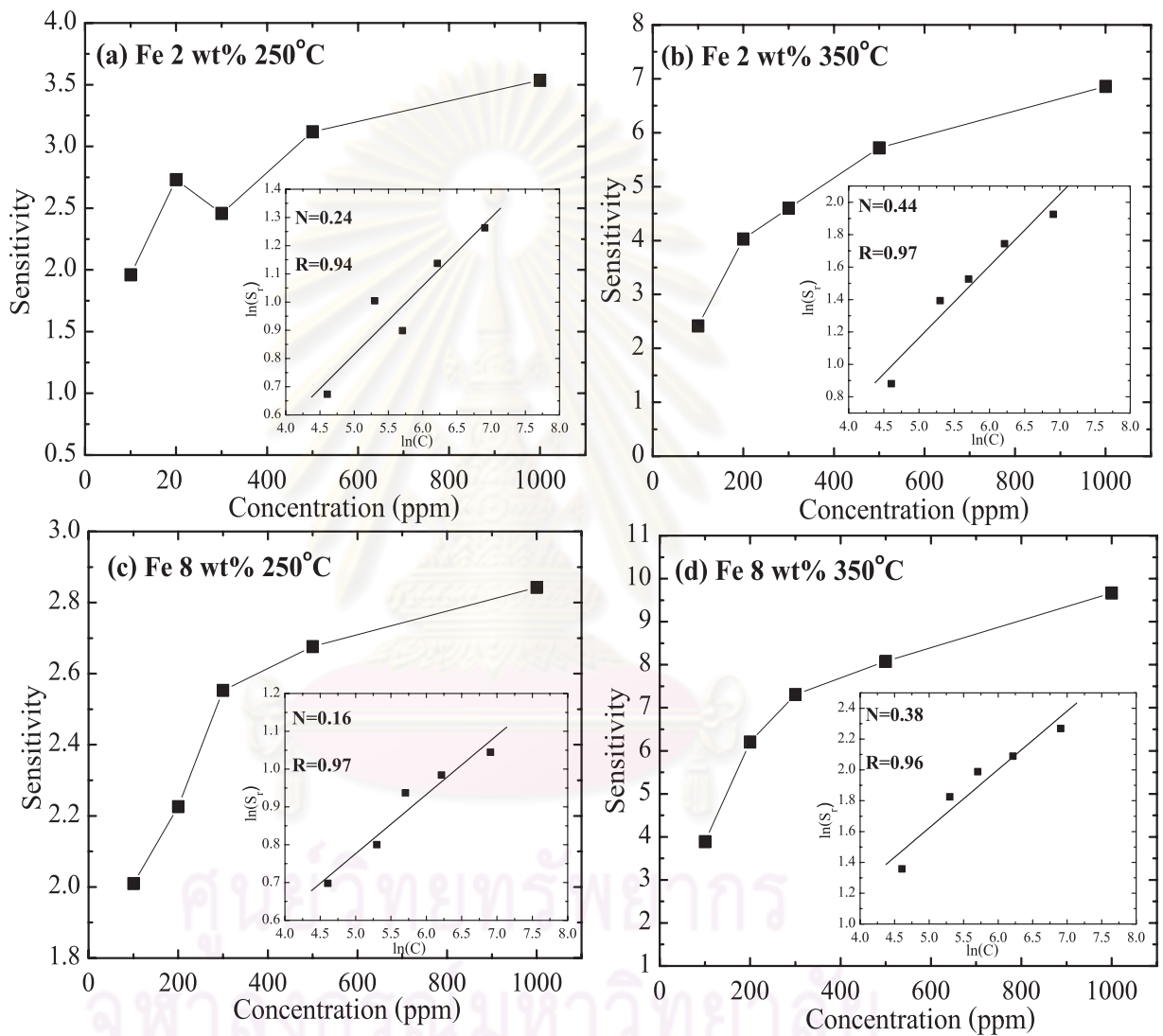


Figure 5.19: Sensitivity of the films doped with (a) Fe 2 wt% operating at 250 °C, (b) Fe 2 wt% operating at 350 °C, (c) Fe 8 wt% operating at 250 °C and (d) Fe 8 wt% operating at 350 °C.

The sensitivity of our ethanol sensors based on 2 wt% Fe-doped films is in the 1.96-3.54 range at the operating temperature of 250 °C and increases up to in the 2.41-6.86 range as the operating temperature increased to 350 °C, and rising up with ethanol concentrations. A similar trend can be perceived for the sensor made from the film doped with Fe 8 wt%. The ethanol sensitivity of Fe 8 wt% doped film is in the 2.00-2.84 and 3.89-9.67 range at operating temperature of 250 °C and 350 °C, respectively. These results show that the highest sensitivity may be obtained at the operating temperature of 350 °C for both films. This is due to the fact that the absorbed oxygen molecule on the film surface can form in increased coverage at high temperatures which induce a larger resistivity variation upon ethanol exposure resulting in an improvement in sensitivity. At fixed operating temperature of 350 °C as shown in Fig. 5.20, we found that the ethanol sensitivity of sensors made from Fe 8 wt% doped films is 1-2 times higher than that of the films doped with Fe 2 wt%. We note that with higher Fe concentrations in the film, a better sensitivity is obtained. This is possibly due to the surface morphology of the films doped with more iron has smaller grains and more porous structures which enhance the reaction between absorbed oxygen molecules on the film surface and the ethanol gas.

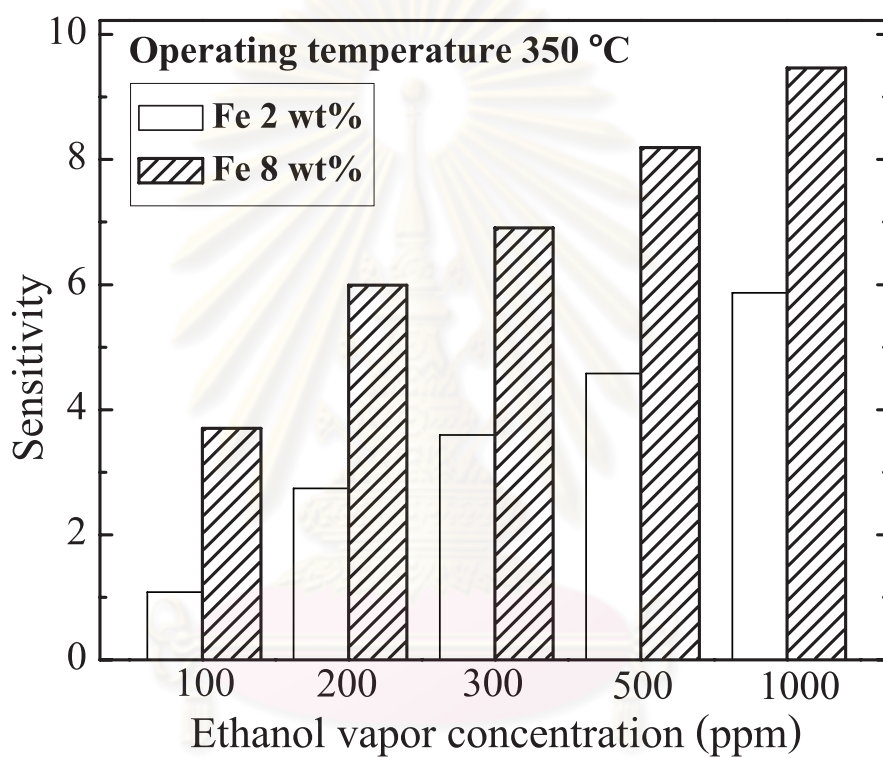


Figure 5.20: Comparison of ethanol sensitivity of the films doped with Fe 2 wt% and 8 wt% with different concentrations at operating temperature of 350 °C.

5.6 Effect of multilayer structure film and Fe dopant on dielectric constant

There are many reports on dielectric constant properties indicating that the dielectric constant of films can be enhanced by increasing annealed temperature. Work by Joshi et al. reported that dielectric constant of BaTiO_3 prepared by metallo-organic solution deposition technique increases from 70 to 255 with increase of annealed temperature from 500 to 700 °C at a frequency of 100 kHz carried out at room temperature without applied voltage [158]. Quan et al. deposited $\text{Ba}_{0.9}\text{Sr}_{0.1}\text{TiO}_3$ films by radio frequency magnetron sputtering technique. They found that the dielectric constant of as-deposited $\text{Ba}_{0.9}\text{Sr}_{0.1}\text{TiO}_3$ film and the films annealed at 650, 700 and 750 °C were 517, 591, 696 and 758, respectively at 1 MHz [48]. The dielectric enhancement of the films with the increase in annealing temperature is due to increase in grain size and improved crystallinity of the films yielding strain and stress developed in the film structure. As discussed earlier in section 5.1, we obtained the large grain size for the films annealed at high temperature of 1000 °C. From this reason to study the effect of multilayer structure film and Fe dopant on dielectric constant, we kept the annealing temperature constant at 1000 °C. Figure 5.21 shows the dielectric constant of BaTiO_3 film as function of frequency in the range from 10-1000 kHz with various applied voltages operating at room temperature. We found that the dielectric constant of BaTiO_3 film decreases with increasing applied frequency and high dispersion of dielectric constant with frequency was clearly observed at frequency below 100 kHz. Whereas at frequency above 100 kHz, the dielectric constant is close to constant value. This dielectric variation on frequency can be attributed to dielectric relaxation which was discussed in section 2.5.2. Moreover, we observed the change in dielectric constant of BaTiO_3 film with both positive and negative bias voltages as illustrated in Figs 5.21(a) and 5.21(b), respectively indicating the ferroelectric properties of BaTiO_3 at room temperature.

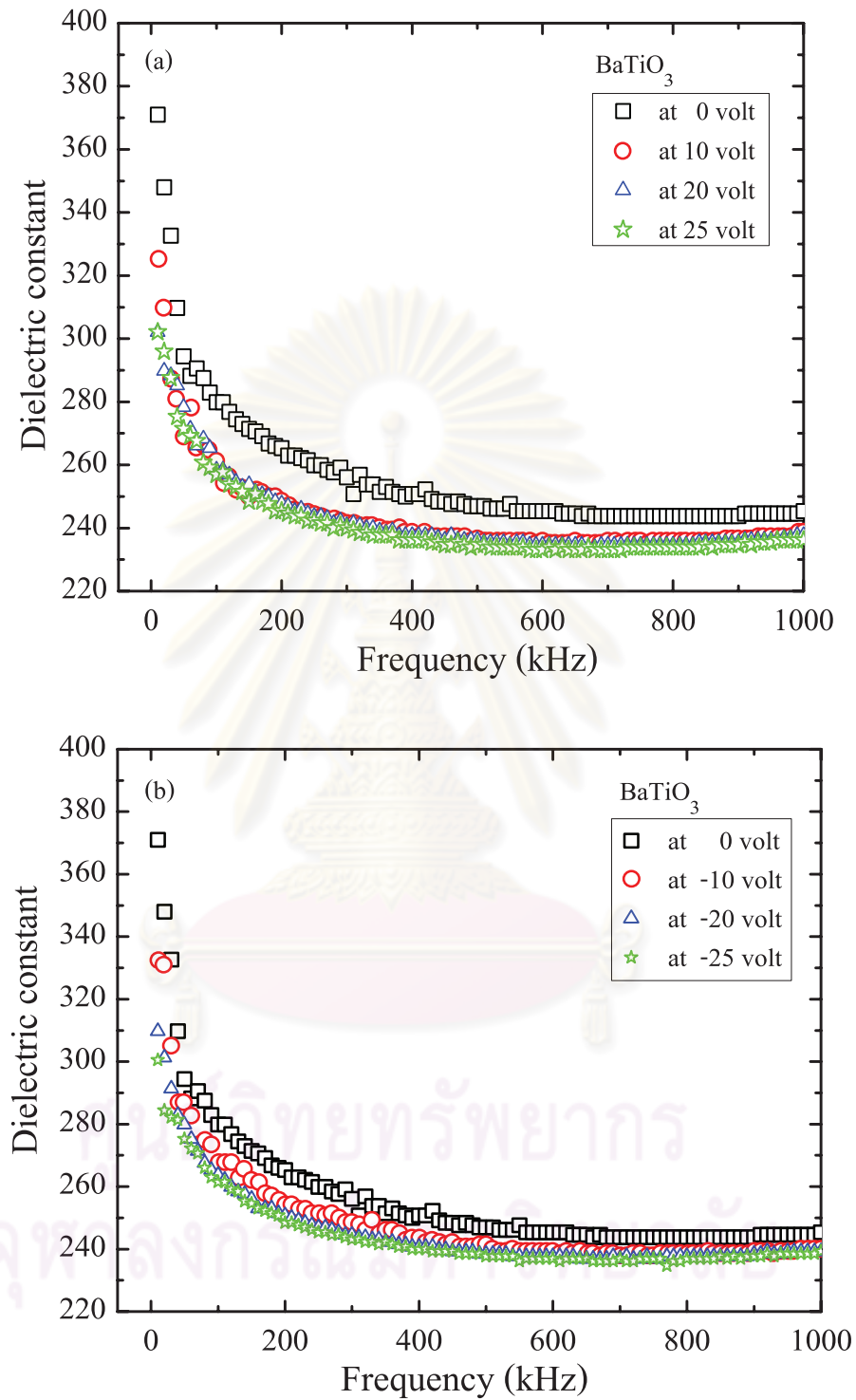


Figure 5.21: The frequency dependence of dielectric constant of BaTiO₃ with applied voltage at (a) 0 to 25 volt and (b) 0 to -25 volt at room temperature.

The tunability percentage of dielectric constant of thin films was calculated by the formula;

$$\% \text{Tunability} = \frac{\varepsilon_{\max} - \varepsilon_{\min}}{\varepsilon_{\min}} \times 100, \quad (5.5)$$

where ε_{\max} and ε_{\min} are the maximum and minimum dielectric constant, respectively over investigated voltage range. In our work, dielectric constants of BaTiO₃ films are 280, 261, 258, 256, 268, 264 and 261 at 0, 10, 20, 25, -10, -20 and -25 V, respectively and tunabilities of BaTiO₃ capacitors were found to be about 7.03%, 8.30% and 8.95% at a very small applied electric field of 1, 2 and 2.5 kV/cm, respectively at 100 kHz. Work by Xu et al. reported that under high electric field of 300 kV/cm and at frequency of 100 kHz, the dielectric tunability of BaTiO₃ films is about 35% [159]. Our dielectric constant values were comparable to that reported by Joshi et al. [158], Lee et al. [160] and Liu et al. [161] for films prepared by sol-gel process. The frequency dependence of room temperature dielectric constant of SrTiO₃ film with different applied voltages is presented in Fig. 5.22. It has been seen that there is no change in dielectric constant of SrTiO₃ film on bias voltages up to 25 V. In other word, SrTiO₃ capacitor can not tune with applied electric field at room temperature. This result confirms that SrTiO₃ is paraelectric and the structure is cubic phase at room temperature. We found that the value of dielectric constant made from SrTiO₃ films is about 188 at 100 kHz which is smaller than that of SrTiO₃ films prepared by pulse laser deposition [162].

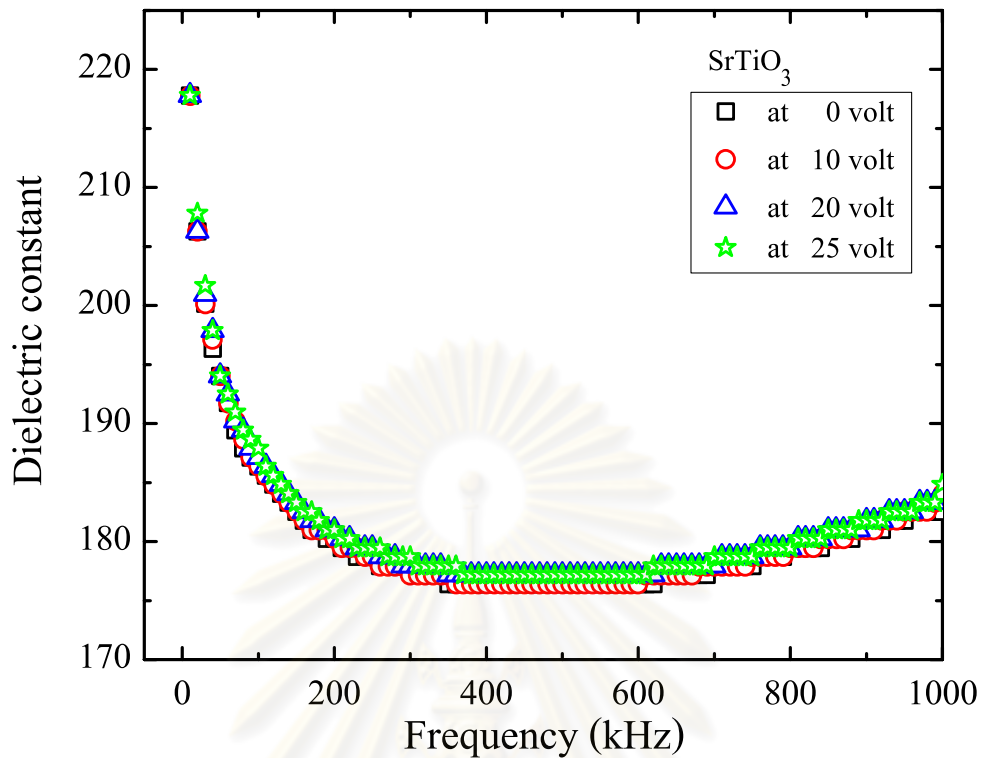


Figure 5.22: The frequency dependence of dielectric constant of SrTiO_3 with applied voltage from 0 to 25 volt at room temperature.

Similar dielectric constant versus frequency behavior has been also observed in SrTiO_3 and BaTiO_3 multilayer films as shown in Fig. 5.23. It has been clearly seen that the dielectric constant of multilayer films dramatically change with bias voltages compared with uniform BaTiO_3 . At a frequency of 100 kHz, dielectric constants were found to be about 521, 464, 445, 434, 466, 447 and 437 at 0, 10, 20, 25, -10, -20 and -25 respectively. Dielectric tunability of multilayer films are about 12.28%, 17.07% and 20.04% at applied electric field of 1, 2 and 2.5 kV/cm, respectively (see Fig. 5.24). Our results showed that the films grown with multilayer structure the tunability was be improved. We compare the dielectric constant and loss tangent of all films as well as 8 wt% Fe-doped multilayer film as a function of applied frequency at zero bias voltage as depicted in Fig. 5.25(a) and 5.25(b), respectively. All films were grown with 5 layers of deposition for which the thickness of the films is approximately 600 nm. Deposition conditions

for the film growth can be seen in Table 4.2. We found that dielectric constant of multilayer films not only undoped films but also Fe-doped films exhibits high dielectric constant. The values of room temperature dielectric constant and loss tangent of all films at 100 kHz are shown in Table 5.6.

Table 5.6: The value of dielectric constant and loss tangent of all films at 100 kHz with no bias voltage.

Materials	Dielectric constant	Loss tangent
SrTiO ₃	188	0.017
BaTiO ₃	280	0.028
Fe-doped SrTiO ₃ /BaTiO ₃	497	0.049
SrTiO ₃ /BaTiO ₃	522	0.058

ศูนย์วิทยทรัพยากร
จุฬาลงกรณ์มหาวิทยาลัย

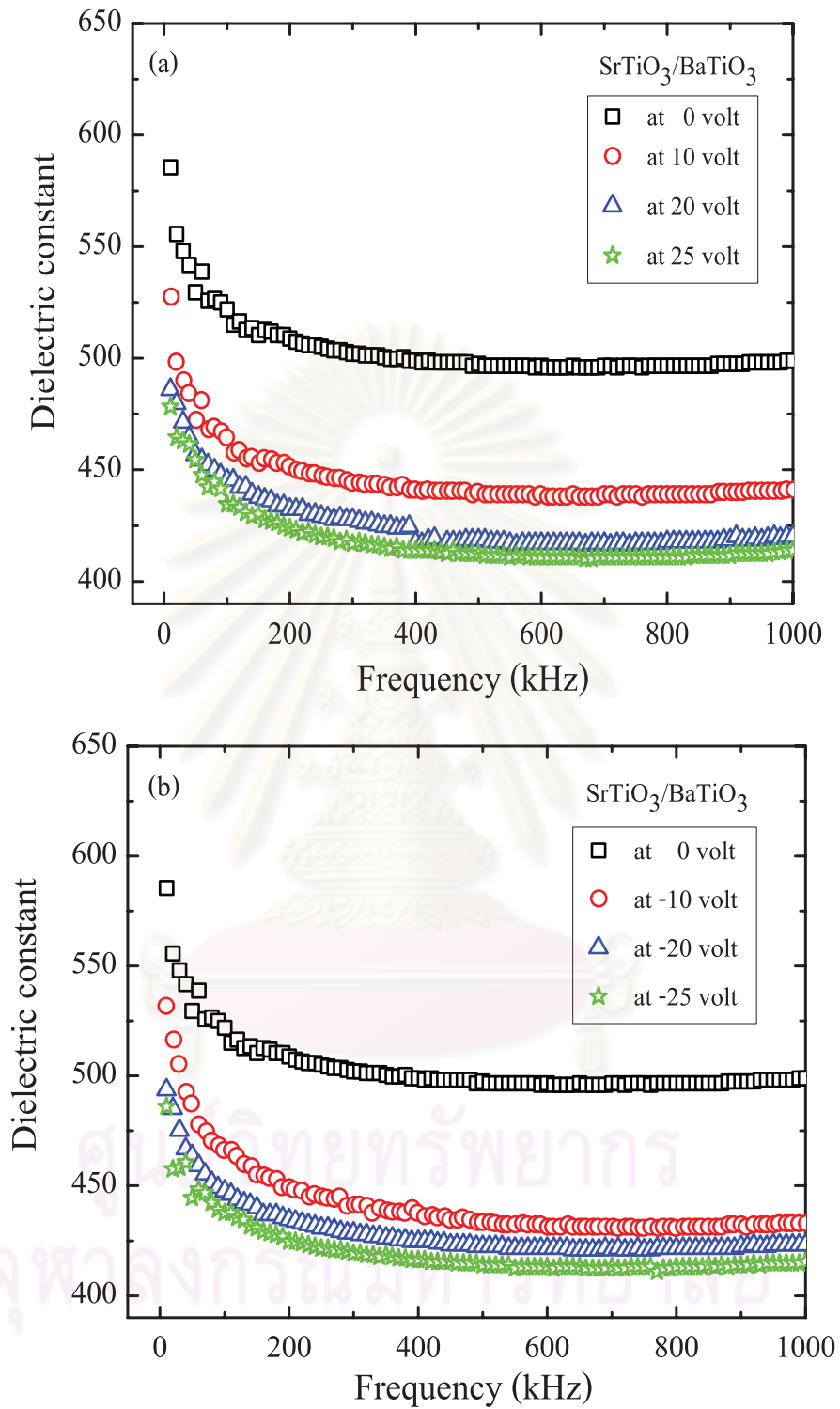


Figure 5.23: The frequency dependence of dielectric constant of SrTiO₃/BaTiO₃ films with applied voltage at (a) 0 to 25 volt and (b) 0 to -25 volt at room temperature.

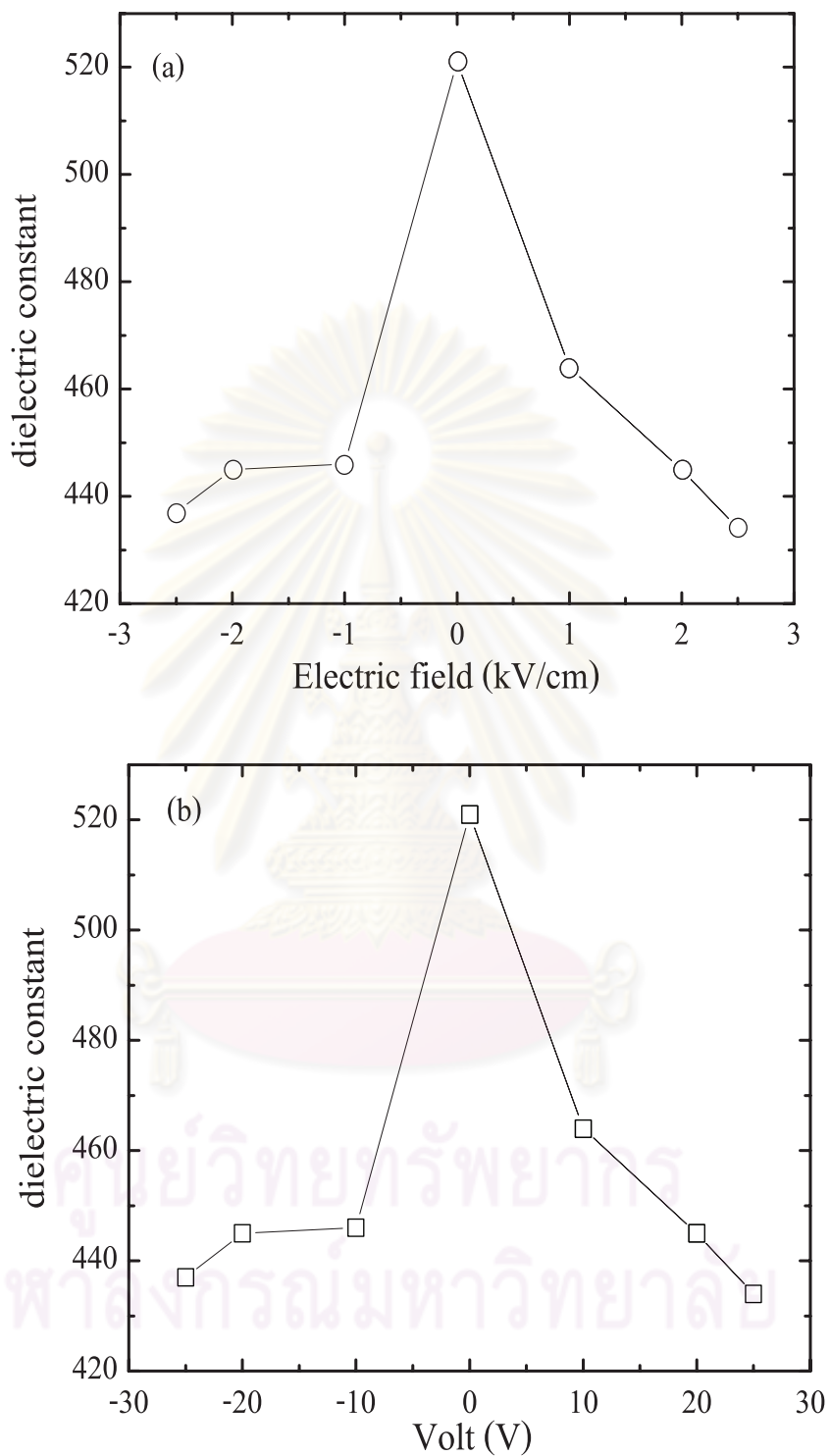


Figure 5.24: The room temperature dielectric constant as a function of (a) applied electric field and (b) volt of BaTiO₃/SrTiO₃ multilayer films.

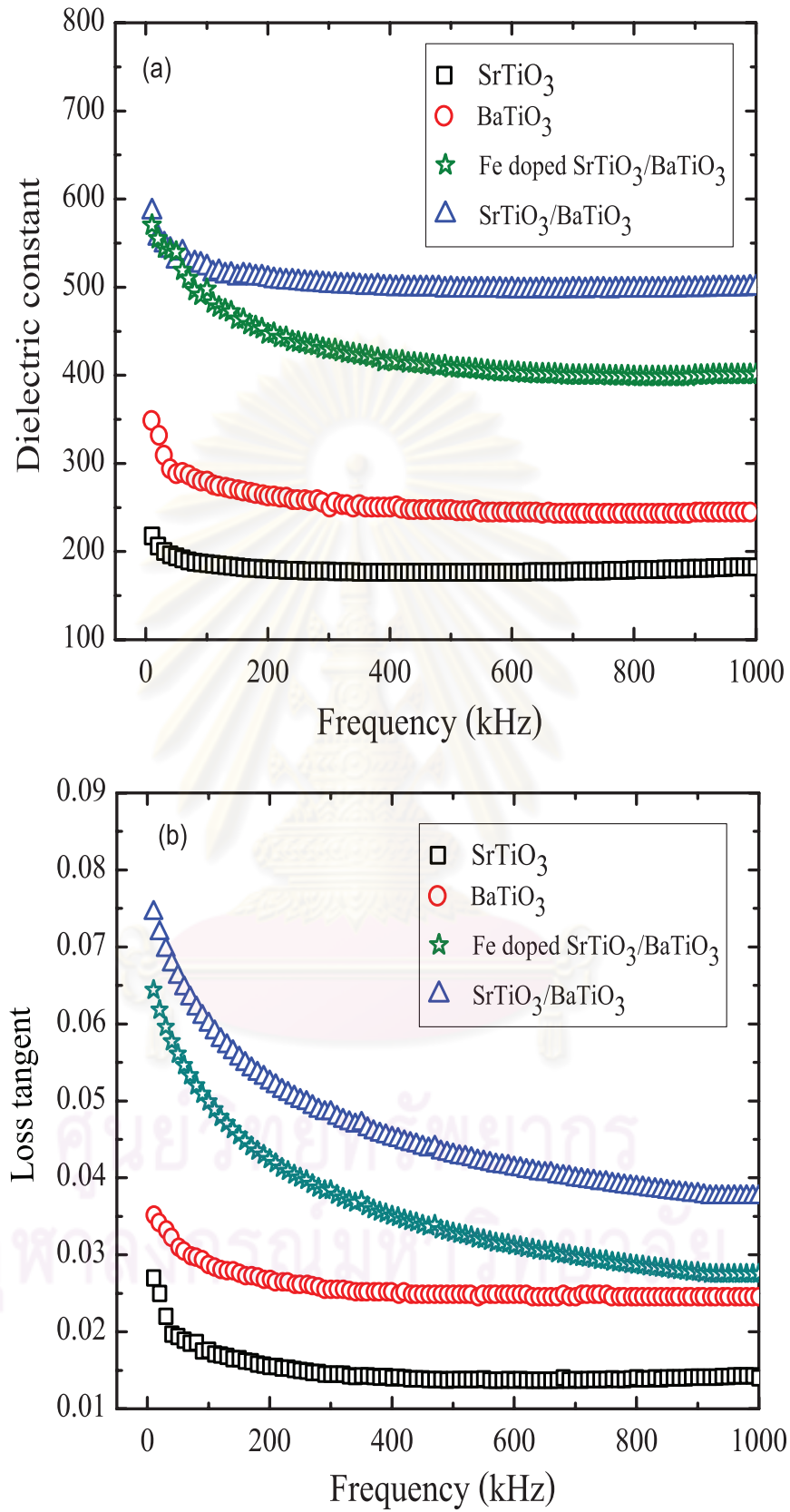


Figure 5.25: The value of dielectric constant of all the films without applied voltage measured at room temperature.

The enhancement of dielectric constant and tunability observed in multilayer films is due to the fact that strain induces lattice distortion resulting from the mismatch of lattice parameter between SrTiO_3 and BaTiO_3 . Figure 5.26 depicts the formation of $\text{SrTiO}_3/\text{BaTiO}_3$ superlattices. SrTiO_3 bulk has cubic structure with lattice constant of 3.905 \AA [56], whereas BaTiO_3 bulk has tetragonal structure with lattice constant of $a = 3.992 \text{ \AA}$ and $c = 4.036 \text{ \AA}$ [136]. Due to the fact that

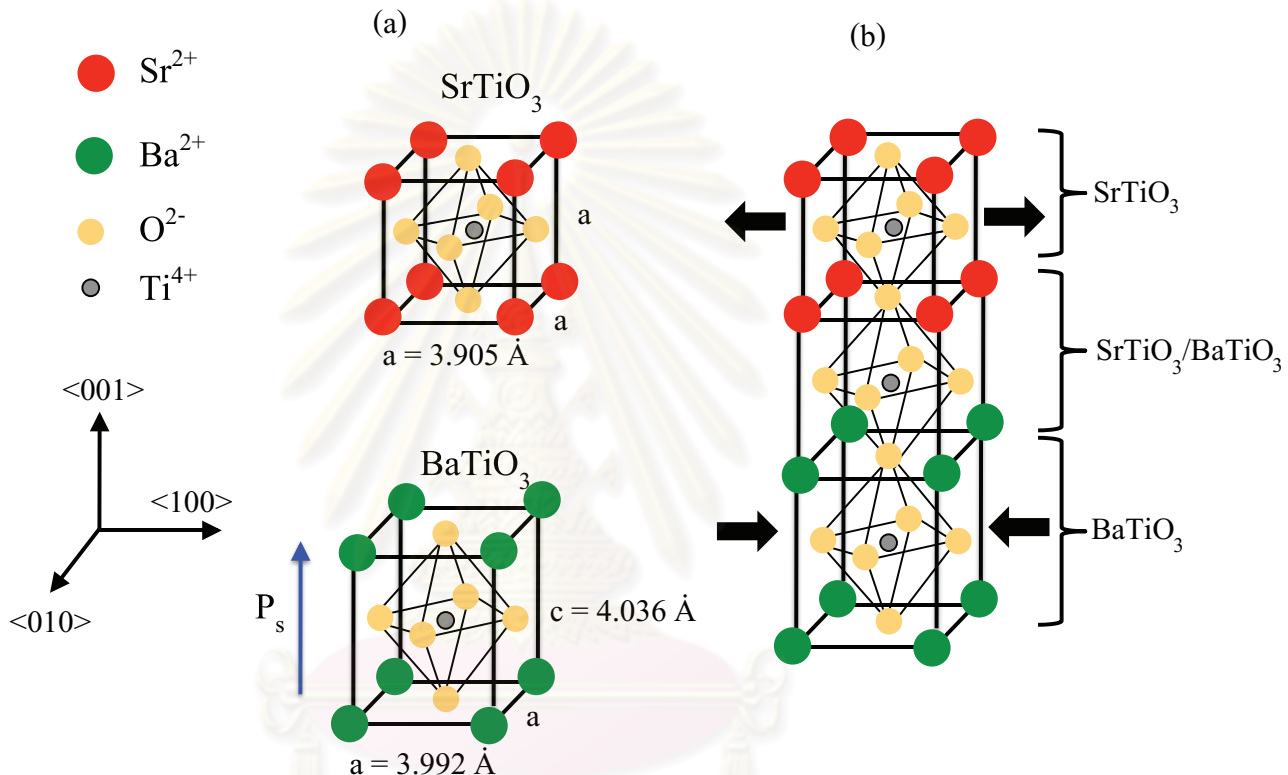


Figure 5.26: Schematic presentation of (a) perovskite unit cell of SrTiO_3 and BaTiO_3 (b) formation of $\text{SrTiO}_3/\text{BaTiO}_3$ superlattices. The arrows denote the induced compressive stress in BaTiO_3 and the tensile stress in SrTiO_3 .

Ti^{4+} ions in tetragonal structure are displaced with O^{2-} ions, the spontaneous polarization P_s in BaTiO_3 is along the elongated lattice direction $\langle 001 \rangle$ as shown in Fig 5.26(a). Since the lattice constant of SrTiO_3 is smaller than both a and c lattice constant of BaTiO_3 , the coherent interface introduces $\langle 100 \rangle / \langle 010 \rangle$ in-plane compressive stress into BaTiO_3 and tensile stress into the SrTiO_3 layer as presented by arrows in Fig. 5.26(b). There are theoretical studies reporting the

interfacial strain-polarization coupling issues [62]. The reports suggest that the compressive stress state in the BaTiO₃ layer tends to maintain the polarization component along the <001> direction. Also, this polarization induces aligned dipoles in the SrTiO₃ layer. In addition, the increase of stacking number results in the development of a dipole component along <100>/<010> direction. Zhu et al. studied the effect of compressive strain on the polarization properties of the BaTiO₃/SrTiO₃ superlattice by using a first-principles calculation [63]. They pointed out that with increasing strain from 0.3-1.5%, displacement of Ti and O atoms increased from 0.007-0.015 in unit cell vector as well as the polarization raised from 18.9 to 28.5 $\mu\text{C cm}^{-2}$. However, compared with undoped multilayer films, dielectric constant of the films doped with Fe presents a lower dielectric constant and larger dispersion with frequency. The decrease in dielectric constant of Fe-doped films can be attributed to reduction in grain size of the films contributed to the width of domain. The theoretical investigations observed the correlation between domain width and grain size indicating that the domain width was proportional to (grain size)^m, where $m = 1/2$ [163, 164, 165]. It was known that stable domain width in ferroelectric materials is the result of a balance of energy. As the width of domain is smaller, the domain wall energy per volume would be higher. On the other hand, as domain width is larger, the energies of electric and mechanical field would be higher. Nevertheless, such correlation between domain width and grain size can be applied for tetragonal ferroelectric phase of material with grain size in the range between 1 and 10 μm . Arlt et al. investigated the domain width contribution in BaTiO₃ ceramic [166]. Their results revealed the departure of domain width and grain size correlation from parabolic relation for grain size below 0.5 μm . They mentioned that at smaller grain size (< 0.5 μm), the 90° domain wall vanished. In addition, Arlt et al. also experimentally and theoretically observed the dielectric constant dependence on the average grain diameter as shown in Fig. 5.27. At grain size above 1 μm the dielectric constant decreased with increasing average grain diameter which matched calculated dielectric constant curve. However, at grain size below 1 μm , the significant decrease

of dielectric constant was be observed. They pointed out that the reduction in dielectric constant with decreasing grain diameter below $1 \mu\text{m}$ was due to gradual changes from tetragonal to pseudocubic structure and by coexistence of both phase. Many experimental works also reported grain size dependence on permittivity for BaTiO_3 ceramic as presented in Fig. 5.28 [166, 167, 168, 169]. At micron level, the permittivity decreased with increasing grain size whereas it reduced at submicron level.

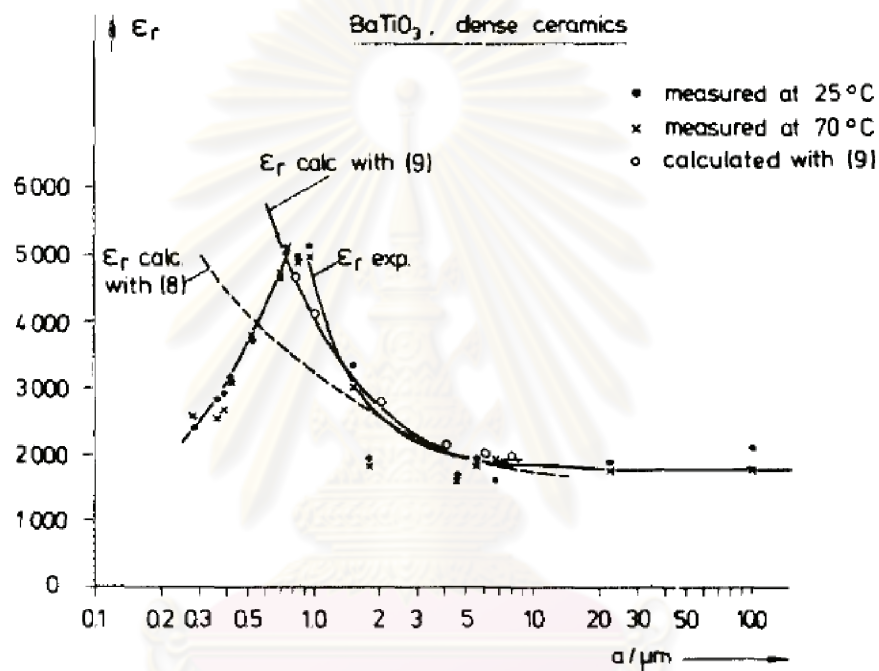


Figure 5.27: Dielectric constant of BaTiO_3 plotted as a function of average grain diameter reported by Arlt et al.

ศูนย์วิทยทรัพยากร
จุฬาลงกรณ์มหาวิทยาลัย

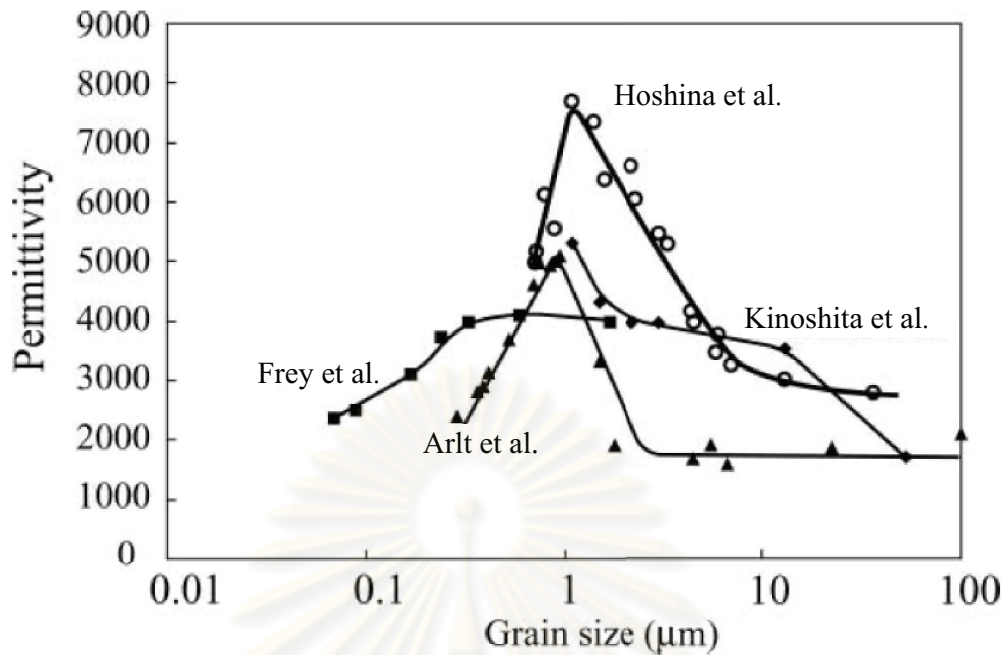


Figure 5.28: Grain size dependence of permittivity of BaTiO₃ ceramics

Figure 5.29 shows the dispersion curves of room temperature capacitance and loss tangent of all films without applied voltage. We observed that the capacitance and loss tangent of the films are in the 1.31-1.26 pF and 0.03-0.01 range, respectively for uniform SrTiO₃ and in the 1.52-1.34 pF and 0.04-0.02, respectively for uniform BaTiO₃. The capacitance increases to in the range of 1.76-1.54 pF and 1.78-1.69 pF for Fe-doped multilayer and undoped multilayer films, respectively accompanied with the enhancement in loss tangent in the 0.06-0.03 and 0.07-0.04, respectively.

ศูนย์วิทยทรัพยากร
จุฬาลงกรณ์มหาวิทยาลัย

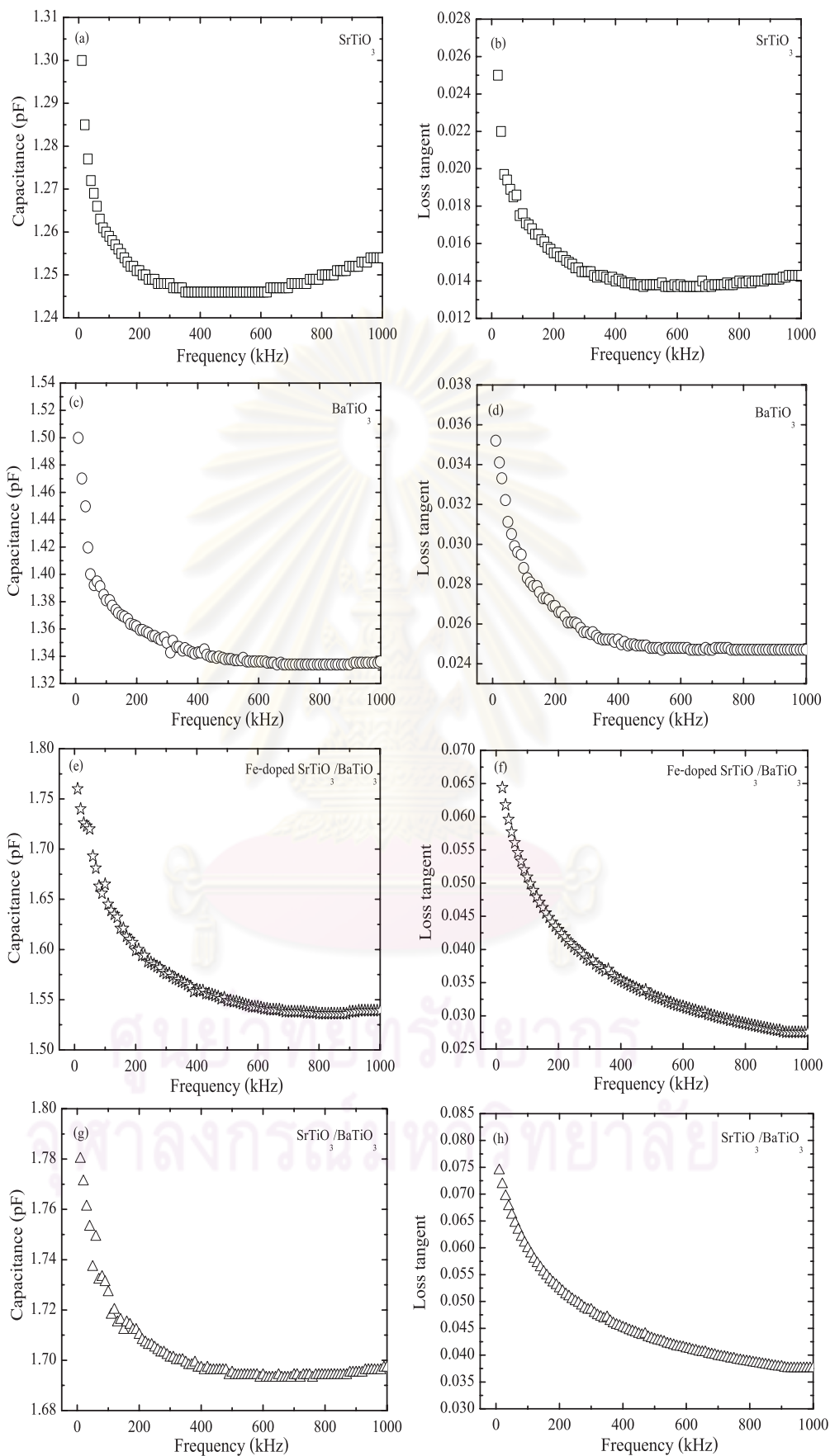


Figure 5.29: The frequency dependence of capacitance and loss tangent of all the films without applied voltage measured at room temperature.

5.7 Effect of gamma irradiation on dielectric constant

In this thesis work, the capacitors made from SrTiO₃ and BaTiO₃ multilayer films were chosen to investigate the effect of gamma irradiation on their dielectric constants due to maximum dielectric constant compared with others. ⁶⁰Co gamma source (Gammacell 220 Excell) with an activity of 10 kCi was used to expose the capacitors to gamma irradiation. The capacitors were irradiated at three dose values of gamma ray including 4.82, 10.57 and 28.64 kGy. However, we estimated these values as 5, 10 and 30 kGy, respectively. The details of experimental part for gamma irradiation can be read from Ornnicha Kongwut's thesis [170]. Figure 5.30 shows the capacitance and loss tangent of SrTiO₃/BaTiO₃ multilayer films after exposure to gamma ray at dose of 5, 10 and 30 kGy without applied voltage. Before gamma irradiation the capacitance and loss tangent of SrTiO₃/BaTiO₃ multilayer films are in the 1.78-1.69 pF and 0.074-0.038 range, respectively. After exposing to gamma ray, the films show change in capacitance. With increment of radiation dose, the capacitance of the films increases. We found that the capacitance of the film exposed to gamma at a dose of 5 kGy is in the 1.86-1.78 pF range accompanied with the increase in loss tangent in the 0.087-0.051 range. As the film irradiated to more radiation dose at 10 kGy, the capacitance and loss increase to 1.93-1.92 pF and 0.096-0.062 range, respectively. The values of capacitance reach a maximum when the film was exposed with 30 kGy of gamma dose, which the capacitance and loss are in the 2.14-2.08 pF and 0.109-0.073 range, respectively. The enhancement in capacitance as a result in increase in the dielectric constant of the films. Figure 5.31 compares dielectric constant of SrTiO₃/BaTiO₃ multilayer films before and after irradiation with gamma dose at 5, 10 and 30 kGy. Our dielectric constant was found to be in the 647-586 range for gamma irradiation at dose of 5 kGy, in the 739-689 range for gamma irradiation at dose of 10 kGy and in the 862-812 range for gamma irradiation at dose of 30 kGy. The increase in capacitance and dielectric constant after irradiating to gamma ray were also reported in other

literatures [69, 72, 171]. Arshak et al. found that bismuth germinate ($\text{Bi}_4\text{Ge}_3\text{O}_{12}$) thin films showed the increase of capacitance from 2.97 pF to 7.09 pF after gamma irradiation with a small dose of 2.44 mGy [69]. Work done by Tugluoglu et al. has been observed that the dielectric constant for Au/SnO₂/n-Si (MOS) structures was affected by strong gamma irradiation dose rate, which dielectric constant increased in a small range of 1.06-1.18 after exposing to gamma ray at a dose of 500 kGy [72]. Sinha et al. reported that the dielectric constant for polyallyldiglycol carbonate (PADC) increased from 32 at a 100 kGy gamma dose to 42 at 1000 kGy gamma dose [171]. The significant enhancement in dielectric constant after exposing to gamma ray may be attributed to the energetic gamma ray displacing the atoms in the crystal during irradiation. This generates the vacancies and charge carriers trapped at that sizes inducing ease of orientation of dipolar molecules. Hence, the capacitance increases as a consequence of increase in dielectric constant and loss tangent.

We future do an experiment to confirm that atoms in crystal were displaced by gamma irradiation. The irradiated films were heated at temperature of 100 °C for 30 min and were re-examined the capacitance. Figure 5.32 presents (a) capacitance, (b) dielectric constant and (c) loss tangent of SrTiO₃/BaTiO₃ films after gamma radiation dose of 10 kGy and heating at 100 °C for 30 min. Fig. 5.33 shows (a) capacitance, (b) dielectric constant and (c) loss tangent of SrTiO₃/BaTiO₃ films exposed to gamma ray at dose of 30 kGy and heating at 100 °C for 30 min. Our results reveal that the capacitance of both films exposed to gamma ray significantly decreased after the films were heated. We found that the values of capacitance of the heated film after gamma irradiation at dose of 10 kGy reduced to 1.74-1.80 pF and that for heated film after gamma irradiation at dose of 30 kGy also become lower to 1.77-1.84 pF. The capacitance values of heated films after exposing to gamma ray decreased closely to the capacitance values of films before gamma irradiation, which was in the range of 1.69-1.78 pF (see Fig. 5.29(g)). Energetic gamma ray can affect all atoms in crystal regardless of charge of ions due to gamma has no charge. Nevertheless, in this study we can not in-

dicates which atoms were displaced but the lighter atom was possible to easily be displaced. Atomic mass of Ba, Sr, Ti and O is 137.33, 87.62, 47.87 and 16.00 amu, respectively [172]. From XRD experiment done by Ornicha Kongwut and Dr. Satreerat Hodak showed that there was no observation in shift of XRD peak of BaTiO₃ after gamma irradiation [67], namely, they found no change in lattice parameter corresponding to tetragonal distortion. This might be due to the small error of XRD fitting leading to a small displacement of atoms. By comparing with Fig. 5.29 and 5.31, the dielectric constant and loss tangent of heated films after irradiating to gamma ray at dose of 10 kGy decreased to in the range of 557-600 and 0.047-0.084, respectively. A similar result of reduction in dielectric constant and loss tangent also found for heated films after irradiating to gamma ray at dose of 30 kGy, which the dielectric constant and loss tangent were in the range of 581-631 and 0.055-0.092, respectively. The observed reduction in dielectric constant by heating the films may be due to the fact that the displaced atoms by gamma ray come back to former location and leaving charge carriers trapped at that size producing decrease in orientation of dipole molecules. Thus, the capacitance decreases as a consequence of reduction in dielectric constant and loss tangent.

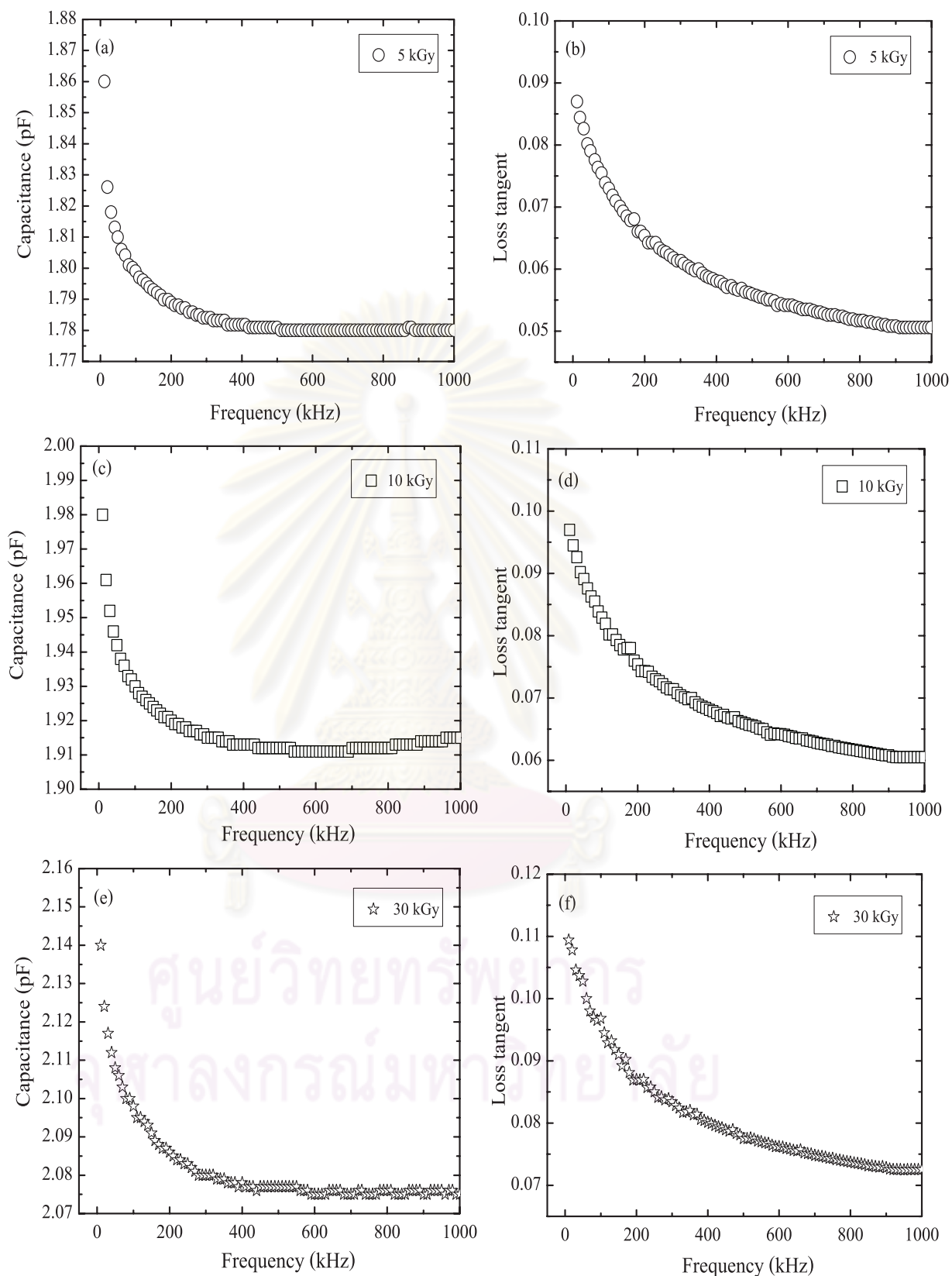


Figure 5.30: The frequency dependence of capacitance and loss tangent of SrTiO₃/BaTiO₃ films after exposure to gamma at dose of 5, 10 and 30 kGy.

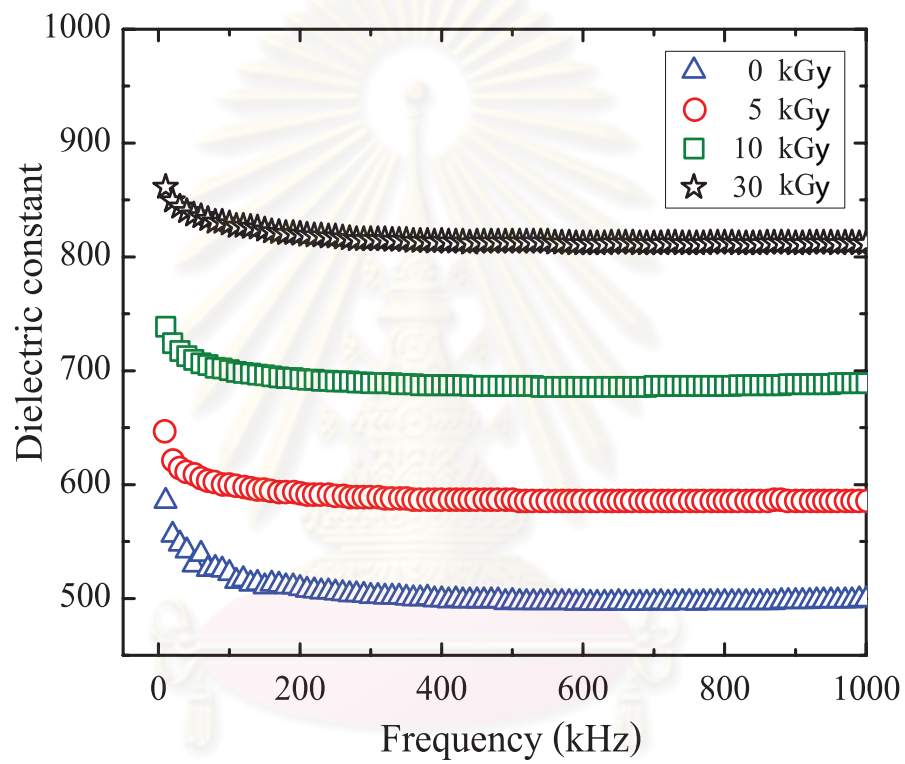


Figure 5.31: The dielectric constant of $\text{SrTiO}_3/\text{BaTiO}_3$ films as a function of frequency with various gamma irradiations.

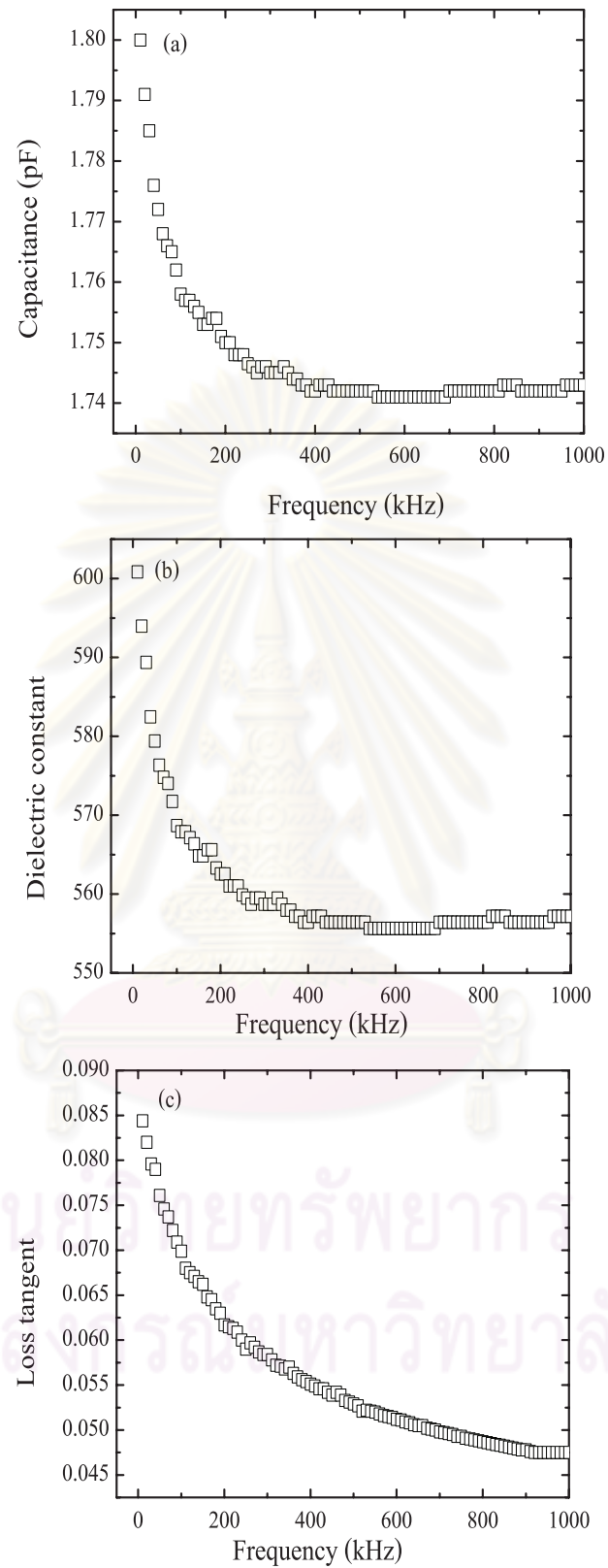


Figure 5.32: The (a) capacitance (b) dielectric constant and (c) loss tangent of $\text{SrTiO}_3/\text{BaTiO}_3$ films exposed to gamma ray at dose of 10 kGy and heating at 100°C for 30 min.

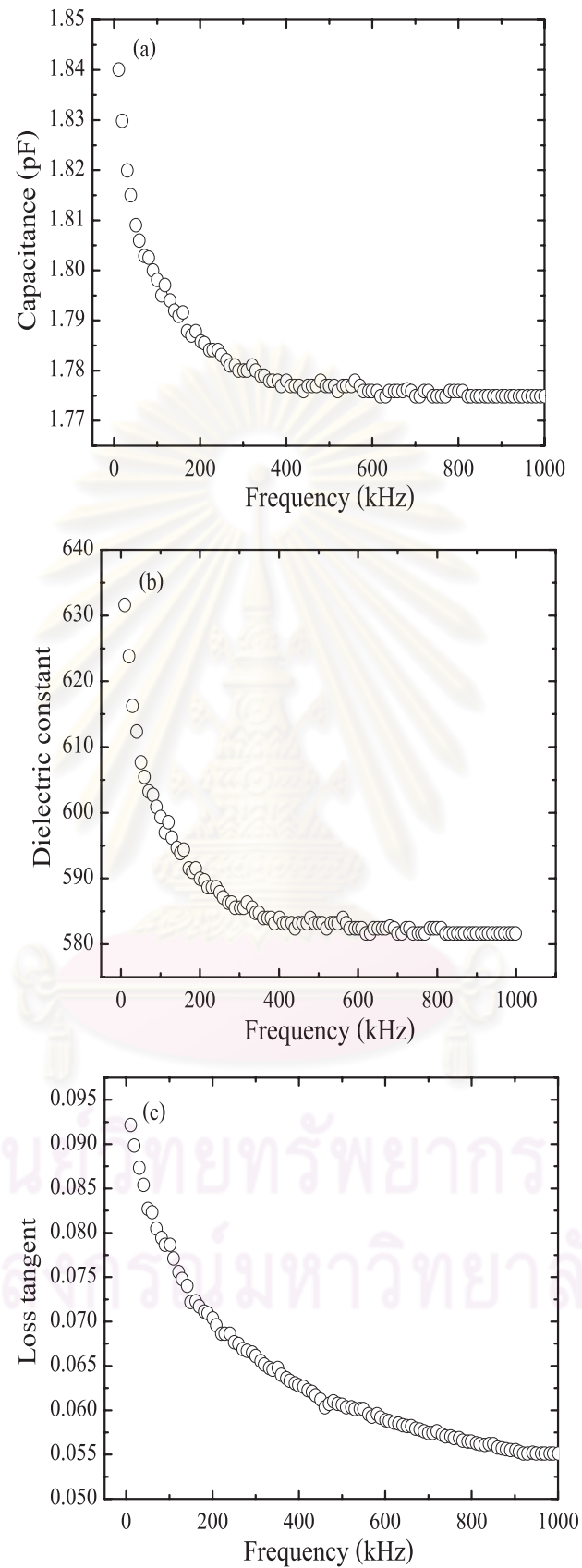


Figure 5.33: The (a) capacitance (b) dielectric constant and (c) loss tangent of $\text{SrTiO}_3/\text{BaTiO}_3$ films exposed to gamma ray at dose of 10 kGy and heating at 100 °C for 30 min.

CHAPTER VI

CONCLUSION

In this thesis, we prepared SrTiO₃/BaTiO₃ as well as Fe-doped SrTiO₃/BaTiO₃ films with multilayer structure by a sol gel spin coating method. The used substrates were chosen according to the desired applications. SrTiO₃/BaTiO₃ multilayer films were deposited onto ITO coated on glass substrates to investigate the optical properties. Alumina was chosen as a substrate for growing SrTiO₃/BaTiO₃, Fe-doped SrTiO₃/BaTiO₃ as well as uniform BaTiO₃ and SrTiO₃ films in order to characterize the electrical properties including dielectric and gas sensing properties.

For investigating optical properties, the operating temperature was varied in the range of 300-650 °C. The maximum operating temperature limited at 650 °C was due to avoid weakening of glass substrate. From XRD results the films annealed above 600 °C showed more pronounced crystallinity with phase separated mixture of SrTiO₃ and BaTiO₃ crystallites and with increasing annealing temperature, the large grain size could be obtained. The transmission spectra of the films were measured in the 200-800 nm wavelength range. All the films exhibited optical transmittance of near 85% in the visible region. Tunable band gaps can be obtained by varying annealing temperatures. We found that the value of energy gap gradually decreased from 4.19 to 4.03 eV as the films were annealed at lower temperature (300-550 °C) while that of the films annealed beyond 600 °C was in the 3.64-3.74 eV range. The refractive index of the films was in the range of 1.69-2.10 depending on annealing temperature and the extinction coefficient of the films was in the order of 10⁻² which indicate low optical losses with the film

annealed at 650 °C showing the lowest loss.

Then we moved on to characterize gas sensing properties. The annealing temperature was kept constant at 1000 °C. It was known that the gas sensing performance is influenced by grain size and porosity which could be adjusted through metal doping. The films were doped with Fe as concentrations of 2 wt%, 4 wt% and 8 wt%, respectively. The XAS spectra noticed Fe ions in the films being a Fe^{3+} oxidation state. We further investigated the effect of Fe dopant on the microstructure and surface morphology of the films. We observed that the lattice parameter decreased as Fe concentration increased. Our calculated lattice constant for undoped SrTiO_3 with cubic structure was 3.902 Å while that for Fe-doped SrTiO_3 was 3.900 Å for Fe 2 wt%, 3.894 Å for 4 wt% and 3.884 Å for 8 wt%. For BaTiO_3 , we found that the lattice parameter was 4.009 Å, 4.008 Å, 4.003 Å and 4.000 Å with Fe doping concentration of 0, 2, 4 and 8 wt%, respectively. The reduction in lattice constant is due to a slightly smaller size of Fe^{3+} substituting into Ti^{4+} . The FESEM results revealed that with increasing Fe content, the surface morphology of the films had a tendency to more porous structure and decrease in grain size of the films. The ethanol sensitivity could be improved through increase in Fe doping content, with our films acting as a p-type semiconductor. The sensitivity of our ethanol sensors performed the best at 350 °C. The obtained sensitivity to ethanol vapor concentration in the 100-1000 ppm of the films doped with Fe 8 wt% is in the 3-10 range which is about two times higher than that of the Fe 2 wt% doped films. This improvement in ethanol sensing performance is may be due to with more addition of iron into the films causing a smaller grains and more porous structures which increase the reaction between absorbed oxygen molecules on the film surface and ethanol gases.

The last properties of BaTiO_3 and SrTiO_3 films which were investigated are dielectric properties. We repeated several experiments and compared our results with many literatures. Our results confirmed that the dielectric constant can be enhanced through growing the films with heterostructure of BaTiO_3 and SrTiO_3 of which the dielectric constant as measured at room temperature without applied

electrical field was approximately 522 at 100 kHz while that of uniform BaTiO₃ and SrTiO₃ films were about 280 and 188, respectively. The significant increase of dielectric constant observed in heterostructure films is because strain induces lattice distortion caused by the mismatch of lattice constant between BaTiO₃ and SrTiO₃. In addition, the improvement in tunability also obtained with multilayer films whereas Fe-doped heterostructure films exhibited a little lower dielectric constant than that of undoped multilayer films. A new supplementary research on the dielectric properties for BaTiO₃ and SrTiO₃ materials is to explore the influence of gamma irradiation on dielectric properties. We noticed that the dielectric constant of multilayer films significantly increased after exposure to gamma irradiation. For example, the dielectric constant at 100 kHz operating at room temperature without applied voltage increased up to 830 associated with the dielectric loss of 0.096 after irradiated to gamma ray at dose of 30 kGy. The increase in the values of dielectric constant after presenting in gamma irradiation can be attributed to the atoms in the crystal removed by energetic gamma ray. This creates the vacancies and charge carriers trapped at that size yielding easily orientable dipolar molecules. Consequently, the capacitance increases along with the enhancement in dielectric constant accompanied with the increase in dielectric loss.

ศูนย์วิทยทรัพยากร
จุฬาลงกรณ์มหาวิทยาลัย

References

- [1] Werle, P., Muecke, R., Amato, F. D., and Lancia, T. Near-infrared trace-gas sensors based on room-temperature diode lasers. *Appl. Phys. B* 67 (1998): 307–315.
- [2] Marsal, A., Cornet, A., and Morante, J. R. Study of the CO and humidity interference in La doped tin oxide CO₂ gas sensor. *Sens. Actuation, B* 94 (2003): 324–329.
- [3] Gu, Z. and Liang, P. Novel optical film sensor design based on p-polarized reflectance. *Opt. Laser Techno.* 36 (2004): 211–217.
- [4] Yang, D., Lu, H. H., Chen, B., and Lin, C. W. Surface plasmon resonance of SnO₂/Au bi-layer films for gas sensing applications. *Sens. Actuation, B* 145 (2010): 832–838.
- [5] Stankova, M. et al. Sensitivity and selectivity improvement of rf sputtered WO₃ microhotplate gas sensors. *Sens. Actuation, B* 113 (2006): 241–248.
- [6] Vaishampayan, M. V., Deshmukh, R. G., Walke, P., and Mulla, I. Fe-doped SnO₂ nanomaterial: a low temperature hydrogen sulfide gas sensor. *Mater. Chem. Phys.* 109 (2008): 230–234.
- [7] Tang, H. et al. A selective NH₃ gas sensor based on Fe₂O₃ZnO nanocomposites at room temperature. *Sens. Actuation, B* 114 (2006): 910–915.
- [8] Park, K. and Seo, D. J. Gas sensing characteristics of BaTiO₃-based ceramics. *Mater. Chem. Phys.* 85 (2004): 47–51.
- [9] Fergus, J. W. Perovskite oxides for semiconductor-based gas sensors. *Sens. Actuators, B* 123 (2007): 1169–1179.

- [10] Jain, G. H. and Patil, L. A. Gas sensing properties of Cu and Cr activated BST thick films. *Bull. Mater. Sci.* 29 (2006): 403–411.
- [11] Ishihara, T., Kometani, K., Nishi, Y., and Takita, Y. Improved sensitivity of CuO-BaTiO₃ capacitive type CO₂ sensor by additives. *Sens. Actuator, B* 28 (1995): 49–54.
- [12] Herran, J., Mandayo, G. G., and Castano, E. Solid state gas sensor for fast carbon dioxide detection. *Sens. Actuation, B* 129 (2008): 705–709.
- [13] Hu, Y., Tan, O. K., Cao, W., and Zhu, W. A low temperature nano-structured SrTiO₃ thick film oxygen gas sensor. *Ceram. Int.* 30 (2004): 1819–1822.
- [14] Hara, T. and Ishiguro, T. Oxygen sensitivity of SrTiO₃ thin film prepared using atomic layer deposition. *Sens. Actuation, B* 136 (2009): 489–493.
- [15] Gerblinger, J., Heppel, U., and Meixner, H. Accurate sensors offering unrestricted recalibration and long-term stability for determining high temperatures on the basis of gas-sensitive effects of different gases on metal oxides. *Sens. Actuation, B* 34 (1996): 224–228.
- [16] Jain, G. et al. Surface modied BaTiO₃ thick film resistors as H₂S gas sensors. *Sens. Actuators, B* 117 (2006): 159–165.
- [17] More, P. et al. Unidentified H₂ gas sensing characteristics of BaTiO₃:Cu composition. *Mater. Lett.* 61 (2007): 2891–2895.
- [18] Sahner, K., Gouma, P., and Moos, R. Electrodeposited and sol-gel precipitated p-type SrTi_{1-x}Fe_xO_{3-δ} semiconductors for gas sensing. *Sensors* 7 (2007): 1871–1886.
- [19] Chaudhari, G., Bambole, D., and Bodade, A. Structural and gas sensing behavior of nanocrystalline BaTiO₃ based liquid petroleum gas sensors. *Vacuum* 81 (2006): 251–256.

- [20] Sahner, K. et al. HC-sensor for exhaust gases based on semiconducting doped SrTiO₃ for on-board diagnosis. *Sens. Actuators, B* 114 (2006): 861–868.
- [21] Bene, R., Pinter, Z., Perczel, I. V., Fleischer, M., and Reti, F. High-temperature semiconductor gas sensors. *Vacuum* 61 (2001): 275–278.
- [22] Wisitsoraat, A., Tuantranont, A., Patthanasettakul, V., Lomas, T., and Chindaudom, P. Ion-assisted e-beam evaporated gas sensor for environmental monitoring. *Sci. Technol. of Adv. Mater.* 6 (2005): 261–265.
- [23] Tianshu, Z., Hing, P., Li, Y., and Jiancheng, Z. Selective detection of ethanol vapor and hydrogen using Cd-doped SnO₂-based sensors. *Sens. Actuators, B* 60 (1999): 208–215.
- [24] Hongstith, N., Viriyaworasakul, C., Mangkorntong, P., Mangkorntong, N., and Choopun, S. Ethanol sensor based on ZnO and Au-doped ZnO nanowires. *Ceram. Int.* 34 (2008): 823–826.
- [25] Chen, D. et al. The enhanced alcohol-sensing response of ultrathin WO₃ nanoplates. *Nanotechnology* 21 (2010): 035501–035512.
- [26] Wang, Z. and Liu, L. Synthesis and ethanol sensing properties of Fe-doped SnO₂ nanofibers. *Mater. Lett.* 63 (2009): 917–919.
- [27] Aswal, D. K. and Gupta, S. K.. *Science and Technology of Chemiresistor Gas Sensors*. New York: Nava Science Publishers, Inc. 2006.
- [28] Tan, O. K., Cao, W., Zhu, W., Chai, J. W., and Pan, J. S. Ethanol sensors based on nano-sized α -Fe₂O₃ with SnO₂, ZrO₂, TiO₂ solid solutions. *Sens. Actuator, B* 93 (2003): 396–401.
- [29] Garzella, C. et al. Novel selective ethanol sensors: W/TiO₂ thin films by sol-gel spin-coating. *Sens. Actuators, B* 93 (2003): 495–502.
- [30] Ihokura, K. and Watson, J.. *Stannic Oxide Gas Sensors: Principles and Applications*. Boca Raton: CRC Press, Inc. 2000.

- [31] Koch, C. C.. *Nanostructured Materials: Processing, Properties, and Applications*. New York: William Andrew, Inc. 2007.
- [32] Kuwaba, M. Influence of stoichiometry on the PTCR effect in porous barium titanate ceramics. *J. Am. Ceram. Soc.* 64 (1981): C-170.
- [33] Kim, J. G., Cho, W. S., and Park, K. PTCR characteristics in porous (Ba,Sr)TiO₃ ceramics produced by adding partially oxidized Ti powders. *Mater. Sci. Eng. B* 77 (2000): 255–260.
- [34] Kim, J. G., Cho, W. S., and Park, K. Effect of atmosphere on the PTCR characteristics of porous (Ba,Sr)TiO₃ ceramics. *Mater. Sci. Eng., B* 83 (2001): 123–129.
- [35] Pinto, N. J., Ramos, I., Rojas, R., Wang, P. C., and Jr., A. T. J. Electric response of isolated electrospun polyaniline nanobers to vapors of aliphatic alcohols. *Sens. Actuators, B* 129 (2008): 621–627.
- [36] Raksa, P. et al. Ethanol sensing properties of CuO nanowires prepared by an oxidation reaction. *Ceram. Int.* 35 (2009): 649–652.
- [37] Yang, Z. et al. Ethanol gas sensor based on Al-doped ZnO nanomaterial with many gas diffusing channels. *Sens. Actuators, B* 140 (2009): 549–556.
- [38] Mandayo, G. G., Gonzalez, F., Rivasa, I., Ayerdi, I., and Herran, J. BaTiO₃-CuO sputtered thin film for carbon dioxide detection. *Sens. Actuators, B* 118 (2006): 305–310.
- [39] Pourfayaz, F., Khodadadi, A., Mortazavi, Y., and Mohajezadeh, S. CeO₂ doped SnO₂ sensor selective to ethanol in presence of CO, LPG and CH₄. *Sens. Actuators, B* 108 (2005): 172–176.
- [40] Tianshu, Z., Hing, P., Li, Y., and Jiancheng, Z. Selective detection of ethanol vapor and hydrogen using Cd-doped SnO₂ based sensors. *Sens. Actuators, B* 60 (1999): 208–15.

- [41] Neri, G. et al. FeSrTiO₃-based resistive oxygen sensors for application in diesel engines. *Sens. Actuation, B* 134 (2008): 647–653.
- [42] Lin, F., Jiang, D., Ma, X., and Shi, W. Influence of doping concentration on room-temperature ferromagnetism for Fe-doped BaTiO₃ ceramics. *J. Magn. Magn. Mater.* 320 (2008): 691694.
- [43] Kumar, A. S. et al. Magnetic and ferroelectric properties of Fe doped SrTiO_{3-δ} films. *J. Magn. Magn. Mater.* 200 (2010): 092010–092014.
- [44] Guo, Y., Suzuki, K., Nishizawa, K., Miki, T., and Kato, K. Dielectric and piezoelectric properties of highly (1 0 0)-oriented BaTiO₃ thin film grown on a Pt/TiO_x/SiO₂/Si substrate using LaNiO₃ as a buffer layer. *J. Cryst. Growth* 284 (2005): 190–196.
- [45] Madeswaran, S., Giridharan, N. V., Varatharajan, R., Ravi, G., and Jayavel, R. Effect of rhodium doping on the growth and characteristics of BaTiO₃ single crystals grown by step-cooling method. 266 (2004): 481–486.
- [46] Dalberth, M. J., Stauber, R. E., Price, J. C., Rogers, C. T., and Galt, D. Improved low frequency and microwave dielectric response in strontium titanate thin films grown by pulsed laser ablation. *Appl. Phys. Lett.* 72 (1998): 507–509.
- [47] Kampangkeaw, S.. *Effect of Crystal Structure on Strontium Titanate Thin Films and Their Dielectric Properties*. PhD thesis, University of Colorado at Boulder 2004.
- [48] Quan, Z. et al. Effect of annealing temperature on microstructure, optical and electrical properties of sputtered Ba_{0.9}Sr_{0.1}TiO₃ thin films. *Appl. Surf. Sci.* 255 (2009): 9045–9053.
- [49] Xu, R., Shen, M., Ge, S., Gan, Z., and Cao, W. Dielectric enhancement of solgel derived BaTiO₃/SrTiO₃ multilayered thin films. *Thin Solid Films* 406 (2002): 113–117.

- [50] Hsi, C. S., Shiao, F. Y., Wu, N. C., and Wang, M. C. Characterization and dielectric properties of $(\text{SrTiO}_3/\text{BaTiO}_3)_n$ multilayer thin films deposited on Pt/Ti/SiO₂/Si substrates by double rf magnetron sputtering. *Solid State Commun.* 125 (2003): 633–636.
- [51] Koebernik, G., Haessler, W., Pantou, R., and Weiss, F. Thickness dependence on the dielectric properties of BaTiO₃/SrTiO₃-multilayers. *Thin Solid Films* 449 (2004): 80–85.
- [52] Wang, Y., Liu, B., Wei, F., Yang, Z., and Du, J. Effect of (Ba + Sr/Ti) ratio on the dielectric properties for highly (1 1 1) oriented (Ba,Sr)TiO₃ thin films. *Journal of Alloys and Compounds* 475 (2009): 827–831.
- [53] Iijima, K., Terashima, T., Bando, Y., Kamikagi, K., and Terauchi, H. Atomic layer growth of oxide thin films with perovskite-type structure by reactive evaporation. *J. Appl. Phys.* 72 (1992): 2840–2845.
- [54] Kim, T. U. et al. Integration of artificial SrTiO₃/BaTiO₃ superlattices on Si substrates using a TiN buffer layer by pulsed laser deposition method. *J. Cryst. Growth* 289 (2006): 540–546.
- [55] Hu, D., Shen, M., and Cao, W. Dielectric enhancement in interface-modified BaTiO₃/SrTiO₃ multilayered films prepared by pulsed laser deposition. *Microelectron. Eng.* 83 (2006): 553–556.
- [56] Huang, H. H., Hsiao, F. Y., Wu, N. C., and Wang, M. C. Preparation and characterization of SrTiO₃/BaTiO₃ thin multilayer films deposited on Pt/Ti/SiO₂/Si substrate by radio frequency magnetron sputtering. *J. Non-Cryst. Solids* 351 (2005): 3809–3815.
- [57] Wang, Z., Yasuda, T., Hatatani, S., and Oda, S. Enhanced dielectric properties in SrTiO₃/BaTiO₃ strained superlattice structures prepared by atomic-layer metal organic chemical vapor deposition. *Jpn. J. Appl. Phys.* 38 (1999): 6817–6820.

- [58] Tong, F., Yu, W., Liu, F., Zuo, Y., and Ge, X. Microstructural study of BaTiO₃/SrTiO₃ superlattice. *Mater. Sci. Eng., B* 98 (2003): 6–9.
- [59] Pill, S. and Lee, Y. H. The dielectric properties of BaTiO₃/SrTiO₃ hetero-layered thick films by screen printing method. *Trans. Electr. Electron. Mater.* 6 (2005): 210–213.
- [60] Pontesa, F. and Leitea, E. Dielectric properties and microstructure of SrTiO₃/BaTiO₃ multilayer thin films prepared by a chemical route. *Thin Solid Films* 385 (2001): 260–265.
- [61] Gim, Y. et al. Microstructure and dielectric properties of Ba_{1-x}Sr_xTiO₃ films grown on LaAlO₃ substrates. *Appl. Phys. Lett.* 77 (2000): 1200–1202.
- [62] Chaib, H., Khalal, A., and Nafidi, A. Theoretical investigation of spontaneous polarization and dielectric constant of BaTiO₃/SrTiO₃ superlattice. *Ferroelectrics* 386 (2009): 41–49.
- [63] Zhu, Z. Y., Zhang, H. Y., Tan, M., Zhang, X. H., and Han, J. C. First-principles study of the response to strain in BaTiO₃/SrTiO₃ superlattices. *J. Phys. D: Appl. Phys* 41 (2008): 215408–215411.
- [64] Zhang, J., Yin, Z., and Zhang, M. Dielectric properties of ferroelectric strained superlattices BaTiO₃/SrTiO₃. *Thin Solid Films* 375 (2000): 255–258.
- [65] Li, W. L., Lin, H. J., Hsiao, F. Y., Wu, N. C., and Wang, M. C. Crystal structure and dielectric characterization of a (SrTiO₃/BaTiO₃)_n multilayer film prepared by radio frequency magnetron sputtering. *Metall. Trans. A* 41 (2010): 1330–1337.
- [66] Guigues, B. et al. SrTiO₃/BaTiO₃ multilayers thin films for integrated tunable capacitors applications. *J. Eur. Ceram. Soc.* 27 (2007): 3851–3854.

- [67] Kongwut, O., Kornduangkeaw, A., Jangsawang, N., and Hodak, S. K. Influence of gamma irradiation on the refractive index of Fe-doped barium titanate thin films. *Thin Solid Films* 518 (2010): 74077411.
- [68] Arshak, A., Zleetni, S., and Arshak, K. γ -radiation sensor using optical and electrical properties of manganese phthalocyanine (MnPc) thick film. *Sensors* 2 (2002): 174–184.
- [69] Arshak, K. et al. Properties of BGO thin films under the influence of gamma radiation. *Thin Solid Films* 516 (2008): 1493–1498.
- [70] Selcuk, A. B., Ocak, S. B., and Yuksel, O. F. Effects of gamma irradiation on dielectric characteristics of SnO₂ thin films. *Nucl. Instr. Meth. Phys. Res. A* 594 (2008): 395–399.
- [71] Mustafaeva, S. N., Asadov, M. M., and Ismalov, A. A. Effect of gamma irradiation on the dielectric properties and electrical conductivity of the TlInS₂ single crystal. *Phys. Solid State* 51 (2009): 2269–2273.
- [72] Tugluoglu, N., Altindal, S., Tataroglu, A., and Karadeniz, S. Dielectric properties in Au/SnO₂/n-Si (MOS) structures irradiated under ⁶⁰Co- γ rays. *Microelectron. J.* 35 (2004): 731–738.
- [73] Tataroglu, A. and Altindal, S. The effects of frequency and c-irradiation on the dielectric properties of MIS type schottky diodes. *Nucl. Instrum. Methods Phys. Res. Sect. B* 254 (2007): 113–117.
- [74] Hu, G. J. et al. PbZr_{0.4}Ti_{0.6}O₃ and Ba_{0.9}Sr_{0.1}TiO₃ reflectors derived from chemical solutions containing polymers. *Opt. Lett.* 33 (2008): 2062–2064.
- [75] Hiltunen, J. et al. BaTiO₃-SrTiO₃ multilayer thin film electro-optic waveguide modulator. *Appl. Phys. Lett.* 89 (2006): 242904.
- [76] Ouyang, X., Kitai, A. H., and Xiao, T. Electroluminescence of the oxide thin film phosphors Zn₂SiO₄ and Y₂SiO₅. *J. Appl. Phys.* 79 (1996): 3229–3234.

- [77] Zhang, H. X. et al. Optical and electrical properties of sol-gel derived BaTiO₃ films on ITO coated glass. *Mater. Chem. Phys.* 63 (2000): 174–177.
- [78] Kamalasanan, M. N., Kumar, N. D., and Chandra, S. Structural and microstructural evolution of barium titanate thin films deposited by the sol-gel process. *J. Appl. Phys.* 76 (1994): 4603–4609.
- [79] Huang, W., Wu, Z. P., and Hao, J. H. Electrical properties of ferroelectric BaTiO₃ thin film on SrTiO₃ buffered GaAs by laser molecular beam epitaxy. *Appl. Phys. Lett.* 94 (2009): 032905–032907.
- [80] Tsai, H. N., Liang, Y. C., and Lee, H. Y. Characteristics of sputter-deposited BaTiO₃/SrTiO₃ artificial superlattice films on an LaNiO₃-coated SrTiO₃ substrate. *J. Cryst. Growth* 284 (2005): 65–72.
- [81] Bao, D., Yao, X., Wakiya, N., Shinozaki, K., and Mizutani, N. Bandgap energies of sol-gel derived SrTiO₃ thin films. *Appl. Phys. Lett.* 79 (2001): 3767–3769.
- [82] Fasasi, A. et al. Effect of Zn-doping on the structural and optical properties of BaTiO₃ thin films grown by pulsed laser deposition. *Thin Solid Films* 516 (2008): 6226–6232.
- [83] Wang, N. et al. Morphology and microstructure of BaTiO₃/SrTiO₃ superlattices grown on SrTiO₃ by laser molecular beam epitaxy. *Appl. Phys. Lett.* 75 (1999): 3464.
- [84] Ruan, K., Chen, X., Liang, T., Wu, G., and Bao, D. Photoluminescence and electrical properties of highly transparent (Bi,Eu)₄Ti₃O₁₂ ferroelectric thin films on indium-tin-oxide coated glass substrates. *J. Appl. Phys.* 103 (2008): 074101–704104.
- [85] Bruno, E. et al. Morphological and electrical investigations of lead zirconium titanate thin films obtained by sol-gel synthesis on indium tin oxide electrodes. *J. Appl. Phys.* 103 (2008): 064103–064108.

- [86] Fatuzzo, E. and Merz, W. J.. *Ferroelectricity*. John Wiley & Sons, Inc 1967.
- [87] Haeni, J. H. et al. Room-temperature ferroelectricity in strained SrTiO₃. *nature* 430 (2004): 758–760.
- [88] Rossella, F., Galinetto, P., Samoggia, G., Trepakov, V., and Jastrabik, L. Photoconductivity and the structural phase transition in SrTiO₃. *Solid State Commun.* 141 (2007): 95–98.
- [89] Golovenchits, E., Sanina, V., and Babinsky, A. Nonlinear dielectric susceptibility and the possible origin of the low temperature state of SrTiO₃. *Ferroelectrics* 199 (1997): 317–325.
- [90] Govorgian, S.. *Ferroelectrics in Microwave Devices, Circuits and System: Physics, Modeling, Fabrication and Measurements*. Springer 2009.
- [91] Burfoot, J. C.. *Ferroelectric an Introduction to the Physics Principle*. Cananda, D. Van Nostrand Company, Ltd. 1967.
- [92] Prudan, A. M. et al. Permittivity of strontium titanate film in a SrTiO₃/Al₂O₃ structure. *Tech. Phys. Lett.* 24 (1998): 332–333.
- [93] Ham, Y. S. and Koh, J. H. The dielectric characteristics of screen printed SrTiO₃-epoxy composite thick films on the Cu plate PCB substrates. *Ferroelectrics* 382 (2009): 85–91.
- [94] Hong, J. S. and Lancaster, M. J.. *Microstrip Filters of RF/Microwave Applications*. John Wiley & Sons, Inc 2001.
- [95] Santos, H. J. D. L.. *RF MEMS Circuit Design for Wireless Communications*. Artech House microelectromechanical systems series 2002.
- [96] Park, J. Y., Kim, G. H., Chung, K. W., and Bu, J. U. Monolithically integrated micromachined RF MEMS capacitive switches. *Sens. Actuator, A* 89 (2001): 88–94.

- [97] Xiang, F., Wang, H., Yang, H., Shen, Z., and Yao, X. Low loss flexible SrTiO₃/POE dielectric composites for microwave application. *J. Electroceram.* 24 (2010): 20–24.
- [98] Fujioka, H. et al. Epitaxial growth of semiconductors on SrTiO₃ substrates. *J. Cryst. Growth* 229 (2001): 137–141.
- [99] Zhao, Q. et al. GaAs film deposited on SrTiO₃ substrate by molecular beam epitaxy. *J. Cryst. Growth* 208 (2000): 117–122.
- [100] Qiu, P. S., Cheng, W. X., He, X. Y., Zheng, X. S., and Ding, A. L. Epitaxial growth of PLZT thin film on SrTiO₃ substrate by sputtering method. *Integr. Ferroelectr.* 75 (2005): 155–161.
- [101] Hu, Y., Tan, O. K., Pan, J. S., Huang, H., and Cao, W. The effects of annealing temperature on the sensing properties of low temperature nanosized SrTiO₃ oxygen gas sensor. *Sens. Actuators, B* 108 (2005): 244–249.
- [102] Wagner, S. F. et al. Enhancement of oxygen surface kinetics of SrTiO₃ by alkaline earth metal oxides. *Solid State Ion.* 177 (2006): 1607–1612.
- [103] Sherwin, K. and Horsley, M.. *Thermofluids*. London: Chapman&Hall 1996.
- [104] Sakka, S.. *Sol-Gel Science and Technology Processing Characterization and Applications*. Massachusetts: Kluwer Academic Publishers 2005.
- [105] Newnham, R. E.. *Properties of materials*. New york: Oxford University Press, Inc. 2005.
- [106] Bialkowski, S. E.. *Photothermal Spectroscopy Chemical Analysis*. John Wiley & Sons, Inc 1996.
- [107] Vtelino, J. and Reghu, A.. *Introduction to Sensors*. CRC Press, Taylor & Francis Group 2011.

- [108] Pokhrel, S., Huo, L., Zhao, H., and Gao, S. Sol-gel derived polycrystalline $\text{Cr}_{1.8}\text{Ti}_{0.2}\text{O}_3$ thick films for alcohols sensing application. *Sens. Actuator, B* 120 (2007): 560–567.
- [109] Yude, W., Xiaodan, S., Yanfeng, L., Zhenlai, Z., and Xinghui, W. Perovskite-type NiSnO_3 used as the ethanol sensitive material. *Solid-State Electron.* 44 (2000): 2009–2014.
- [110] Hui, W. X., De, W. Y., Feng, L. Y., and Lai, Z. Z. Electrical and gas-sensing properties of perovskite-type CdSnO_3 semiconductor material. *Mater. Chem. Phys.* 77 (2002): 588–593.
- [111] Korotcenkov, G. Gas response control through structural and chemical modification of metal oxide films: state of the art and approaches. *Sens. Actuation, B* 107 (2005): 209–232.
- [112] Wang, C., Yin, L., Zhang, L., Xiang, D., and Gao, R. Metal oxide gas sensors: sensitivity and influencing factors. *Sensors* 10 (2010): 2088–2106.
- [113] Barsan, N., Koziej, D., and Weimar, U. Metal oxide-based gas sensor research: How to?. *Sens. Actuation, B* 121 (2007): 18–35.
- [114] Butter, M., Yamazoe, N., Vanysek, P., and Aizawa, M.. *Chemical Sensor IV*. New Jersey: The Electrochemical Society, Inc. 1999.
- [115] Mishra, S., Ghanshyama, C., Rama, N., Bajpai, R., and Bedi, R. Detection mechanism of metal oxide gas sensor under UV radiation. *Sens. Actuation, B* 97 (2004): 387390.
- [116] Cullity, B.. *Elements of X-Ray Diffraction*. Massachusetts: Addison-Wesley Publishing Company, Inc. 1956.
- [117] Sloop, D. A. and Leary, J. J.. *Principles of Instrumental Analysis*. United state of America: Saunders College Publishing Ltd. 1992.

- [118] O'Connor, D., Sexton, B., and Smart, R. S. C.. *Surface Analysis Methods in Materials Science*. Germany: Springer-Verlag Berlin Heidelberg 2003.
- [119] Ektessabi, A. I., Kawakami, T., and Watt, F. Distribution and chemical state analysis of iron in the Parkinsonian substantia nigra using synchrotron radiation micro beams. *Nucl. Instrum. Methods Phys. Res. Sect. B* 213 (2004): 590–594.
- [120] Hollas, J. M.. *Basic Atomic and Molecular Spectroscopy*. Cambridge: The Royal Society of Chemistry 2002.
- [121] Swanepoel, R. Determination of the thickness and optical constants of amorphous silicon. *Journal of Physics E: Scientific Instruments* 16 (1983): 1214–1222.
- [122] Zhang, W. F., Huang, Y. B., Zhang, M. S., and Liu, Z. G. Nonlinear optical absorption in undoped and cerium-doped BaTiO₃ thin films using Z-scan technique. *Appl. Phys. Lett.* 76 (2000): 1003–1005.
- [123] Hiibert, T., Beck, U., and Kleinke, H. Amorphous and nanocrystalline SrTiO₃ thin films. *J. Non-Cryst. Solids* 196 (1996): 150–154.
- [124] Tauc, J. C.. *Optical Properties of Solids*. North-Holland: Amsterdam 1972.
- [125] Urbach, F. The Long-Wavelength Edge of Photographic Sensitivity and of the Electronic Absorption of Solids. *Phys. Rev.* 92 (1953): 1324–1324.
- [126] Matthews, B., Li, J., Sunshine, S., Lerner, L., and Judy, J. W. Effects of electrode configuration on polymer carbon-black composite chemical vapor sensor performance. *IEEE Sensors Journal* 2 (2002): 160–168.
- [127] Durrani, S. The influence of electrode metals and its configuration on the response of tin oxide thin film CO sensor. *Talanta* 68 (2006): 1732–1735.
- [128] Capone, S. et al. Moisture influence and geometry effect of Au and Pt electrode on CO sensing response of SnO₂ microsensor based on sol-gel thin films. *Sens. Actuation, B* 77 (2001): 503–511.

- [129] Wang, Y., Cheng, Y. L., Zhang, Y. W., Chan, H. L. W., and Choy, C. L. Dielectric behaviors of lead zirconate titanate ceramics with coplanar electrodes. *Mater. Sci. Eng., B* 99 (2003): 79–82.
- [130] Wang, Y., Chong, N., Cheng, Y. L., Chan, H. L. W., and Choy, C. L. Dependence of capacitance on electrode configuration for ferroelectric films with interdigital electrodes. *Microelectron. Eng.* 66 (2003): 880–886.
- [131] Hong, L., Zhaohui, P., Xiaohong, Z., Dingquan, X., and Jianguo, Z. The effect of different electrode structures on the dielectric properties of lanthanum-doped lead titanate ferroelectric thin films. *Front. Mater. Sci. China* 1 (2007): 322–325.
- [132] Li, L. Y. et al. Effect of electrode configuration on capacitive humidity sensitivity of silicon nanoporous pillar array. *Physica E* 41 (2009): 621–625.
- [133] Lai, L. et al. Physical properties of $\text{YBa}_2\text{Cu}_3\text{O}_7$ thin films using microstrip ring resonators technique. *Physica C* 443 (2006): 9–17.
- [134] Farnell, G. W., Cermak, I. A., and Wong, S. K. Capacitance and field distributions for interdigital surface-wave transducers. *IEEE T. Son. Ultrason.* 17 (1970): 188–195.
- [135] Sirinam, S.. *Structural properties and surface morphology of BaTi_3 and SrTiO_3 prepared by sol-gel method*. Seniors project Chulalongkorn University 2006.
- [136] Yoneda, Y., Okabe, T., Sakaue, K., and Terauchi, H. Growth of ultrathin BaTiO_3 films on SrTiO_3 and MgO substrates. *Surf. Sci.* 410 (1998): 62–69.
- [137] Thomas, R., Dube, D., Kamalasanan, M., and Chandra, S. Optical and electrical properties of BaTiO_3 thin films prepared by chemical solution deposition. *Thin Solid Films* 346 (1999): 212–225.

- [138] Dejneka, A. et al. Atmospheric barrier-torch discharge deposited ZnO films: optical properties, doping and grain size effects. *J. Nanosci. Nanotechnol.* 9 (2009): 4094–4097.
- [139] Metina, H. and Esen, R. Annealing studies on CBD grown CdS thin films. *J. Cryst. Growth* 258 (2003): 141–148.
- [140] Tauc, J. and Menth, A. States in the gap. *J. Non-Cryst. Solids* 8 (1972): 569–585.
- [141] Wang, J. et al. Microstructure, optical and dielectric properties of compositional graded (Ba,Sr)TiO₃ thin films derived by RF magnetron sputtering. *J. Mater. Sci. Mater. Electron.* 20 (2009): 319–322.
- [142] Li, H. et al. Optical properties of lead lanthanum zirconate titanate amorphous ferroelectric-like thin films. *Jpn. J. Appl. Phys.* 39 (2000): 1180–1183.
- [143] Onton, A., Marrello, V., Lucovsky, G., and Galeener, F. L.. *Ferroelectrics*. New York: AIP Conf. Proc. 1976.
- [144] Cardona, M. Optical properties and band structure of SrTiO₃ and BaTiO₃. *Phys. Rev.* 140 (1965): 651–655.
- [145] Benthem1, K. V., Elsasser, C., and French, R. H. Bulk electronic structure of SrTiO₃: experiment and theory. *J. Appl. Phys.* 90 (2001): 6156–6164.
- [146] Suzuki, K. and Kijima, K. Optical band gap of barium titanate nanoparticles prepared by RF-plasma chemical vapor deposition. *Jpn. J. Appl. Phys.* 44 (2005): 2081–2082.
- [147] Xu, Y. N., Ching, W. Y., and French, R. H. Selfconsistent band structures and optical calculations in cubic ferroelectric perovskites. *Ferroelectrics* 111 (1990): 23–32.

- [148] Trepakov, V. A. et al. SrTiO₃:Cr nanocrystalline powders: size effects and optical properties. *J. Phys.: Condens. Matter* 21 (2009): 375303–375307.
- [149] Wohlecke, M., Marrello, V., and Onton, A. O. Retractive index of BaTiO₃ and SrTiO₃ films. *J. Appl. Phys.* 48 (1977): 1748–1750.
- [150] Wemple, S. H. Optical oscillator strengths and excitation energies in solids, liquids, and molecules. *J. Chem. Phys.* 67 (1977): 2151–2168.
- [151] Farges, F. et al. The effect of redox state on the local structural environment of iron in silicate glasses: a combined XAFS spectroscopy, molecular dynamics, and bond valence study. *J. Non-Cryst. Solids* 344 (2004): 176–188.
- [152] Wei, X. et al. Size-controlled synthesis of BaTiO₃ nanocrystals via a hydrothermal route. *Mater. Lett.* 62 (2008): 3666–3669.
- [153] Ye, Y. and Guo, T. Dielectric properties of Fe-doped Ba_{0.65}Sr_{0.35}TiO₃ thin films fabricated by the sol gel method. *Ceram. Int.* 35 (2009): 2761–2765.
- [154] Ling, Z., Leach, C., and Freer, R. Heterojunction gas sensors for environmental NO₂ and CO₂ monitoring. *J. Eur. Ceram. Soc.* 21 (2001): 1977–1980.
- [155] Wongwarakarn, P.. *The ethanol gas sensitivity of undoped and Fe doped CCTO films*. Seniors project Chulalongkorn University 2010.
- [156] Williams, D. E. Semiconducting oxides as gas-sensitive resistors. *Sens. Actuation, B* 57 (1999): 1–16.
- [157] Naisbitt, S., Pratt, K., Williams, D., and Parkin, I. A microstructural model of semiconducting gas sensor response: The effects of sintering temperature on the response of chromium titanate (CTO) to carbon monoxide. *Sens. Actuation, B* 114 (2006): 969–977.
- [158] Joshi, P. and Desu, S. Structural, electrical, and optical studies on rapid thermally processed ferroelectric BaTiO₃ thin films prepared by metallo-

- organic solution deposition technique. *Thin Solid Films* 300 (1997): 289–294.
- [159] Xu, J., Zhai, J., and Yao, X. Structure and dielectric nonlinear characteristics of BaTiO₃ thin films prepared by low temperature process. *J. Alloys Compd.* 467 (2009): 567–571.
- [160] Lee, B. and Zhang, J. Preparation, structure evolution and dielectric properties of BaTiO₃ thin films and powders by an aqueous sol-gel process. *Thin Solid Films* 388 (2001): 107–113.
- [161] Liu, Z., Deng, H., Yang, P., and Chu, J. Enhanced ferroelectric properties of Fe-doped BaTiO₃ thin film deposited on LaNiO₃/Si substrate by sol-gel technique. *Mater. Lett.* 63 (2009): 2622–2624.
- [162] Krupanidhi, S. and Rao, G. M. Pulsed laser deposition of strontium titanate thin films for dynamic random access memory applications. *Thin Solid Films* 249 (1994): 100–108.
- [163] Khachaturyan, A. G.. *Theory of Structural Transformations in Solids*. John Wiley, New York, USA 1983.
- [164] Salje, E.. *Phase Transitions in Ferroelastic and Coelastic Crystals*. Cambridge University Press 1990.
- [165] Mitsui, T. and Furuichi, J. Domain Structure of Rochelle Salt and KH₂PO₄. *Phys. Rev.* 90 (1953): 193–202.
- [166] Arlt, G., Hennings, D., and de With, G. Dielectric properties of fine-grained barium titanate ceramics. *J. Appl. Phys.* 58 (1985): 1619–1625.
- [167] Kinoshita, K. and Yamaji, A. Grain size effects on dielectric properties in barium titanate ceramics. *J. Appl. Phys.* 47 (1976): 371–373.
- [168] Frey, M. H., Xu, Z., Han, P., and Payne, D. A. The role of interfaces on an apparent grain size effect on the dielectric properties for ferroelectric barium titanate ceramics. *Ferroelectrics* 206 (1998): 337–353.

- [169] Hoshina, T. et al. Size Effect and Domain Wall Contribution of Barium Titanate Ceramics. *Ferroelectrics* 402 (2010): 29–36.
- [170] Kongwut, O.. *Effects of gamma ray irradiation on fundamental properties of perovskite thin films prepared by a sol-gel technique*. Masters thesis Chulalongkorn University 2010.
- [171] Sinha, D., Phukan, T., Tripathy, S., Mishra, R., and Dwivedi, K. Optical and electrical properties of gamma irradiated PADC detector. *Radiat. Meas.* 34 (2001): 109–111.
- [172] Gammon, E.. *General Chemistry*. USA, Hughton Mifflin company. 2009.



ศูนย์วิทยทรัพยากร
จุฬาลงกรณ์มหาวิทยาลัย



APPENDICES

ศูนย์วิทยทรัพยากร
จุฬาลงกรณ์มหาวิทยาลัย

Appendix A

XRD database

In this thesis work, we have used the international centre for diffraction data (ICDD) for assuring the position of the XRD peaks of BaTiO_3 and SrTiO_3 . The ICDD databases for BaTiO_3 and SrTiO_3 are shown as the following:



Pattern : 00-005-0626		Radiation = 1.540598		Quality : High		
BaTiO ₃		2th	i	h	k	l
Barium Titanium Oxide		22.039	12	0	0	1
		22.263	25	1	0	0
		31.498	100	1	0	1
		31.647	100	1	1	0
		38.888	46	1	1	1
		44.856	12	0	0	2
		45.378	37	2	0	0
		50.614	6	1	0	2
		50.978	8	2	0	1
		51.100	7	2	1	0
		55.955	15	1	1	2
		56.253	35	2	1	1
		65.755	12	2	0	2
		66.123	10	2	2	0
		70.359	5	2	1	2
		70.662	2	3	0	0
		74.336	5	1	0	3
		75.094	7	3	0	1
		75.164	9	3	1	0
		78.768	3	1	1	3
		79.472	5	3	1	1
		83.492	7	2	2	2
		86.965	1	2	0	3
		87.287	1	3	0	2
		88.069	1	3	2	0
		91.586	7	2	1	3
		92.060	12	3	1	2
		92.327	12	3	2	1
		99.494	1	0	0	4
		100.984	2	4	0	0
		103.869	1	1	0	4
		104.502	1	2	2	3
		104.991	1	3	2	2
		105.362	1	4	1	0
		108.256	3	1	1	4
		108.946	1	3	0	3
		109.733	5	4	1	1
		113.556	2	3	1	3
		114.362	2	3	3	1
		117.506	3	2	0	4
Lattice : Tetragonal		Mol. weight = 233.23				
S.G. : P4mm (99)		Volume [CD] = 64.41				
a = 3.99400		Dx = 6.012				
c = 4.03800		l/lcor = 8.34				
Z = 1						
<p>Color: Colorless Additional diffraction line(s): Plus 10 additional reflections. Sample source or locality: Sample from National Lead Company. Sample preparation: Annealed at 1480 C in MgO. Analysis: Spectroscopic analysis: <0.1% Bi, Sr; <0.01% Al, Ca, Fe, Mg, Pb, Si; <0.001% Mn, Sn. General comments: Inverts to cubic form at 120 C. Temperature of data collection: X-ray pattern at 26 C. General comments: Merck Index, 8th Ed., p. 122. Data collection flag: Ambient.</p>						
Swanson, Fuyat., Natl. Bur. Stand. (U.S.), Circ. 539, volume 3, page 45 (1954)						
CAS Number: 12047-27-7						
Radiation : CuK α 1		Filter : Beta				
Lambda : 1.54050		d-sp : Not given				
SS/FOM : F30= 19(0.0490,32)						

Pattern : 00-035-0734		Radiation = 1.540598		Quality : High		
SrTiO ₃		2th	i	h	k	l
Strontium Titanium Oxide Tausonite, syn		22.783	12	1	0	0
		32.424	100	1	1	0
		39.985	30	1	1	1
		46.485	50	2	0	0
		52.358	3	2	1	0
		57.796	40	2	1	1
		67.805	25	2	2	0
		72.545	1	3	0	0
		77.177	15	3	1	0
		81.724	5	3	1	1
		86.206	8	2	2	2
		95.131	16	3	2	1
		104.154	3	4	0	0
		113.613	10	4	1	1
		118.589	3	3	3	1
		123.832	10	4	2	0
		135.422	6	3	3	2
		150.146	9	4	2	2
Lattice : Cubic		Mol. weight = 183.52				
S.G. : Pm-3m (221)		Volume [CD] = 59.55				
a = 3.90500		Dx = 5.118				
Z = 1		I/cor = 6.22				
<p>Sample source or locality: Sample from Nat. Lead Co. Analysis: Spectrographic analysis: <0.01% Al, Ba, Ca, Si; <0.001% Cu, Mg. Temperature of data collection: Pattern taken at 25 C. Additional pattern: To replace 00-005-0634 and 00-040-1500. Data collection flag: Ambient.</p>						
Swanson, H., Fuyat., Natl. Bur. Stand. (U.S.), Circ. 539, volume 3, page 44 (1954)						
Radiation : CuKα1		Filter : Beta				
Lambda : 1.54050		d-sp : Diffractometer				
SS/FOM : F18= 47(0.0182,21)						

Appendix B

Weight percentage calculating of Fe doping concentrations

In this work, we chose the concentrations of Fe doping as 3, 5 and 10% by weight. The formula for calculating weight percentages of Fe doping for BaTiO₃ is presented in the equation below:

$$\text{wt}\% = \left(\frac{\frac{g_{\text{FeSO}_4 \cdot 7\text{H}_2\text{O}}}{\text{MW}_{\text{FeSO}_4 \cdot 7\text{H}_2\text{O}}}}{\frac{g_{\text{Ba}}}{\text{MW}_{\text{Ba}}}} \right) \left(\frac{\text{MW}_{\text{FeSO}_4 \cdot 7\text{H}_2\text{O}}}{\text{MW}_{\text{BaTiO}_3}} \right) \times 100 \quad (1)$$

where $g_{\text{FeSO}_4 \cdot 7\text{H}_2\text{O}}$ and g_{Ba} are weight of iron (II) sulphate and barium, respectively. $\text{MW}_{\text{FeSO}_4 \cdot 7\text{H}_2\text{O}}$, MW_{Ba} and $\text{MW}_{\text{BaTiO}_3}$ are molecular weight of iron (II) sulphate, barium and barium titanate, respectively. For example, for obtaining Fe doping concentration as 10% by weight. We replaced the the value of g_{Ba} to be 2.558 g (see subsection 4.1). The molecular weight of iron (II) sulphate, barium and barium titanate was replaced by 278.012, 173.327 and 233.240 g/mol, respectively. So, the weight of iron (II) sulphate was 0.435 g. However, our EDS results showed that Fe doping concentration in BaTiO₃ films was found to be 8, 4 and 2% by weight whereas the Fe concentrations obtaining from our calculation were 10, 5 and 3% by weight. The smaller obtained Fe concentrations may be due to incomplete dissolution of iron (II) sulphate in solvent during precursor synthesis process. For calculating Fe doping concentration of SrTiO₃, the symbols g_{Ba} , MW_{Ba} and $\text{MW}_{\text{BaTiO}_3}$ were changed into g_{Sr} , MW_{Sr} and $\text{MW}_{\text{SrTiO}_3}$, which are weight of strontium (2.056 g), molecular weight of strontium (87.620 g/mol) and molecular weight of strontium titanate (183.497 g/mol), respectively.

Appendix C

Conference presentations

International presentations:

2008, T. Supasai, S. Dangtip, P. Learngarunsri, N. Boonyopakorn, A. Wisitsoraat and S.K. Hodak. Structure and Optical Studies on BaTiO₃/SrTiO₃ Multilayer Films Prepared by Sol-Gel Technique. The 4th Mathematics and Physical Science Graduate Congress, National University of Singapore, Singapore (19-20 December 2008)

2009, T. Supasai, A. Wisitsoraat and S.K. Hodak. Ethanol Sensor Based on BaTiO₃/SrTiO₃ Multilayer Films Prepared by a Sol-Gel Technique, Asiasense 2009, Imperial Queens Park Hotel, Bangkok (29-31 July 2009)

2009, T. Supasai, A. Wisitsoraat and S.K. Hodak. Characterization of Fe-Doped SrTiO₃/BaTiO₃ Multilayer Films and Their Ethanol Applications. The 5th Mathematics and Physical Sciences Graduate Congress, Faculty of Science, Chulalongkorn University, Bangkok (7-9 December 2009)

2010, T. Supasai, A. Wisitsoraat and S.K. Hodak. Microstructure and Ethanol Sensing Properties of Fe-Doped SrTiO₃/ BaTiO₃ Multilayer Films Prepared by Sol-Gel Spin Coating Technique. The 16th International Conference on Crystal Growth, Beijing International Convention Center, Beijing, China (8-13 August 2010)

Local Presentations:

2008, T. Supasai, S. Dangtip, P. Learngarunsri, N. Boonyopakorn, A. Wisitsoraat and S.K. Hodak. Structure and Optical Properties of Sol-Gel Derived

BaTiO₃/SrTiO₃ Film with Multilayer on ITO Coated Glass. The Science Forum 2008, Faculty of Science, Chulalongkorn University, Bangkok (13-14 March 2008)

2008, T. Supasai, S. Dangtip, P. Learngarunsri, N. Boonyopakorn, A. Wisitsoraat and S.K. Hodak. Structure and Optical Properties of Sol-Gel Derived BaTiO₃/SrTiO₃ Film with Multilayer on ITO Coated Glass. Siam Physics Congress 2008, The Mandarin Golden Valley Resort and Spa, Khao Yai, Nakorn Ratchasima (20-22 March 2008)

2009, T. Supasai, A. Wisitsoraat and S.K. Hodak. Ethanol Sensor Based on BaTiO₃/SrTiO₃ Multilayer Films Prepared by a Sol-Gel Technique. Siam Physics Congress 2009, Methavalai Hotel, Cha-am, Phetchburi (19-21 March 2009)

2010, T. Supasai, A. Wisitsoraat and S.K. Hodak. Characterization of Fe-Doped SrTiO₃/BaTiO₃ Multilayer Films and Their Ethanol Applications. Siam Physics Congress 2010, River Kwai Village Hotel, Kanchanaburi (25-27 March 2010)

ศูนย์วิทยทรัพยากร
จุฬาลงกรณ์มหาวิทยาลัย

Appendix D

Publications

T. Supasai, S. Dangtip, P. Learngarunsri, N. Boonyopakorn, A. Wisitsoraat and S. K. Hodak, Influence of Temperature Annealing on Optical Properties of SrTiO₃/BaTiO₃ Multilayered Films on Indium Tin Oxide, Applied Surface Science 256 (2010) 4462-4467.

S. K. Hodak, T. Supasai, A. Wisitsoraat and Jose H. Hodak, Design of Low Cost Gas Sensor Based on SrTiO₃ and BaTiO₃ Films, Journal of Nanoscience and Nanotechnology 10 (2010) 7236-7238.



ศูนย์วิทยทรัพยากร
จุฬาลงกรณ์มหาวิทยาลัย

Appendix E

Research award



จุฬาลงกรณ์มหาวิทยาลัย

Vitae

Miss Thidarat Supasai was born on April 10, 1981 in Surin, Thailand. She received her Bachelor Degree of Science in Physics from Mahidol University in 2002, then received her Master degree of Science in Physics from Chulalongkorn University in 2006, and continued her Ph.D.'s study in Physics at Chulalongkorn University.



ศูนย์วิทยทรัพยากร
จุฬาลงกรณ์มหาวิทยาลัย